UNIVERSITY OF COIMBRA

Faculty of Sciences and Technology

Department of Physics

Swept Source OCT for retinal imaging on small animals: performance, phase stabilization and optical setup

Master's Degree in Engineering Physics

João Padre Bernardino

September 2016

UNIVERSITY OF COIMBRA

Faculty of Sciences and Technology

Department of Physics

Swept Source OCT for retinal imaging on small animals: performance, phase stabilization and optical setup

Thesis submitted to University of Coimbra for obtaining the degree of Master in Engineering Physics

Advisor:

Doctor António Miguel Lino Santos Morgado

João Padre Bernardino

September 2016

Acknowledgments

I would first like to thank my thesis advisor Professor António Miguel Morgado for his guidance and support given throughout this project. His immense knowledge and continuous input allowed me to deliver this thesis and accomplish this great milestone. His door was always open whenever a question needed an answer, and for that, I am very thankful.

I would also like to express my gratitude towards Professor Rui Bernardes, as the second reader of this thesis, and for all his suggestions regarding the programming aspects of this project.

A special thanks to my lab colleague, Ph. D. student Susana Silva, for her willingness and all the precious help provided during this last year.

Last, but not least, I would like to thank my parents, my sister, my grandparents and my girlfriend for all the support and encouragement given throughout these years. All that I am, I owe it to all of you. Thank you all so much.

João Bernardino

Abstract

Optical Coherence Tomography (OCT) is a noninvasive imaging technique capable of providing high speed and high resolution cross-sectional images and three-dimensional volumes of non-homogeneous samples, such as retinal tissue. It is mainly used in ophthalmology, where it is considered a very powerful tool for early diagnosis of ocular pathologies.

For research purposes, OCT allows the study of new medical diagnostic approaches and treatments in small animals.

With this purpose in mind, a Swept Source OCT system is being developed at IBILI (Institute for Biomedical Imaging and Life Sciences, Faculty of Medicine – University of Coimbra) to image the retinal structures of the rat's eye. It is based on a swept source laser (1060 nm of central wavelength and 110 nm of bandwidth), a balanced detector and a 400 MSPS analog-to-digital acquisition board.

The main goal of this work is to obtain the performance needed for reliable phase measurements. The secondary goal is to design an optical solution capable of imaging the retinal structures of the rat eye. Finally, the tertiary goal is the study of the performance parameters of the OCT in its current state of development.

The first goal was achieved with the help of a numerical phase stabilization algorithm. The design of an optical setup towards imaging the rat's retina with good quality was achieved using the Zemax OpticStudio. Results obtained with respect to the tertiary goal allow to conclude that the performance parameters meet the standards for OCT retinal imaging.

Resumo

A Tomografia por Coerência Ótica (OCT) é uma técnica de imagiologia não invasiva capaz de adquirir imagens de secção e volumes de amostras não homogéneas, como a retina, a velocidades e resoluções elevadas. É utilizada maioritariamente em oftalmologia, sendo considerada uma poderosíssima ferramenta para o diagnóstico precoce de patologias oculares.

Em investigação científica, esta técnica tem servido de base para o desenvolvimento de novos métodos de diagnóstico e para o estudo de novos tratamentos em humanos e em modelos animais de doença.

Com este mesmo objetivo, está a ser desenvolvido no IBILI (Instituto de Imagem Biomédica e Ciências da Vida, Faculdade de Medicina – Universidade de Coimbra) um sistema OCT com vista à imagiologia das estruturas da retina do rato. O sistema baseia-se numa fonte de varrimento com 1060 nm de comprimento de onda central e 110 nm de largura de banda, um detetor balanceado e uma placa de aquisição.

O objetivo principal deste trabalho é a obtenção das condições de desempenho necessárias para aquisição de medidas de fase fiáveis. O segundo objetivo centra-se no desenvolvimento de uma solução ótica capaz de obter imagens das estruturas do olho de rato. Finalmente, o terceiro objetivo deste trabalho é o estudo dos parâmetros de desempenho do sistema OCT no seu estado de desenvolvimento atual.

O primeiro objetivo foi atingido com a ajuda de um algoritmo de estabilização de fase por métodos numéricos. O desenvolvimento de um sistema ótico destinado à imagiologia da retina de rato com qualidade foi atingido utilizando o Zemax OpticStudio. Os resultados obtidos referentes ao terceiro objetivo permitem concluir que os parâmetros de desempenho do sistema obedecem aos *standards* desejados para a imagiologia OCT de retina.

Contents

List of Figures

List of Tables

Introduction

Optical Coherence Tomography (OCT) is a noninvasive imaging technique based on the principle of light interference, capable of providing high speed and high resolution cross-sectional images and three-dimensional volumes of non-homogeneous transparent samples, such as biological tissue. Since the late 1980s and early 1990s, when this technique was first developed [1], OCT has seen many improvements in acquisition speed, imaging resolution, tissue penetration and data processing, and has become a tool for a variety of applications concerning biomedical imaging, for either investigation or clinical purposes. Within those applications, ophthalmic diagnosis can be highlighted, where this imaging technique is considered a very powerful tool for *in vivo* assessment of retinal pathologies and functional information of the human and animal eye.

OCT was first developed as a Time Domain technique and later moved to the Fourier Domain, currently the dominant field, when the necessities for real time imaging became more and more demanding with regards to acquisition speed.

When compared to other techniques of the standard clinical practice, such as X-ray Computed Tomography (CT), Magnetic Resonance Imaging (MRI) or Positron Emission Tomography (PET) imaging, OCT provides a resolution in the cell size range in opposition with a few millimeters resolution of the former techniques [1], making it a better solution between noninvasive and minimally invasive imaging systems. Because of its noninvasive nature, tissue removal for further analysis is not necessary, presenting a major advantage over traditional excisional biopsy, by removing its hazardous nature and providing the possibility to acquire information of tissue samples in areas that excisional biopsy can't reach, such as the retina.

The present essay describes the work conducted during my master thesis project, while involved in the development of a Swept Source Optical Coherence Tomography system, at IBILI (Institute for Biomedical Imaging and Life Sciences, Faculty of Medicine – University of Coimbra). The main objective of this project it to achieve the performance needed for reliable phase measurements. The secondary objective is to design an optical solution for imaging the retinal structures of the rat eye. The tertiary objective is the study of the performance parameters of the OCT in its current state of development.

In the first chapter, the theory of Optical Coherence Tomography is presented, starting with a brief piece of history behind its creation followed by an explanation of the physical principles behind this technology. Then, an overview of the different domain modalities, the parameters for evaluating the system's performance and a reference to some of its main applications are discussed.

Chapter two describes the main components of the Swept Source OCT system implemented at IBILI and used during this project.

The third chapter discusses the subject of Phase-Sensitive OCT, namely the topic of phase stability of a Swept Source OCT system, with its experimental determination for the OCT system used during this thesis. Then, a fully numerical phase stabilization algorithm is discussed, aiming to improve the system's phase stability.

Chapter four presents the optical simulations performed using the Zemax OpticStudio 15 Standard Edition software. First, an optical model of the rat's eye is presented followed by the optical setup designed for imaging the rat's retinal structures.

The final chapter, chapter five, presents the system's performance results obtained throughout this thesis.

Chapter 1

Optical Coherence Tomography

As the first chapter of this master's thesis it is important to give a detailed explanation about the concept of Optical Coherence Tomography, namely what are the fundamental principles behind it, so that the reader can properly understand the subjects discussed during the present essay.

This chapter details the theoretical background for OCT, first presenting some history that led to the its appearance, then discussing the physical principles involved, such as the interferometer, theory on light coherence and light interference, as well as explaining a mathematical formulation for this imaging technique. Next, the different OCT approaches will be exposed and compared, providing a thorough description of the Swept Source OCT modality. Then, an overview of the performance parameters of this technology will be discussed and finally, some applications will also be presented.

1.1 History of OCT

The initial approaches that ultimately led to the development of OCT began with attempts to measure the time delays of backscattered light, much like with sound waves in ultrasound. However, time delays in the order of magnitude of femtoseconds were too small to detect through the use of direct measurement, due to the high propagation velocities involved. This constituted a problem, so alternative techniques were created and from them, OCT emerged.

The first approach for detecting optical echoes was published in 1971 by M. Duguay and A. Mattick [2], with the application of the Kerr effect (change in the refractive index, as consequence of application of an electric filed to the material) through the use of a fast optical shutter for detecting light pulses travelling through a scattering medium. Duguay then concluded that this technique could be used for medical purposes, namely tissue imaging through high-speed optical gating [2].

In 1985 [3], Fujimoto *et al.* described a noninvasive tissue imaging technique based on femtosecond laser pulses, capable of performing optical ranging through nonlinear cross-correlation gating. Using 65 *fs* laser pulses, spatial resolutions of less than 15 μm could be achieved [3]. The experimental results for *in vivo* imaging of a rabbit's eye are presented in Figure 1, where it is possible to identify some of the structures of the rabbit's eye and give a rough estimate for their thickness.

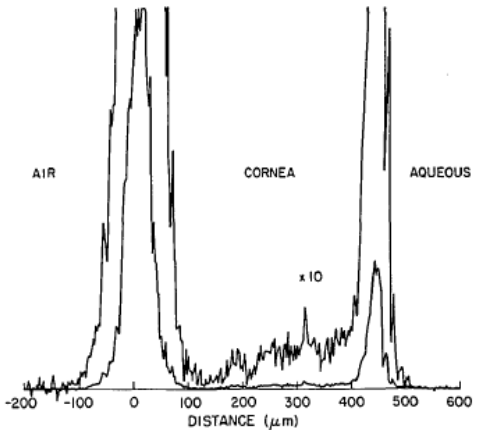

Figure 1. Experimental results for in vivo imaging of rabbit's eye. From [3].

The breakthrough for OCT came in the year 1987, with Fercher *et al.* in "Eye-length measurement by interferometry with partially coherent light". Describing an interferometric technique using partially coherent light, as presented in Figure 2, it was possible to determine, with a good precision, the human eye length in the axial direction,

analyzing the cross-correlation of the field amplitudes of the measurement beam and the reference beam [4].

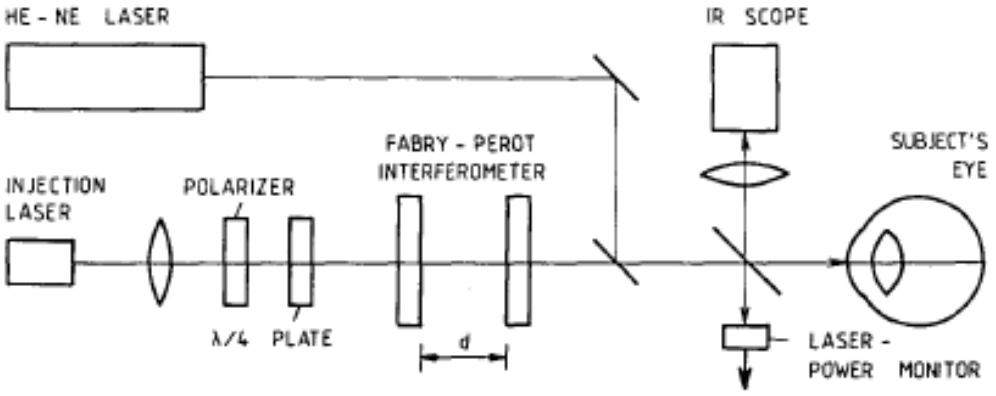

Figure 2. Experimental setup from Fercher et al. [4] used to measure the optical length of the eye.

The experiments conducted by Fercher *et al.* demonstrated two very important insights for imaging based on low-coherence interferometry. The first states that in order to observe interference, both the delay and measurement path-lengths had to be equal. In fact, as it is discussed in the next section of this chapter, interference occurs when both path-lengths are matched to within a coherence length [7]. The second relates both the resolution and the coherence length as it is said, "a*n estimate of the resolution can be obtained by the coherence length of the radiation*" [4]. This conclusion will also be discussed in the next chapter of this thesis, when presenting the concept of axial resolution of an OCT system.

A few years later, in 1991, Clivaz *et al.* described a technique called Optical Low Coherence Reflectometry [5], implementing a Michelson Interferometer to analyze diffuse biological tissue and determine its thickness. A schematic of the experimental setup and the results obtained for different interfaces are presented in Figure 3 [5].

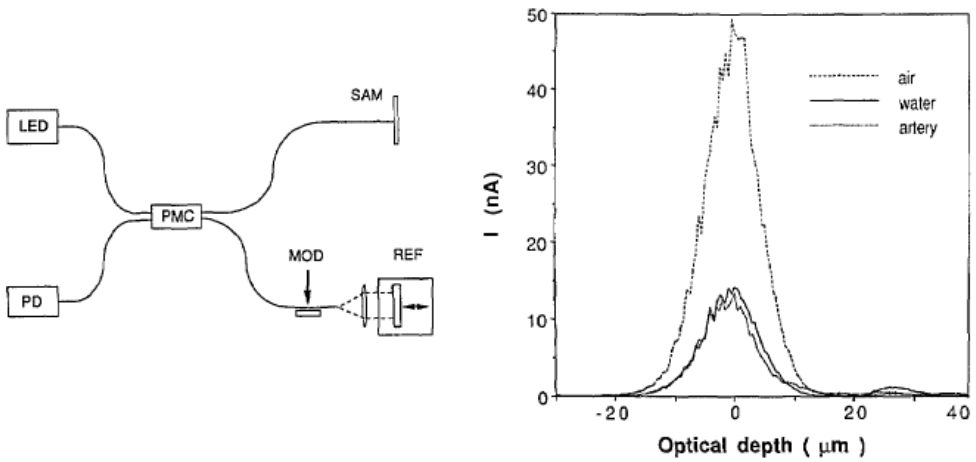

Figure 3. (Left) Schematic of the experimental setup used by Clivaz et al. – LED: edge-emitting diode, PMC: 50:50 panda coupler, SAM: sample, PD: InGaAs photodiode, MOD: phase modulator, REF: reference arm; (Right) Reflection signal as a function of the optical depth for three interfaces: fiber-air, fiber-pure water, fiber-arterial wall. From [5]

Later that year 1991, an imaging technique called Optical Coherence Tomography was presented by Huang *et al.* for noninvasive cross-sectional imaging in biological systems [6]. The experimental setup, exposed in Figure 4, extends the previous Optical Low Coherence Reflectometry [5] to tomographic imaging, being able to acquire two-dimensional reflection images, as is also shown by the human retina image acquired experimentally presented in Figure 4.

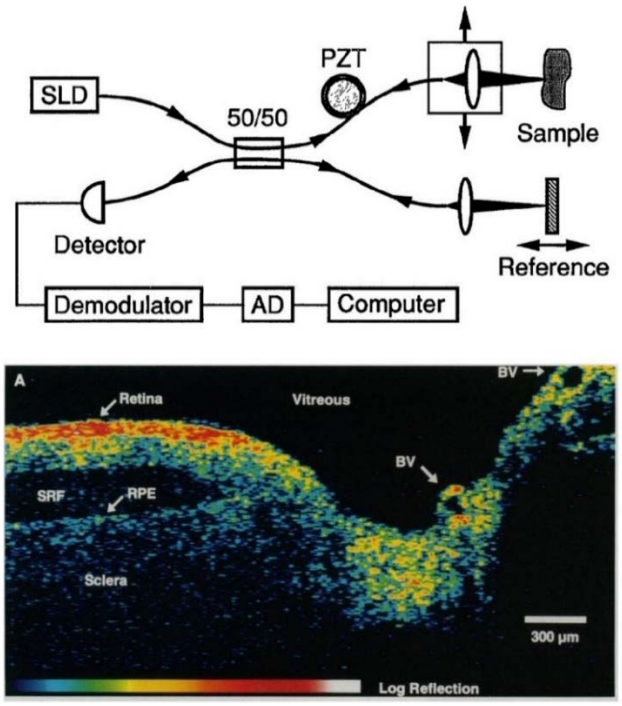

Figure 4. (Up) Schematic of the OCT scanner. (Bottom) Optical coherence tomograph of human retina, obtained by D. Huang *et al* in 1991 [6].

With the improvements done by Huang *et al.* a new imaging technique named Optical Coherence Tomography was born. Since then, it has been a technological reference in the field of biological imaging.

1.2 Principles of OCT

1.2.1 The interferometer

Optical Coherence Tomography is an imaging technique based upon the principle of light interference resulting from the implementation of an interferometer, exemplified in Figure 5 with a Michelson interferometer. Light emitted from a coherent source is directed towards a beam splitter and split into two paths, where it is reflected by mirrors 1 and 2. The reflected light from each path, or interferometer arm as is commonly called, is re-directed back into the beam splitter where it interferes, forming an interference pattern.

It is important to note that, as first noticed by Fercher *et al.* [4], an interference pattern is observed only when the optical path-lengths of the light in both interferometer arms are matched to within the coherence length of the light [7].

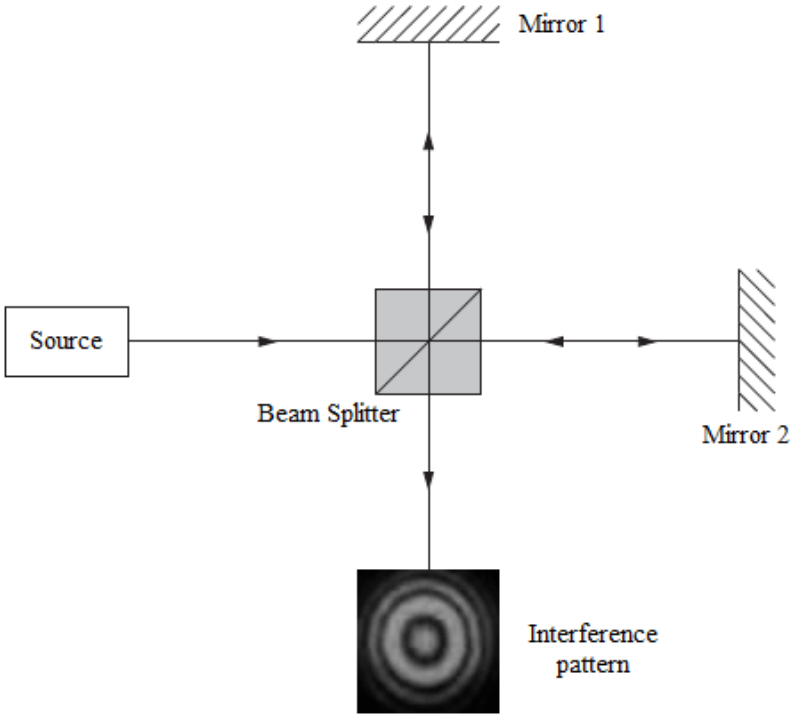

Figure 5. Michelson Interferometer. Adapted from [7].

1.2.2 Light coherence and light interference

To understand the concept of coherence it is important to clarify how light is generated in order to conclude that a source cannot be perfectly monochromatic. Light is produced when an atomic or molecular transition from an excited state to a lower energy state occurs, and consequent emission of electromagnetic radiation takes place, with energy directly proportional to its frequency:

$$E = hf \tag{1}$$

However, the resulting radiation from atomic transitions is not monochromatic (i.e. only one defined frequency and wavelength). This is mainly due to the uncertainty in the energy of the excited state, consequence of Heisenberg's uncertainty principle $\Delta E \Delta t \geq \frac{\hbar}{2}$, yielding higher uncertainties in energy (ΔE) when shorter lifetimes (Δt) of the excited states are involved. This is known as the "natural linewidth".

The emission of light is not continuous, it occurs in short oscillatory pulses, named wave trains. If we consider the case of two wave trains with slightly different wavelengths, a light wave is considered to be coherent when, through a long enough period of time, those wave trains emitted with a time delay between each other have the same characteristics [8], namely phase and amplitude. The same explanation applies to more than just two wave trains, with an increasing number of wave trains resulting in a shorter time during which the conditions are met.

A light field is coherent when there is a fixed phase relationship between the electric field value at different places and different times. This definition implies that light coherence is described in terms of temporal and spatial coherence. Temporal coherence represents the correlation between the phases of a light wave at different times, in the same location. Spatial coherence represents the correlation between the phases of the light wave at different points across the beam profile. The time period over which the coherence is lost is known as coherence time (Δt_c) and the corresponding distance, called coherence length (l_c), is given by:

$$l_c = c \times \Delta t_c \tag{2}$$

Although the coherence length represents the distance over which the coherence is lost, it characterizes the temporal coherence and not the spatial coherence, since it is obtained directly from the coherence time.

A laser source emitting a very short range of wavelengths has a much larger coherence length/time than, for example, a broadband source, which emits a wide spectrum of wavelengths.

As mentioned before, interference between light from two different paths of the interferometer will only occur if the corresponding optical path lengths are matched to within the light's coherence length, which is equivalent to, in terms of difference between the two path lengths, $\Delta L \leq l_c$. Only under this condition it is possible to observe/detect an interference pattern.

OCT requires low temporal coherence, for obtaining high axial resolution, combined with high spatial coherence (i.e. a transversal monomode, Gaussian beam profile), that contributes to high lateral resolution and good signal quality.

1.2.3 OCT basic setup

Based on the insights earlier discussed, it is now appropriate to present a generic and simplified system architecture for an OCT system as well as an overview for its operation principles. As already mentioned, Optical Coherence Tomography is an interferometric technique.

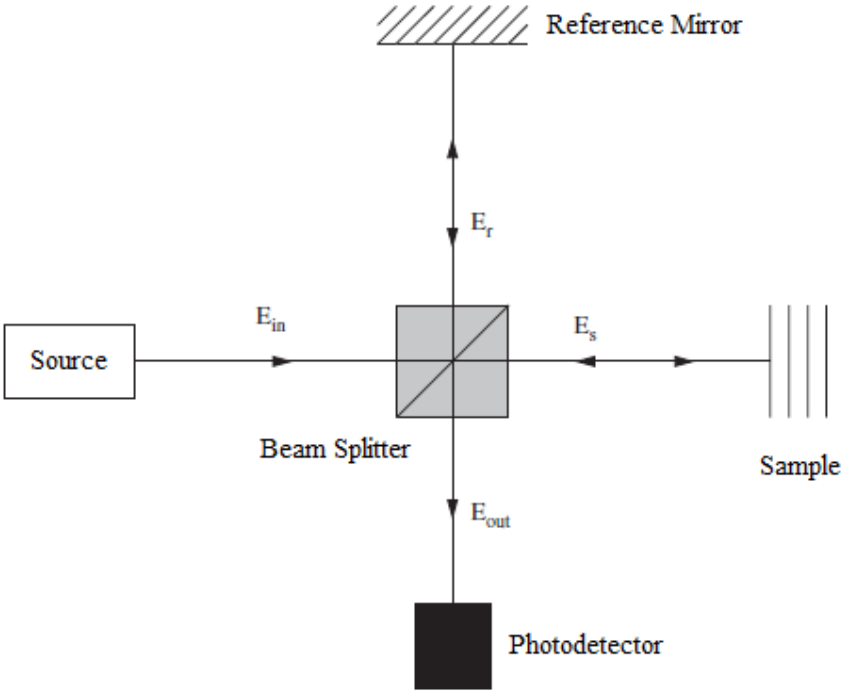

Figure 6. Basic OCT system, implementing a Michelson interferometer. From [7].

Light from a low-coherence light source, is directed towards a beam splitter where it is split into a reference arm and a sample arm. Light travelling in the reference arm is reflected on a reference mirror and re-directed to the beam splitter. Light travelling in the sample arm is reflected by the multiple layers within the sample at study and also re-directed to the beam splitter. Then, both reflected beams arriving at the beam splitter will interfere, forming an interference pattern that is detected by a photodetector.

Note that the reference mirror is static, in the Fourier domain approaches (Spectral and Swept Source), and is a moving part in the case of Time domain OCT. These modalities of Optical Coherence Tomography and their respective differences are discussed in detail in section 1.3. Also it is important to note that the information acquired from the sample depends on the type of scanning method applied, namely A-scan, B-scan or C-scan which are discussed and compared in section 1.4.

Next, a presentation of a mathematical formulation for OCT is given.

1.2.4 Theoretical formulation

A mathematical model for OCT is now presented, based on Figure 6. The electric field that describes the light wave emitted by the source and enters the beam splitter is expressed in the complex form [1]:

$$E_{in} = s(k,\omega)e^{i(kz-\omega t)} \tag{3}$$

where $s(k,\omega)$ represents the electric field amplitude as a function of the angular frequency $\omega = 2\pi\nu$ and wavenumber $k = \frac{2\pi}{\lambda}$, which are respectively the temporal and spatial frequencies of each spectral component of the field having wavelength λ. The wavelength λ and frequency ν are related through the index of refraction $n(\lambda)$ (which is wavelength-dependent in a dispersive media) and the vacuum speed of light c according to the relation $\frac{c}{n(\lambda)} = \lambda\nu$. In Figure 6, E_{in} represents the input electric field at the beam splitter (corresponding to the electric field emitted by the source), E_{out} represents the beam splitter's output electric field that is directed towards the photodetector, and E_r and E_s are the beam splitter's input electric fields after reflection by the reference mirror and the sample, respectively.

For this deduction, it is considered an ideal beam splitter, i.e., lossless, with an achromatic power splitting ratio yielding $T_r + T_s = 1$ (T_r and T_s being the intensity transmission coefficients for the reference and sample arms, respectively), and an ideal reflector in the reference arm, with an electric field reflectivity r_R and power reflectivity $R_r = |r_R|^2$. Also, the distance from the beam splitter to the reference arm is z_r.

Due to the depth-dependence of the sample's electric field reflectivity profile along the axial direction (beam propagation), the sample reflectivity $r_s(z_{s_n})$ (where z_{s_n} is the variable path length between the beam splitter and the n^{th} reflective surface) is, generally, a continuous complex function containing both phase and amplitude information of each reflection [1]. For this exercise, however, we assume a simplified description given by a set of *N* discrete, real delta-function reflections within the sample [1]:

$$r_s(z_s) = \sum_{n=1}^{N} r_{s_n} \delta(z_s - z_{s_n}) \tag{4}$$

This equation represents each electric field reflectivity $(r_{s_1}, r_{s_2}, \dots, r_{s_N})$ and their corresponding path-lengths $(z_{s_1}, z_{s_2}, \dots, z_{s_N})$. The electric field reflectivity of each layer of the sample can be obtained by applying the Fresnel's equations $r_{s_n} = \frac{n_{n+1} - n_n}{n_{n+1} + n_n}$, where n_n represents the refractive index of the n^{th} layer. Therefore, the reflectivity profile is a representation of the changes in refractive index within the sample. The respective power reflectivity of each reflective surface is $R_{s_n} = |r_{s_n}|^2$.

The expression that gives the sample's response function, i.e., the overall reflection from all structures within the sample in the beam propagation direction is [7]:

$$H(k,z) = \sum_{n=1}^{N} r_{s_n} e^{2in(k,z)\frac{kz}{c}} \tag{5}$$

where $n(k,z)$ is the wavelength dependent, depth varying group refractive index.

Based on these considerations, it is now possible to mathematically describe the processes involved in the OCT system represented in Figure 6. Thus, the electric fields E_r, E_s and E_{out} can be written as [7]:

$$E_r(k,z) = (T_r T_s)^{\frac{1}{2}} E_{in} r_R e^{2ikz_r} \tag{6}$$

$$E_s(k,z) = (T_r T_s)^{\frac{1}{2}} E_{in} H(k,z) \tag{7}$$

$$E_{out}(k,z) = E_r + E_s = (T_r T_s)^{\frac{1}{2}} E_{in}\left[H(k,z) + r_R\, e^{2ikz_r}\right] \tag{8}$$

As mentioned above, the output electric field of the beam splitter is directed towards a photodetector. Since optical detectors are square law irradiance detection devices, the recorded light irradiance is directly proportional to a time average over the electric field, multiplied by its complex conjugate [7], and therefore:

$$I(\omega,k) = \lim_{t\to\infty} \frac{1}{2T}\rho \int_{-T}^{T} E_{out}\; E_{out}^{*}\, dt \tag{9}$$

where ρ is the responsivity factor of the detector. Using a bracket notation representing a time-average for simplification:

$$I(\omega,k) = \rho\langle E_{out}\; E_{out}^{*}\rangle \tag{10}$$

Replacing E_{out} as defined in Equation 8, yields:

$$I(\omega,k) = \rho\langle (E_r + E_s)(E_r + E_s)^{*}\rangle \tag{11}$$

$$\Leftrightarrow I(\omega,k) = \rho\langle |E_r + E_s|^2\rangle \tag{12}$$

Substituting E_r and E_s as defined in Equations 6 and 7, resolving the magnitude squared function, and simplifying through Euler's formula yields the usually called "spectral interferogram" [1]:

$$\begin{aligned} I(k) = \rho T_r T_s S(k) \Bigg\{ & \left[R_r + R_{s_1} + \cdots + R_{s_N}\right] \\ & + \left[\sum_{n=1}^{N} \sqrt{R_r R_{s_n}}\, \cos\left(2k\left(z_r - z_{s_n}\right)\right)\right] \\ & + \left[\sum_{n\neq m=1}^{N} \sqrt{R_{s_n} R_{s_m}}\, \cos\left(2k\left(z_{s_n} - z_{s_m}\right)\right)\right] \Bigg\} \end{aligned} \tag{13}$$

where $S(k) = \langle |s(k,\omega)|^2\rangle$ represents the spectral intensity of the light source. Equation 13 contains three distinct contributions for the detector photocurrent $I(k)$. The first term, called "incoherent term", is the contribution due to the incoherent sum of light, which is independent of the path length difference and has an amplitude proportional to the power reflectivity of the reference mirror, R_r, plus the sum of the sample structure's power reflectivity, $R_{s_1} + \cdots + R_{s_n}$.

The second term in Equation 13, "cross-correlation term" or "cross-interference term", is dependent on the path length difference between the reference arm and sample reflectors, $z_r - z_{s_n}$, and the wavenumber k. Also, it is the desired component of the OCT signal, since it cross-correlates the signals from the reference and the sample reflectors.

The third and final term of the equation is called "auto-correlation term" and corresponds to the interference occurring between different structure reflections.

As stated before, Equation 13 represents the detector photocurrent $I(k)$ of the generic OCT system, previously analyzed. Furthermore, this result can be specified to both Time and Fourier domains techniques. Thus, a discussion of their respective detector photocurrent equations is appropriate while presenting a detailed description of the OCT modalities, in the next section of this thesis.

1.3 OCT modalities

In Optical Coherence Tomography the depth information of a sample can be obtained by different methods, according to the OCT approach used. Figure 7 presents a scheme with the various OCT modalities that will be described in this section.

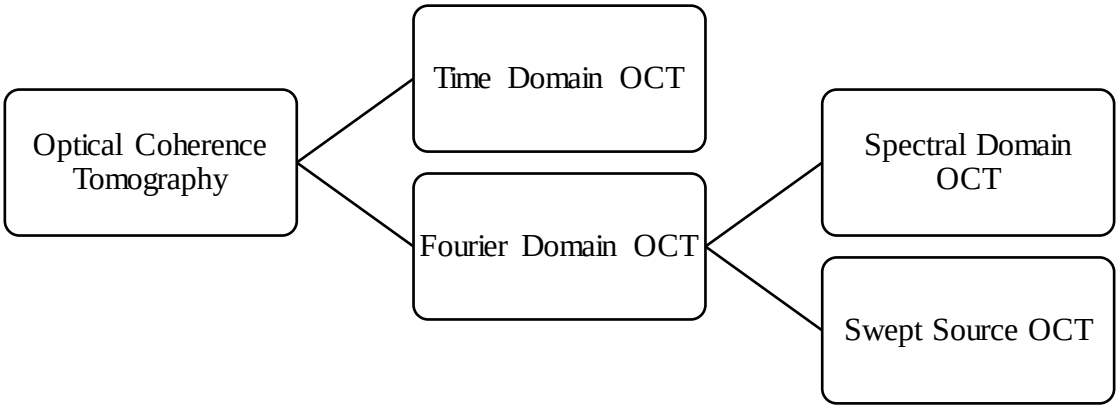

Figure 7. Optical Coherence Tomography modalities.

The first modality developed, the Time Domain OCT, is based on a moving reference mirror to obtain the depth information. Later, the Fourier Domain was introduced, first with the Spectral followed by Swept Source techniques, both characterized by the absence of moving parts.

1.3.1 Time Domain OCT

The first approach for the OCT imaging technique was the Time domain OCT (TD-OCT), schematically represented in Figure 8. The scanning of the consecutive (in depth) structures of the sample in the axial direction is done by sweeping the mirror's position, z_r, along the axial direction of the reference arm, consequently changing the light's path length. Thus, each path length in this arm is matched to a different path length in the sample arm, and therefore, a different depth within the sample.

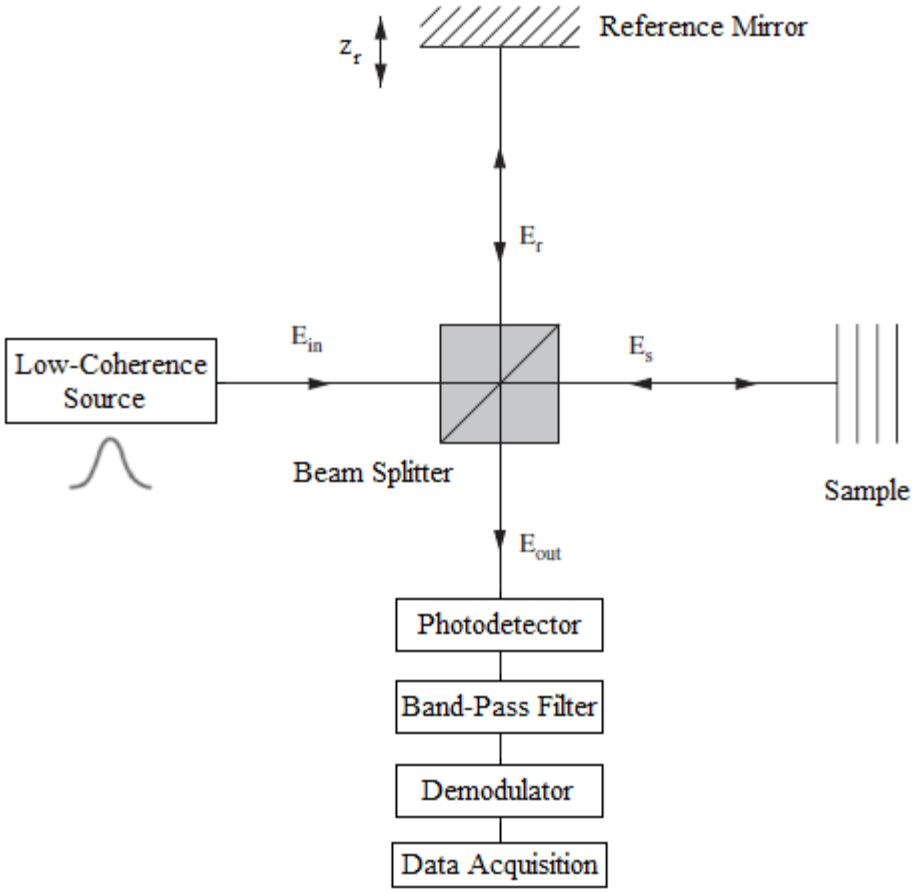

Figure 8. Time Domain OCT system. Adapted from [7].

The mathematical expression for the photodetector current, as a function of the reference path length, can be obtained for the Time domain OCT by integration over the source spectrum, i.e., over the wavenumber values k:

$$I(\Delta z_r) = \int_0^{+\infty} I(k)dk \tag{14}$$

yielding an expression similar to the result obtained in Equation 13 [1]:

$$I(\Delta z_r) = \rho T_r T_s S_0 \left\{ \left[R_r + R_{s_1} + \cdots + R_{s_N} \right] + \left[\sum_{n=1}^{N} \sqrt{R_{s_n} R_r}\, e^{-[(z_r - z_{s_n})\Delta k]^2} \cos(2k_0(z_r - z_{s_n})) \right] \right\} \quad (15)$$

where $S_0 = \int_0^{+\infty} S(k)dk$ is the integration of the power emitted by the light source over its spectrum. Equation 15 is composed by two terms, a DC offset equal to the first term of Equation 13 already discussed, and a second term, that modulates the interferogram (Figure 9). One of two modulation factors is a sinusoidal carrier wave at a frequency proportional to the source's central wavenumber k_0, influencing the rapid oscillations seen the interferogram. The other modulation factor is the exponential factor that controls the Gaussian shape of each envelope corresponding to each reflection, whose respective amplitude is given by the pre-exponential factor $\sqrt{R_{s_n} R_r}$. Please note that the reflections present a Gaussian-shaped envelope because we considered an ideal light source, with a Gaussian power spectrum. The envelope shape is determined by Fourier transform of the power spectrum of the light source, as dictated by the Wiener theorem.

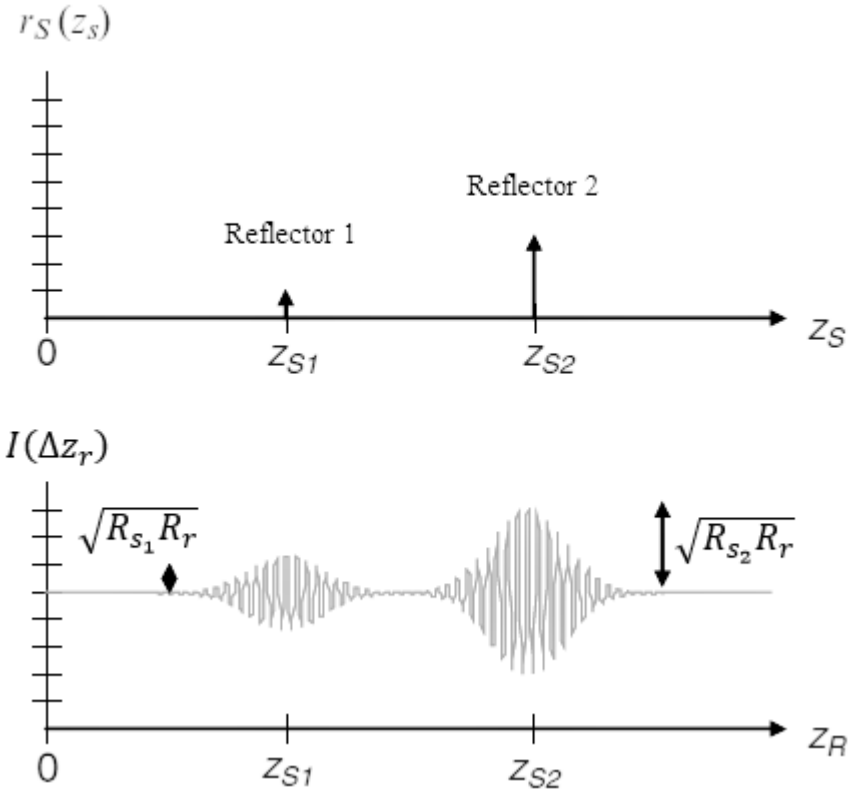

Figure 9. Example of sample containing two reflectors (up) and the respective recorded interferogram (bottom). Adapted from [1].

The interference signal presented in Figure 9 can be interpreted as the "raw" data/signal generated by the photodetector. As presented in Figure 8, this signal is band-pass filtered and is then demodulated, for obtaining the intensity peaks that represent the reflecting structures along the optical axis within the sample, known as the A-scan (section 1.4).

1.3.2 Fourier Domain OCT

The OCT approaches in the Fourier domain, Spectral Domain OCT (SD-OCT) and Swept Source OCT (SS-OCT), use a static reference mirror and the reflectivity depth profile of the sample is created from the Fourier analysis of the acquired reflection's (intensity spectrum) across the laser frequency range. The difference between the two Fourier approaches lies on the type of light source used and interference detection.

Spectral Domain OCT

Figure 10 depicts a schematic of Spectral domain OCT. The light source used in this approach is of the low-coherence (broadband) type. As light back scattered by the sample's structures interferes with light reflected by the reference arm, the resulting interference is directed into a spectrometer. The spectrometer breaks light into its spectral components, which are then directed towards a detector array (e.g. a CCD camera or a photodiode array), where each spectral component of the interference signal is simultaneously measured. This OCT approach can also be called *spatially encoded* FD-OCT since the detected spectrum is spatially distributed across the detection array. After the data acquisition, resampling of the spectral components in the frequency space (k-space) is needed in order to be able to perform the inverse Fourier transform and gain access to the encoded depth information of the sample (A-scan).

It is relevant to place here a brief consideration on the Wiener Theorem, a result of great importance to Fourier analysis in OCT. It is assumed that a Gaussian shaped light source is used. In consequence, the normalized Gaussian function $S(k)$ and its inverse Fourier transform $\gamma(z)$ are related by:

$$\gamma(z) = e^{-z^2\Delta k^2} \overset{FT}{\leftrightarrow} S(k) = \frac{1}{\Delta k\sqrt{\pi}} e^{-\left(\frac{k-k_0}{\Delta k}\right)^2} \tag{16}$$

where k_0 is the central wavenumber and Δk is the bandwidth of the light source spectrum. Applying the inverse Fourier transform to Equation 13, making use of the Fourier transform property relations $\frac{1}{2}[\delta(z+z_0)+\delta(z-z_0)] \overset{FT}{\leftrightarrow} \cos(kz_0)$ and $x(z) \otimes y(z) \overset{FT}{\leftrightarrow} X(z)Y(z)$, where $\otimes$ represents the convolution operation, yields [1]:

$$I(z) = \rho T_r T_s \left\{ \gamma(z)\left[R_r + R_{s_1} + \cdots + R_{s_N}\right] + \left[\gamma(z) \otimes \sum_{n=1}^{N} \sqrt{R_r R_{s_n}}\, \delta\left[z \pm 2\left(z_r - z_{s_n}\right)\right]\right] + \left[\gamma(z) \otimes \sum_{n \neq m=1}^{N} \sqrt{R_{s_n} R_{s_m}}\, \delta\left[z \pm 2\left(z_{s_n} - z_{s_m}\right)\right]\right]\right\} \quad (17)$$

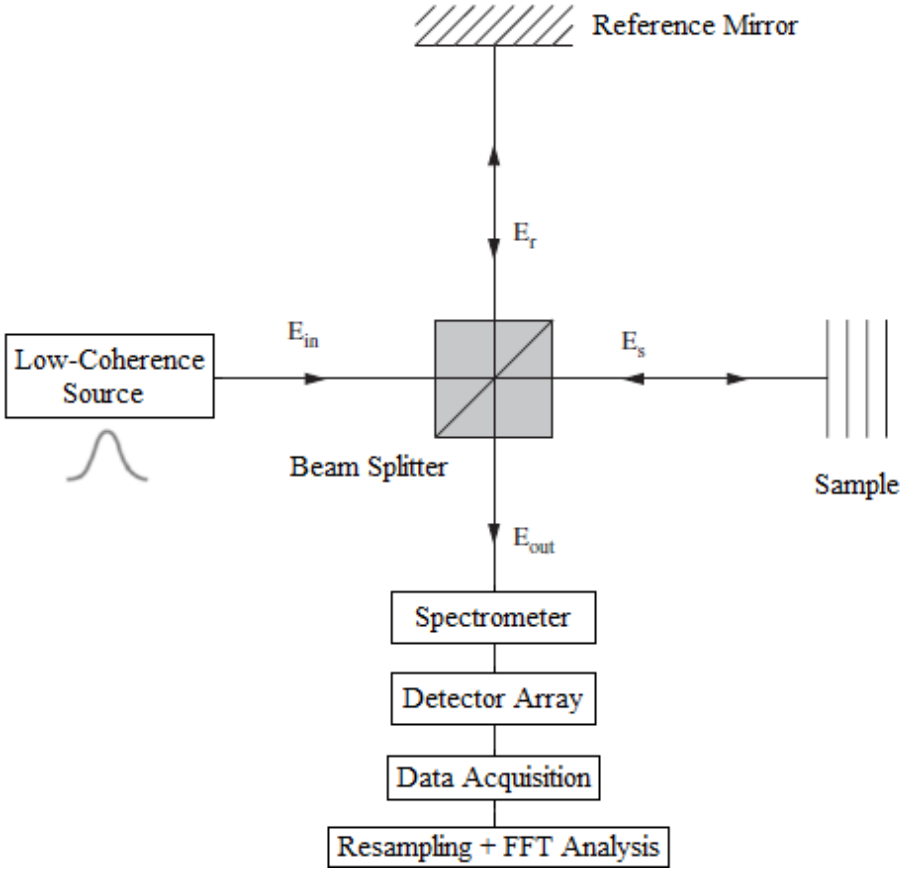

Figure 10. Spectral Domain OCT system. Adapted from [7].

The relevant information for the sample reflectivity profile is embedded in the "cross-correlation term", the second term in Equation 17. As such, the A-scan is obtained by [1]:

$$I(z) = \rho T_r T_s \left\{ \gamma(z)\left[R_r + R_{s_1} + \cdots + R_{s_N}\right] + \left[\sum_{n=1}^{N} \sqrt{R_r R_{s_n}}\, \gamma\left[2\left(z_r - z_{s_n}\right) - 2\left(z_r - z_{s_n}\right)\right]\right] + \left[\sum_{n \neq m=1}^{N} \sqrt{R_{s_n} R_{s_m}}\, \gamma\left[2\left(z_{s_n} - z_{s_m}\right) - 2\left(z_{s_n} - z_{s_m}\right)\right]\right]\right\} \quad (18)$$

Figure 11 presents the $I(z)$ signal (A-scan) obtained by means of the Fourier transform of a Fourier Domain OCT system signal from a sample with two reflecting surfaces. The second term represents the cross-correlation terms, the signal of interest for the application field at hand. The relative displacement between reflectors is twice the real distance due to the round-trip distance measured by the interferometer. Additionally, these terms appear mirrored with respect to the DC component due to the nature of the Fourier transform [1]. These "mirror image artifacts" can be ignored by displaying only half of the signal.

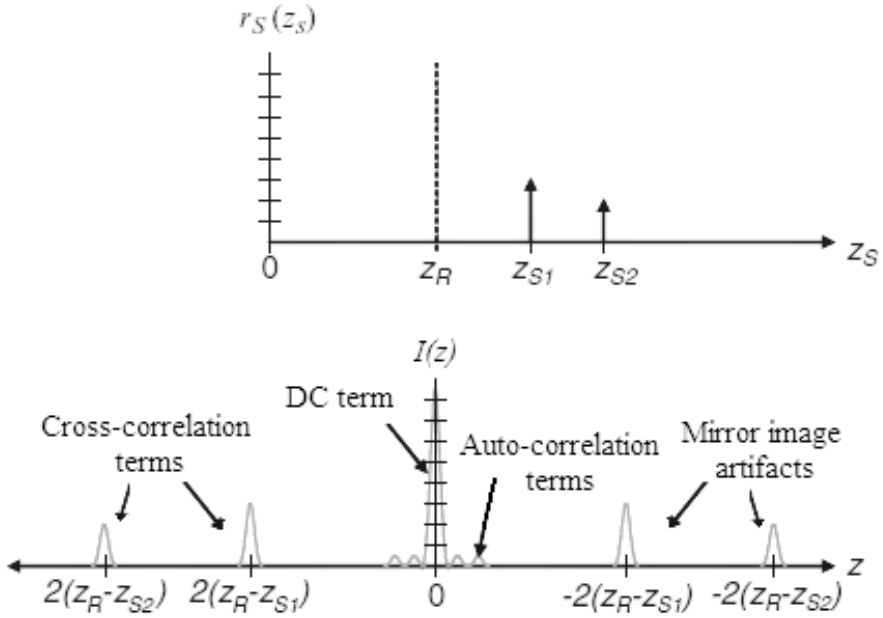

Figure 11. Example of a two sample containing two reflective structures (up) and the respective I(z) signal obtained from Fourier Domain OCT (bottom). Adapted from [1].

Swept Source OCT

In this approach, a narrowband laser source is used whose frequency is swept across its spectral range (frequency-swept narrowband source). As such, neither a spectrometer nor a detector array are required. A single photodetector is used for detecting the interference signal, as presented in Figure 12. While in Spectral Domain OCT the spectral components of the interference light are spatially separated, in the Swept Source OCT, also referred to as *temporally encoded FD-OCT*, they are encoded in time, meaning that the Fourier transform is carried on the temporal output of the single photodetector, over the period of time that it takes to sweep over the wavelength range of the light source [9].

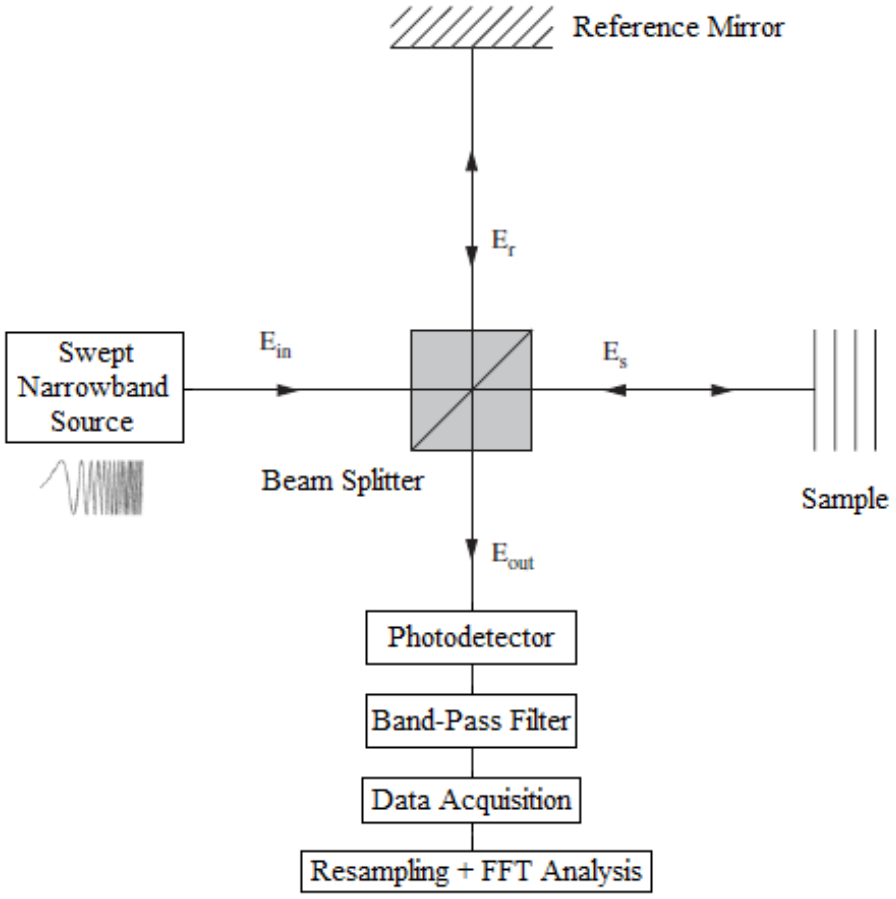

Figure 12. Swept Source OCT system. Adapted from [7].

The signal processing involved in Swept Source OCT is the same as the one described for Spectral Domain OCT. However, the mathematical description of the signal is a little different, due to the nature of the laser output. Since the laser source is a swept source (i.e. its output wavelength changes with time), the wavenumber of the light is a linear function of time [8]:

$$k(t) = k_0 + \frac{\Delta k}{\Delta T} t \tag{19}$$

where k_0 is the initial wavenumber, Δk is the wavenumber bandwidth, and ΔT is the sweeping period (inverse of the sweep frequency). Thus, the "spectral interferogram" is obtained as a time-sequential signal [8] and can be described by rewriting Equation 13:

$$\begin{aligned} I(k) = \rho T_r T_s S(k) \Bigg\{ & \left[R_r + R_{s_1} + \cdots + R_{s_N} \right] \\ & + \left[\sum_{n=1}^{N} \sqrt{R_r R_{s_n}} \cos\left(2 \left[k_0 + \frac{\Delta k}{\Delta T} t \right] \left(z_r - z_{s_n} \right)\right) \right] \\ & + \left[\sum_{n \neq m = 1}^{N} \sqrt{R_{s_n} R_{s_m}} \cos\left(2 \left[k_0 + \frac{\Delta k}{\Delta T} t \right] \left(z_{s_n} - z_{s_m} \right)\right) \right] \Bigg\} \end{aligned} \tag{20}$$

Both cross-correlation and auto-correlation terms will oscillate with an angular frequency $\alpha = 2\frac{\Delta k}{\Delta T}\Delta z$ proportional to the sweeping frequency $\frac{1}{\Delta T}$, the wavenumber bandwidth Δk, and the light's path difference between the sample and reference arms.

This expression is similar to Equation 13. However, the wavenumber is time-dependent. Ultimately, in terms of information contained in the equations that describe the photocurrent measured in Spectral and Swept Source domains, Equations 18 and 20 carry the same information. The difference lies in the spectral representation of the interference signal due to the dependence in the period (and consequently, the frequency) of the wavelength sweep of the laser source. Thus, Figure 11 can also describe the signal obtained for a Swept Source OCT, namely the terms and the artefacts observed and previously discussed.

1.4 Scanning methods

The present section provides a brief description of the different types of scans available to Optical Coherence Tomography. The most important ones, when considering the biomedical imaging and the clinical diagnosis, are the A, B and volume scans. These applications require depth-resolved high resolution structural information from the sample.

The basic scan type is the A-scan (amplitude scan). It provides the reflectivity profile at the beam's focusing spot along the light propagation direction.

The acquisition of consecutive A-scans along a line in the transverse direction enables the build of a two-dimensional cross-sectional image of the sample, named B-scan (brightness scan).

Multiple (normally parallel) B-scans allow for the volume imaging of the sample at study.

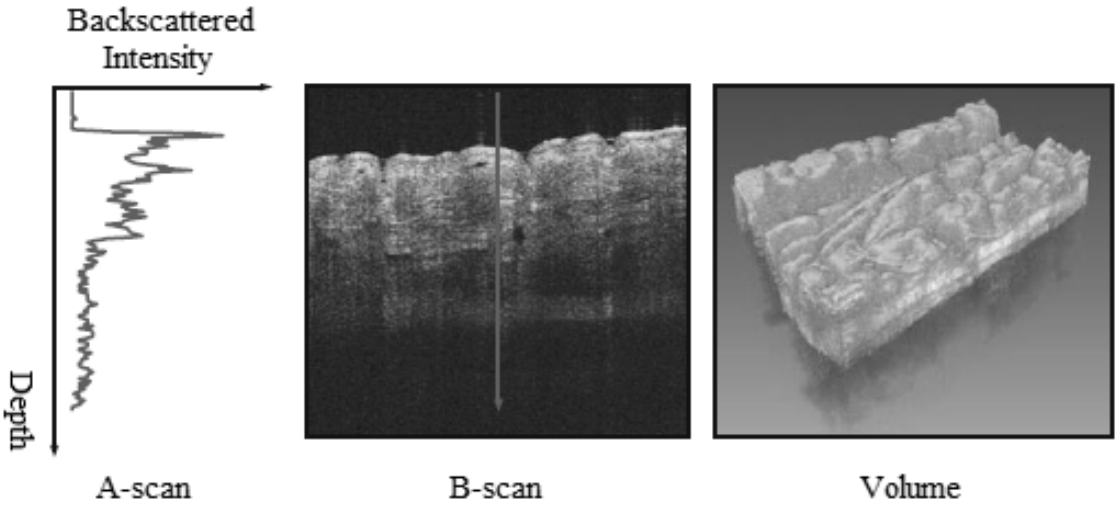

Figure 13. Examples of the different types of scans: A-scan (left), B-scan (middle), Volume (right). From [10].

A galvanometric scanning system is used to scan different points of the sample, changing the position of the focusing beam along two directions, X and Y, both transverse to the beam's propagation direction Z. This system has two mirrors, X-mirror and Y-mirror, working synchronously – when the X-mirror completes a scan of the sample, the Y-mirror changes its position and the X-mirror repeats the scan, until all the sample is scanned.

After acquiring every desired scan, the reconstruction of the sample's image and/or volume, either displayed in a gray scale or with false color, is achieved through data processing.

1.5 Performance parameters in OCT

The assessment of the system performance is of major importance, not only to understand its current development state, but to conclude about its accuracy. In this section, the theoretical treatment of the parameters to be analyzed, the experimental methods for their determination and some standard values are presented. Since this thesis work was

experimentally conducted using a Swept Source OCT system, the analysis given will be based and directed towards this architecture.

Firstly, a brief discussion of the Point Spread Function (PSF) concept is needed, since it is the type of signal registered in order to determine and analyze most of the performance parameters. The PSF is described as the focused optical system's response to a point object (i.e. impulse). Ideally it assumes a Dirac pulse shape. However, since in reality a perfect imaging system does not exist, the PSF shape is similar to the one depicted in Figure 14. The PSF signal is obtained by Fourier transformation of the interference signal when the sample is a mirror, and its shape is determined by the shape of the power spectrum of the light source, following the Wiener theorem. In these conditions the A-scan describes a single reflective surface.

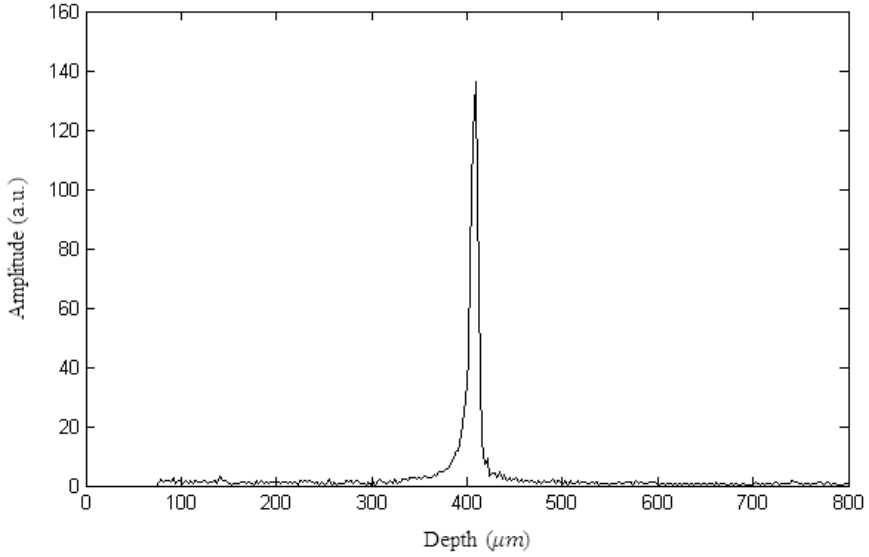

Figure 14. Axial Point Spread Function (PSF) acquired from analysis of a gold mirror.

1.5.1 Axial resolution

One of the most important performance parameters of an OCT system is its depth resolution, describing the system's ability to distinguish two consecutive interfaces along the light beam's propagation direction. For the target application, imaging rodent's retinas, this parameter represents the ability to discriminate the different structures of the retina.

As demonstrated by Fercher *et al.* (section 1.1), there is a correlation between the axial resolution and the coherence length of the light. Assuming that the power spectrum of the

light source is described by a Gaussian function, a well-established approximation in the OCT community, the axial resolution is defined as half the coherence length. The axial resolution is defined by the optical parameters of the source, namely its central wavelength λ_0 and spectral full-width at half maximum $\Delta\lambda$ [7]:

$$\Delta z = \frac{l_c}{2} = \frac{2\ln 2}{\pi}\frac{{\lambda_0}^2}{\Delta\lambda} \tag{21}$$

Equation 21 establishes the maximum achievable value for the axial resolution of a given OCT system based on its light source. Nonetheless, due to dispersion effects in the system and the assumption of the Gaussian shaped light source this limit is not experimentally achieved. For a Swept Source OCT system, the limit value for the axial resolution, due to the light source characteristics only, can be established by measuring the spectrum of the light source using an optical spectrum analyzer and determine the Full-Width at Half Maximum (FWHM) of the Fourier transformed spectrum [11].

Experimentally, the axial resolution of the entire OCT system can be estimated by the analysis of an A-scan from a gold coated mirror. An A-scan in these conditions is depicted in Figure 14. The FWHM can be computed by fitting a Lorentzian function to the acquired data points, being the Lorentzian given by:

$$f(x) = y_0 + \frac{2A}{\pi}\frac{w}{4\,(x - x_c)^2 + w^2} \tag{22}$$

where the w parameter is the FWHM to be determined through an optimization procedure (the software Origin was used in this work). The remaining parameters – y_0 is an offset, A is the area under the curve and x_c the coordinate of the peak – are not important to the resolution.

For biomedical applications, it is commonly accepted that in order to acquire images with enough quality to extract good conclusions, the axial resolution in tissue of the OCT system must better (i.e. less) than 10 μm [12].

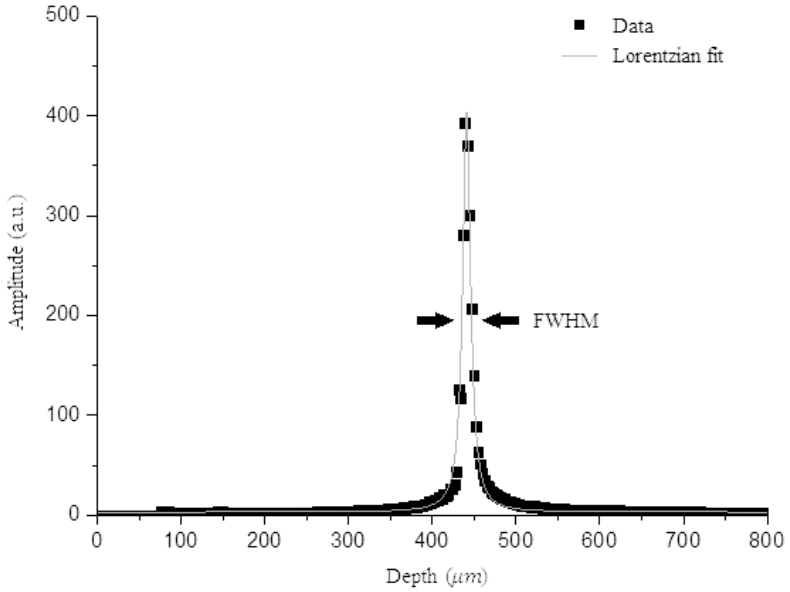

Figure 15. Lorentzian curve fitting (Origin software) to PSF data points acquired for axial resolution determination.

1.5.2 Lateral resolution and depth-of-focus

Similar to the axial resolution, the lateral resolution of an OCT system describes the system's ability to discriminate between two adjacent points as separate ones in the transverse direction to the light beam's propagation. It is defined as [7]:

$$\Delta x = 1.22 \frac{\lambda_0}{2NA_{obj}} \tag{23}$$

where NA_{obj} is the numerical aperture of the objective lens used to focus the light beam into the sample. Although higher numerical apertures lead to better lateral resolution, they also lead to a worsening of the OCT system's depth-of-focus (see Figure 16), representing the maximum penetration distance (due to optics only) within the sample from which information can be retrieved, given by [7]:

$$b = 2 \frac{n \lambda_0}{NA_{obj}^2} \tag{24}$$

where n represents the sample's refractive index.

In consequence, a compromise towards the best equilibrium between the depth-of-focus and lateral resolutions is required and needs to be established taking into account the system's target application.

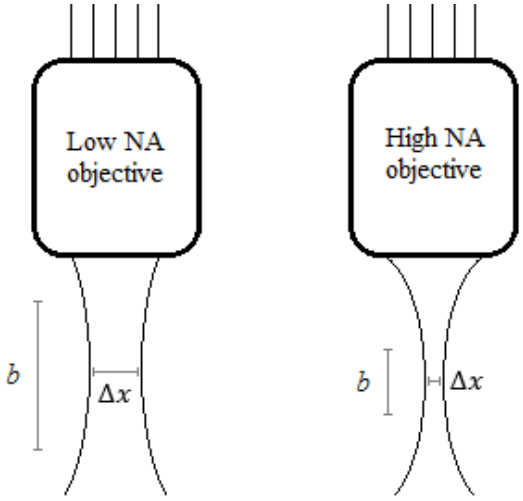

Figure 16. Representation of lateral resolution and depth of focus dependence with NA aperture of objective.

1.5.3 Sensitivity

Sensitivity is a measure of the smallest sample reflectivity, $R_{s,min}$, detected by the system. It is obtained by the signal level at which the signal-to-noise ratio (SNR) equals one. It is expressed, in terms of $R_{s,min}$, in dB units, by [13]:

$$S_{dB} = 10 \log_{10}\left(\frac{1}{R_{s,min}}\right) \tag{25}$$

Experimentally, the sensitivity value of a given OCT system can be determined by placing a neutral density filter of a known optical density ($OD = 2$) before a gold mirror used as sample (considered a perfect reflector). Light travelling into and from the sample arm will be doubly attenuated by this filter, resulting in an equivalent sample reflectivity of 10^{-4} ($-OD \times 2 \times 10 = -40\ dB$). The noise level (in dB units) of an acquired PSF under these conditions corresponds to the sensitivity of the OCT system. From the obtained value and inverting Equation 25, $R_{s,min}$ can be determined.

Similarly to the axial resolution, there is a commonly accepted minimum value required for the sensitivity that an OCT system must achieve, being it of $S_{dB} = 95\ dB$ ($R_{s,min} = 3.16 \times 10^{-10}$)[12].

1.5.4 Sensitivity roll-off

The sensitivity of any OCT system depends on the imaging depth within the sample and characterizes the system's ability to image in depth. In swept source OCT, the decrease in signal amplitude with increase in depth (sensitivity roll-off), which is a consequence of distinct factors related to the OCT instrumentation. First, the limited spectral resolution that, for swept source OCT, is a consequence of the swept laser linewidth [10]. This effect can be modelled by convolving the ideal spectrogram with a Gaussian function representing the spectral resolution. Consequently, the ideal A-Scan will be multiplied by a Gaussian term given by the inverse Fourier transform of the spectral resolution function, resulting in an exponential roll-off. This contribution to sensitivity decrease is usually viewed as the decreasing visibility of higher fringe frequencies corresponding to higher depths.

Another cause for the sensitivity roll-off is the limited bandwidth of the OCT electronic amplifier. Higher electronic frequencies correspond to larger sample depths.

Experimentally, the sensitivity roll-off is determined by the acquisition of consecutive A-scans and by determination of the respective PSF maximum for various reference mirror positions. The slope is thereafter determined by fitting a line to the maximum of the PSF (Figure 17). Sensitivity roll-off is established in dB/mm units.

A good sensitivity roll-off value for an OCT system is commonly stated at no more than 10 dB/mm [12], since this parameter restricts the imaging depth.

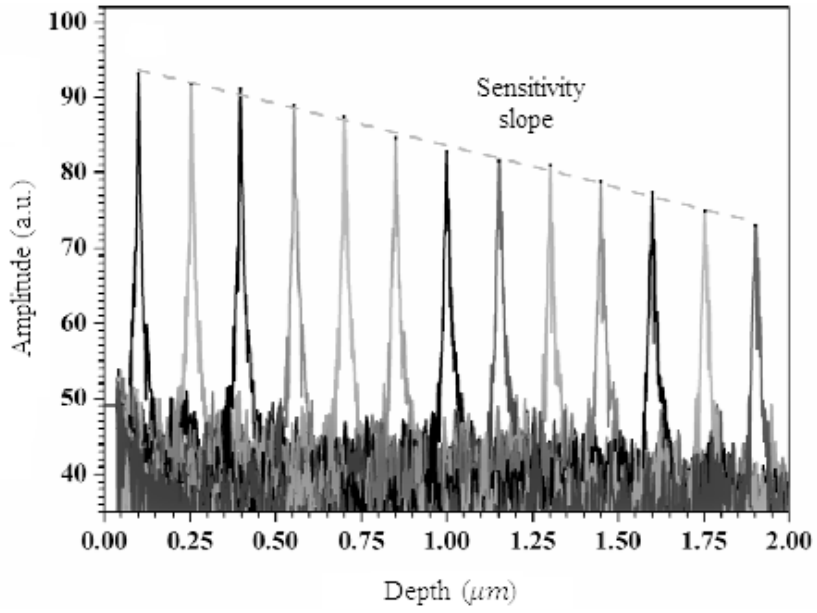

Figure 17. Representation of sensitivity roll-off acquired signals, superimposed in one single graph. Adapted from [13].

1.5.5 Dynamic range

The dynamic range of an OCT is defined as the ratio between the maximum and minimum signal intensities (in dB units) detected in the same A-scan, and is described by:

$$D_{dB} = 20 \log_{10}\left(\frac{PSF_{max}}{\sigma_{noise}}\right) \tag{26}$$

Similarly to the sensitivity measurement, the dynamic range is determined by acquiring a PSF using a gold coated mirror as sample (see Figure 14), but this time a single PSF is acquired and no filter is used. The maximum intensity recorded corresponds to the PSF peak, PSF_{max}, and the smallest is defined by the standard deviation of the noise σ_{noise}. As mentioned above, to calculate the sensitivity value, the standard deviation of the noise is obtained through acquisition of a separated PSF function.

For biomedical imaging it is often required for the dynamic range of an Optical Coherence Tomography system to be at least $40 - 50\ dB$ [12], since most OCT images have around $35\ dB$ of dynamic range.

1.5.6 Noise

In order to better understand the signal-to-noise ratio (SNR) parameter discussed next in this thesis, it is important to get to know the main contributions to noise within the OCT.

In the following discussion only light emission and detection noise sources are considered, therefore leaving out other sources like the speckle. In this way, three key contributions can be highlighted: shot noise, thermal noise and excess photon noise.

Shot noise

Shot noise describes the current fluctuations due to quantization of photons, a consequence of the quantum nature of light. Although charge is generated at a photodetector corresponding to a mean rate defined by the photocurrent, the elapsed time between specific emissions is random [14]. So, the instants corresponding to both the photon arrival and the electron emission are described by a Poisson distribution. Thus, the photocurrent variance that results from this intrinsic uncertainty is given by [16]:

$$i_{shot}^2 = 2\, e\, \bar{I}_s\, \Delta f \tag{27}$$

where e represents the electron charge, $\bar{I}_s$ is the detector's mean photocurrent and Δf is the detector's bandwidth.

Thermal noise

Thermal noise, also known as Johnson noise, arises from the ever constant movement of charge carriers due to the thermal energy present in any resistive element. It is related to the temperature equilibrium and to the transfer of energy between any resistor and its surroundings [15]. It is described by [7]:

$$i_{thermal}^2 = \frac{4\, k_B\, T \Delta f}{R} \tag{28}$$

where $k_B$represents the Boltzmann's constant, T is the absolute temperature (in Kelvin), Δf is the detector's bandwidth and R the resistor.

Excess photon noise

Excess photon noise refers to the fluctuations in the output intensity of the light source due to the beating of different spectral components with random phases, and is given by [16]:

$$i_{excess}^2 = \frac{(1+\alpha^2)\, \bar{I}_s\, \Delta f}{\Delta v} \tag{29}$$

where α represents the degree of polarization of the source, $\bar{I}_s$ is the detector's mean photocurrent, Δf is the detector's bandwidth and Δv the effective linewidth of the source.

1.5.7 Signal-to-noise ratio (SNR)

The concept of signal-to-noise ratio is present over a wide range of scientific and engineering subjects when instrumentation is involved. It relates the level of the signal, carrying useful information, with the level of the background noise. The SNR is defined as the ratio between the powers of the signal, P_{signal}, and the noise, P_{noise}:

$$SNR = \frac{P_{signal}}{P_{noise}} \tag{30}$$

commonly expressed in decibels (dB), through the logarithmic expression:

$$SNR_{dB} = 10 \log_{10}\left(\frac{P_{signal}}{P_{noise}}\right) \quad (31)$$

The power of the signal is defined by the mean square signal photocurrent, $\langle {i_D}^2 \rangle$, which, for a single detector, can be written as [16]:

$$\langle {i_D}^2 \rangle = 2\rho^2 P_r P_s \quad (32)$$

where ρ represents the detector's responsivity, and P_r and P_s are the optical power in the reference and sample arms, respectively. The background noise power is estimated by the noise variance, defined as the sum of the squared noise contributions aforementioned [16]:

$$\sigma^2_{noise} = i^2_{shot} + i^2_{thermal} + i^2_{excess} \quad (33)$$

Equation 31 can be rewritten as:

$$SNR_{dB} = 10 \log_{10}\left(\frac{\langle {i_D}^2 \rangle}{\sigma^2_{noise}}\right) = 10 \log_{10}\left(\frac{2\rho^2 P_r P_s}{i^2_{shot} + i^2_{thermal} + i^2_{excess}}\right) \quad (34)$$

Due to the low optical intensities reflected/backscattered by biological tissues, it is fundamental that biomedical imaging techniques present a high SNR value.

1.6 OCT Applications

Optical Coherence Tomography is a powerful and noninvasive imaging technique capable of rapidly acquiring high resolution images of tissue samples, and so it plays a very important role in clinical fields like ophthalmology and cardiology, as well as in biomedical investigation.

For ophthalmology purposes, OCT provides detailed structural information of the human eye through noninvasively and contactless analysis, allowing for the imaging of the anterior and posterior segments (see Figure 18 for an example of a posterior, macular, segment), facilitating the early diagnosis of pathologies like glaucoma [17], age-related macular degeneration [18] and diseases associated with the central nervous system, like multiple sclerosis [19], by analyzing morphology changes in the retinal nerve fiber layer [17]. In addition, monitoring the patient's response to treatment through this technique allows for a better understanding of disease pathogenesis [20].

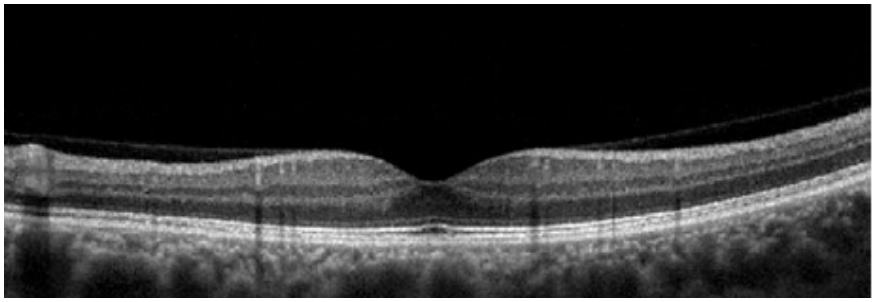

Figure 18. Macula cross sectional image. From [17].

In cardiology, intravascular imaging can be acquired with OCT (Figure 19), similar to intravascular ultrasound, but with ten times the resolution [21]. Using a catheter probe simultaneously with a clearing agent, to displace the blood and consequently preventing the strong attenuation of light due to hemoglobin, it is possible to obtain a clear view of the coronary artery wall, so that coronary artery disease can be assessed [22]. Other pathologies like coronary atherosclerosis [22], spontaneous coronary dissection [23] or cardiac allograft vasculopathy [24] can be evaluated. Moreover, due to OCT high spatial resolution, evaluation of vascular response to percutaneous coronary intervention and guidance during the procedure is possible with this technique [22].

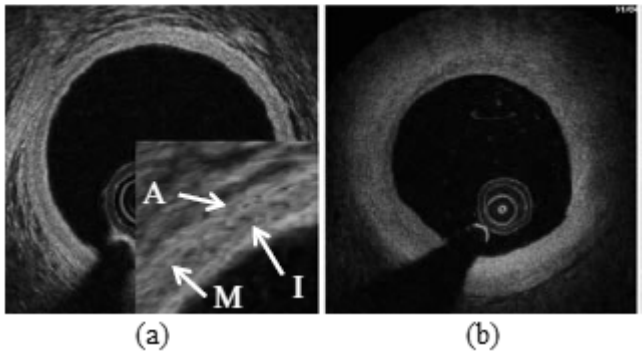

Figure 19. Coronary artery images acquired using OCT. (a) Normal coronary artery is structured into intima (I), media (M) and adventitia (A), clearly visualized by OCT. (b) Pathologic intimal thickening – with progression of atherosclerosis, the border between intima and media becomes diffuse. From [22].

Furthermore, functional information such as blood flow velocities can be obtained by acquisition and processing of phase information from the sample at study. Usually called Doppler OCT, this phase-sensitive technique allows for the reconstruction of the intensity images as well as the velocity profiles within the sample, as presented in Figure 20.

Many other applications for Optical Coherence Tomography, either in medicine branches like dermatology, gynecology, oncology, etc. or even in completely different fields like material testing or artwork examination, are described in "Part V: OCT Applications" of the book *Optical Coherence Tomography - Technology and Applications*.

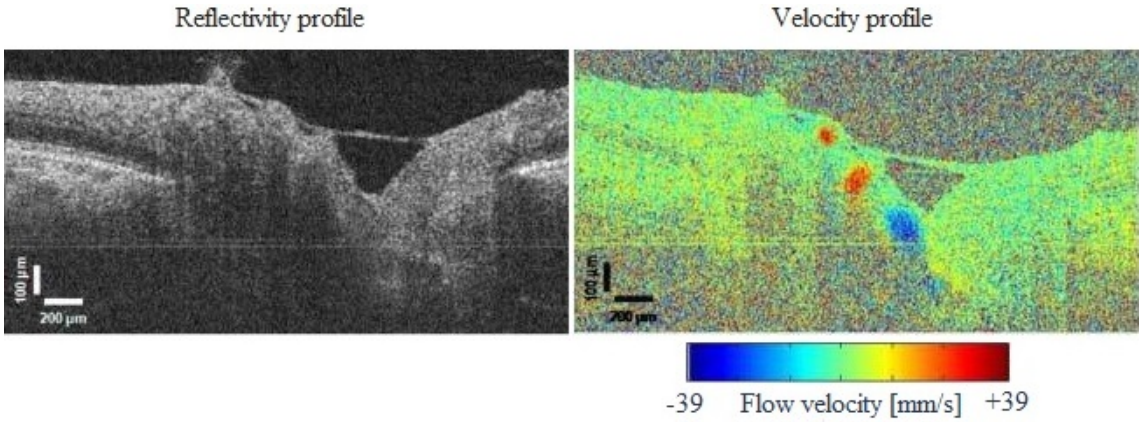

Figure 20. Volumetric Doppler OCT imaging of retinal vasculature. Structural reflectivity B-scan (left) and respective Doppler OCT image with velocity profile (right). Adapted from [25].

1.7 Comparison of OCT approaches

As a final note to this first introductory chapter, it is interesting to compare the different OCT approaches, their imaging speeds and detection sensitivities. In order to better understand the impact of this technique in current applications, a brief comparison with other imaging techniques such as computer tomography (CT), positron emission tomography (PET) or magnetic resonance imaging (MRI) is also important.

Due to the reference mirror movement dependency, the imaging acquisition speed in Time domain OCT is limited by mechanical factors. This constitutes the main disadvantage when compared to Fourier Domain OCT techniques. These use a static reference mirror and each depth profile is read at one, for the Spectral Domain OCT, on in a short time through the swept of the laser over the required range, for the Swept Source OCT. Either way, both present an acquisition rate increase of over one hundred times that of the Time Domain [26]. These acquisition speeds do also reduce artifacts due to sample motion. Moreover, FD-OCT provides higher detection sensitivity [27] over the TD-OCT, and so most of the current OCT work is conducted using Fourier Domain OCT systems.

As mentioned earlier, Fourier Domain OCT comprises two approaches, Spectral Domain and Swept Source. Capable of ultrahigh imaging speeds, deep tissue penetration, Doppler OCT flow analysis, and long imaging range [28], SS-OCT presents advantages over the state-of-the-art SD-OCT technology currently limited to imaging speeds in the range of 20,000 to 50,000 axial scans per second [28]. At deeper imaging distances, SS-OCT has greater sensitivity than SD-OCT, consequence of the source type and its usually higher

central wavelength, but lower signal-to-noise ratios (SNR) [29], consequence of the type and wavelengths of the sources involved in each technique. The downside to applying SS-OCT is due to lack of a compact, high-performance, low-cost swept sources [28], resulting in a more expensive system compared to that of SD-OCT.

Chapter 2

Experimental Setup

This chapter details the experimental Swept Source Optical Coherence Tomography system under development at IBILI (Institute for Biomedical Imaging and Life Sciences, Faculty of Medicine – University of Coimbra) for the imaging of small animals, and used during this master's thesis work.

First, a complete schematic of the system setup along with its working principles is discussed. Then, a description of the system's main components is given, with emphasis on their important characteristics for OCT.

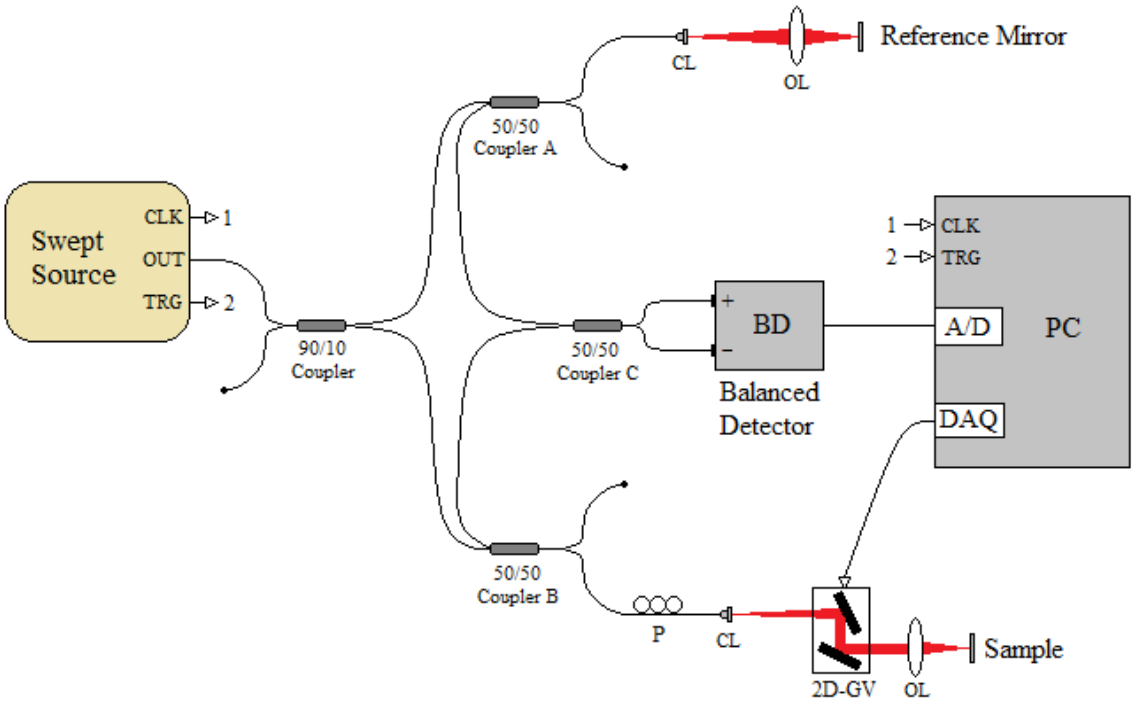

Figure 21. Schematic of the Swept Source OCT system used in this master's thesis. It includes a Swept Source Laser, fiber optic couplers, collimators (CL), two scanning objective lenses (OL), one polarization controller (P), a 2D galvanometer scanning system (2D-GV), a balanced detector (BD), a DAQ board from National Instruments (DAQ), and an acquisition board (A/D).

Figure 21 presents a schematic illustration of the OCT system used. Light emitted by the swept source laser (SSOCT-1060 from Axsun Technologies) is directed to an optical fiber path and split by means of a 90/10 fiber optic coupler into the reference (10%) and sample (90%) arms. In both cases, light is made to pass through the 50/50 fiber optic couplers A and B (Figure 21). These act as circulators, therefore separating light signals travelling in opposite directions inside the respective optical fibers.

Light exiting the optical fiber in the reference arm is collimated and focused by means of an objective lens to a gold coated mirror. The back-reflected light is then re-directed into the optic coupler C.

In the sample arm, after passing through an optical fiber path with a polarization controller, the light is collimated into a bidirectional galvanometer scanning system, before being focused on the sample's imaging spot by the scanning objective lens. Light back-scattered by the sample is then re-directed towards to optic coupler C. Note that the scanning of the sample is achieved through the galvanometer system which is controlled by the DAQ (Data Acquisition) board (PCI-6010 from National Instruments).

Consequently, it is in optic coupler C that light from the reference mirror and back-scattered from the sample interfere. This interference is then detected by a balanced photodetector (Thorlabs PDB471C). An acquisition board (X5-400M from Innovative Integration) carries the sampling and quantization of the interference signal delivered by the balanced photodetector. It is important to note that the light source generates two electrical signals in addition to the optical output: a trigger signal and a clock signal. These are fed to the acquisition board for the trigger and synchronization of the acquisition process. Subsequent processing and display is performed by custom-made software (C++).

2.1 Light source

The swept laser source used is an Axsun Technologies (model SSOCT-1060) High Speed Swept Laser with a central wavelength of 1060 nm. As mentioned in the first chapter, a swept laser source is characterized by the continuous change in wavelength of the outputted light, in time, within the wavelength range. In this model, wavelengths range from 985 to 1095 nm with a sweeping rate of 100 kHz [30]. This process is achieved through a reflective Fabry-Perot MEMS (Microelectromechanical System) tunable filter placed in one end of the laser cavity. The filter produces a tunable reflection peak since its optical axis is tilt with respect to the optical beam.

Table 1. Axsun SSOCT-1060 swept source specifications [30].

Parameter	Value
Wavelength range	985 – 1095 nm
Central wavelength	1040 – 1060 nm
Sweep frequency	100 kHz
Scan range in air	3.7 mm
Maximum samples	1510
Selected number of samples	1376
% Bandwidth used	91 %
Duty Cycle	45 %
Estimated clock frequency	310 MHz *

* ± 20% typical variation

The choice of 1060 nm for central wavelength is worth a brief note. Since the OCT system detects light back-scattered by the retina, light passes twice by the anterior mediums of the eye. It is therefore important to choose a central wavelength that minimizes absorption

and scattering of photons in this round-trip. In the near-infrared region, 600 – 1500 nm, water is the main absorbing element. The absorption coefficient of water as a function of wavelength is plotted in Figure 22. Light scattering, namely Rayleigh scattering, presents a cross-section that varies inversely with $\lambda_0{}^4$.

For axial resolutions in the range 1 to 4 μm, the 800 nm central wavelength is typically used. However, this wavelength yields an unwanted high scattering cross-section in comparison to longer wavelengths. On the other hand, the choice of the 1300 nm presents lower scattering cross-section at the cost of a lower axial resolution. The choice of wavelength is therefore a balance between scattering and depth resolution, with the 1060 nm allowing for a resolution in the range of 4 to 10 μm, while presenting an acceptable water absorption for the aimed application.

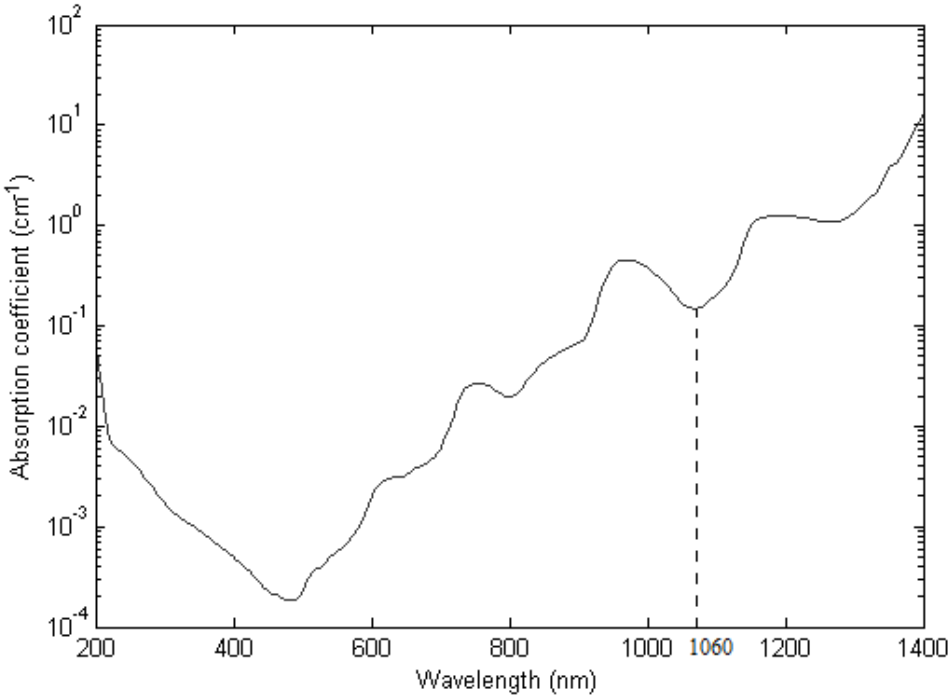

Figure 22. Water absorption coefficient (1/cm) as a function of wavelength (nm). From [31].

Figure 23 represents the average spectral power output of the swept source laser, along the wavelength sweep, ranging from 985 nm to 1095 nm. During this 110 nm sweep, the source's output trigger signal, with a period of 10 μs, is used for synchronization of the acquisition process with the beginning of the wavelength sweep, delayed by 90 ns in order to compensate the difference in time between the clock and trigger signals.

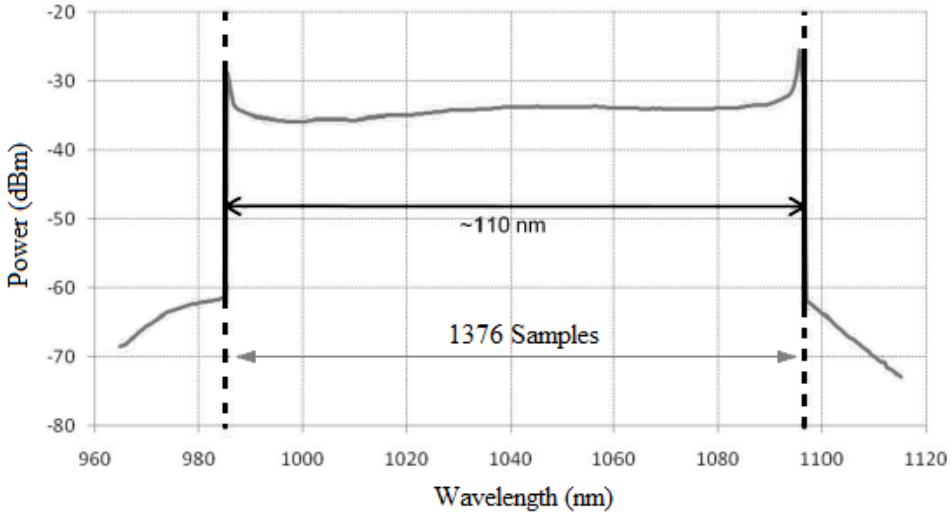

Figure 23. Time average spectral power output of SSOCT-1060 swept source. Adapted from [30].

This sweeping process is characterized by having two distinct stages – ascending and descending – as represented in Figure 24 (bottom). During the ascending phase the laser is turned ON and the wavelength sweep takes place (45% duty cycle, yielding a 4.5 μs duration). In this stage, the acquisition is controlled by an optical clock signal (see Figure 25), at a frequency of 310 MHz, with time varying frequencies in order to obtain a linear acquisition in the k-space (wavelength space, frequency domain), allowing for the acquisition of 1376 samples of the interference signal. During the descending phase, the laser is turned OFF, the clock signal is a "dummy" clock – used to fill the gap that lasts until the end of the sweeping process – and the tunable filter returns to its original position.

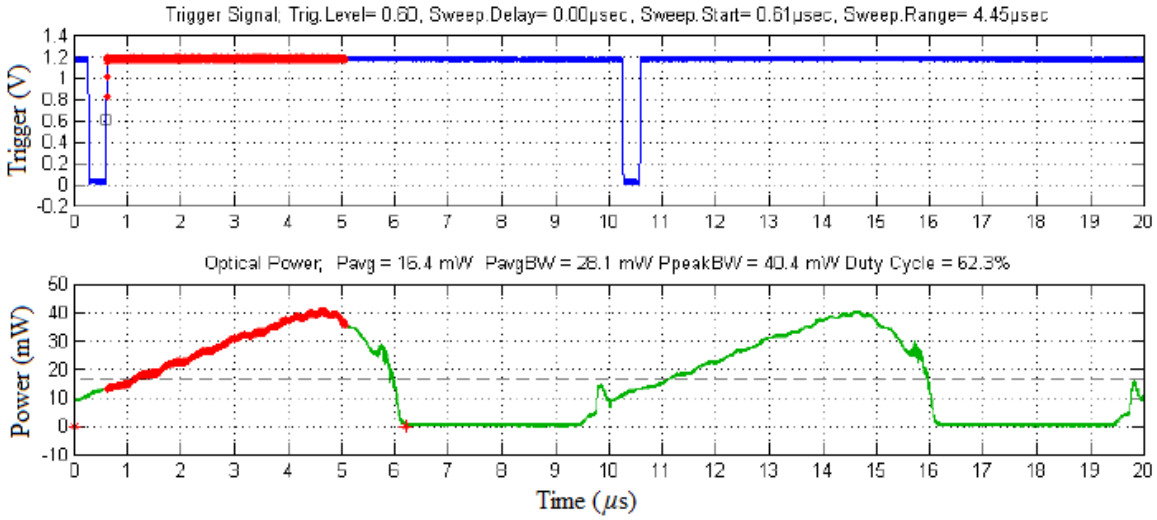

Figure 24. Trigger signal (top) and spectral power of the SSOCT-1060 engine. From [30].

Since the entire wavelength sweep is done at a frequency of 100 kHz and each sweep generates one A-scan, this source is capable of generating 100 000 A-scans per second.

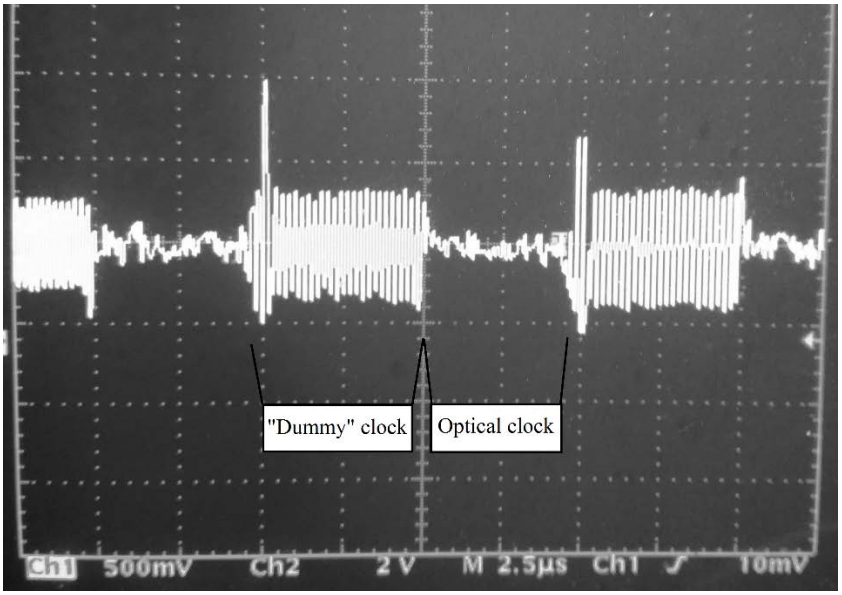

Figure 25. Swept source's clock signal observed in the oscilloscope. During the "optical clock" (~4.5 μs) the interference signal is acquired. During the "dummy clock" (~5.5 μs) there is no acquisition.

2.2 Balanced detector

The interference signal of the OCT system is detected using a balanced photodetector PDB471C from Thorlabs. As mentioned in the beginning of this chapter, the interference signal between the sample and reference signals takes place in optic coupler C. The two outputs of this coupler are connected to the inputs of the balanced photodetector. It consists of two well-matched pigtailed InGaAs photodiodes followed by an ultra-low noise and high-speed trans-impedance amplifier. The latter is responsible for the generation of the output voltage which is proportional to the difference between the photocurrents generated by each of the photodiodes and, as such, proportional to the difference between the optical inputs – see the block diagram of Figure 26. This proportionality relation can be described by [32]:

$$U_{RF\ OUTPUT} = \left(P_{opt\,1} - P_{opt\,2}\right) \times G \times R(\lambda) \tag{35}$$

where $P_{opt\,1}$ and $P_{opt\,2}$ represent the optical power of each input, $G = 10^4\ (V/A)$ is the trans-impedance gain and $R(\lambda)$ is the responsivity of the photodiode at a given wavelength. The responsivity values can be found from the plot in Figure 27 (~0.72 A/W for the 1060 nm wavelength).

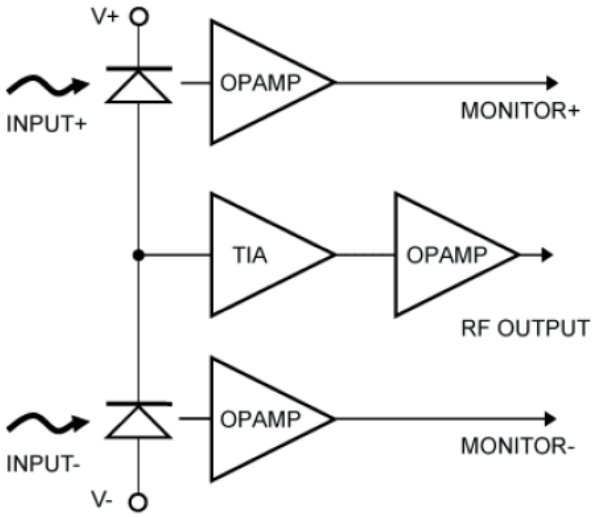

Figure 26. Block diagram of the PDB471C balanced amplified photodetector. From [32].

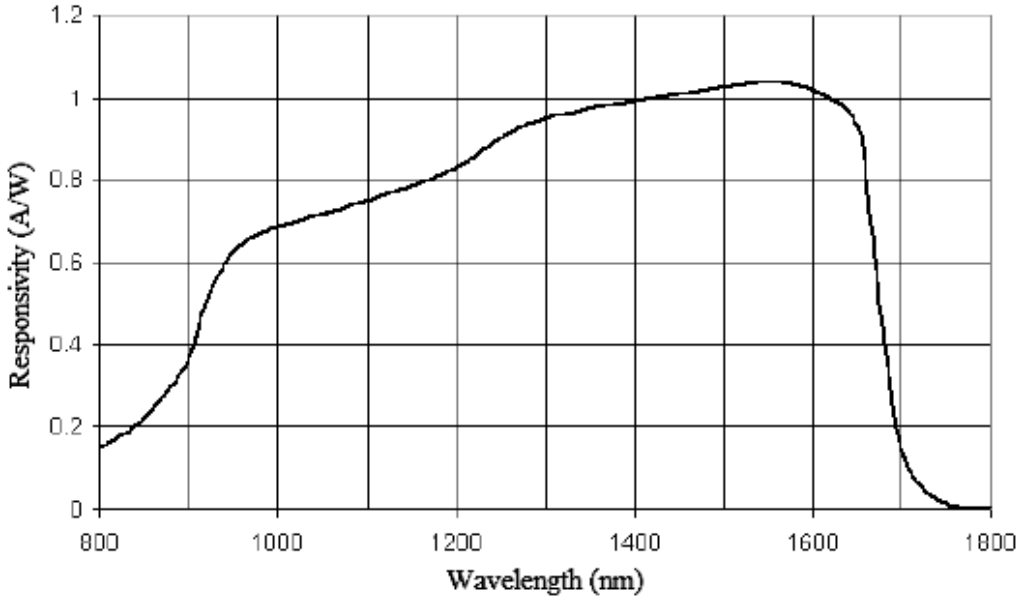

Figure 27. PDB471C responsivity curve. From [32].

The balanced photodetector used has a wavelength range from 900 nm to 1400 nm, being optimized for input light of 1060 nm wavelength. Additional important characteristics include the 3 dB bandwidth of 400 MHz, and the Common-Mode Rejection Ratio (CMRR) over 25 dB (typically $> 30\ dB$) [31] for the entire bandwidth (Figure 28).

In a differential detection device, the Common-Mode Rejection Ratio represents the ratio between the power of the differential gain over the common mode gain. It characterizes the ability of the device to eliminate common-mode signals.

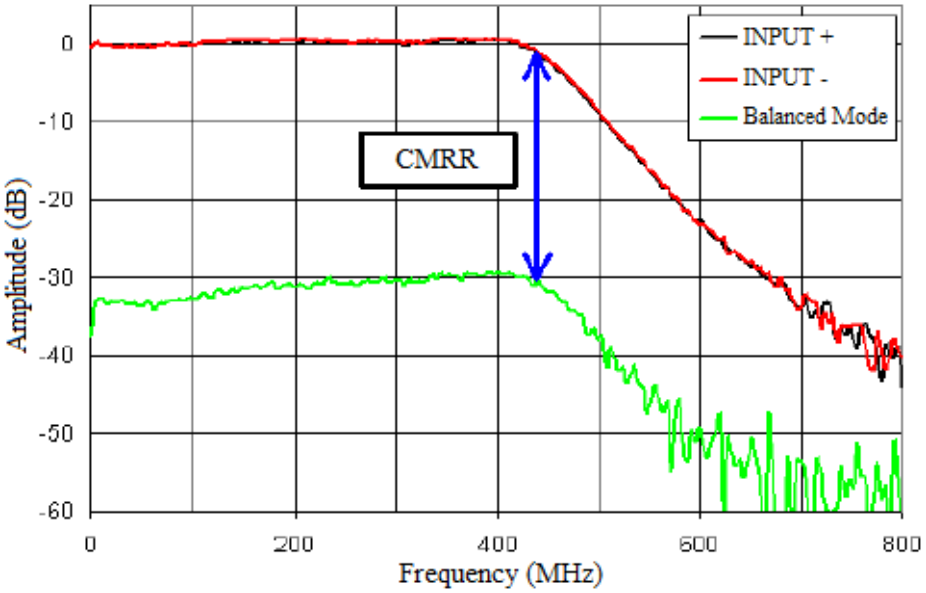

Figure 28. PDB471C frequency response. From [32].

Although an infinite value for the CMRR is desired, in practice one aims for high enough CMRR in order to amplify the differential part of the signal and reject the majority of the common-mode components.

Additionally, a balanced detection scheme allows for the reduction of excess photon noise [33] and consequently leads to the signal-to-noise ratio (SNR) increase.

From Figure 27, it possible to verify that the CMRR of the PDB471C photodetector for frequencies in the range between 0 and 400 MHz is higher than 30 dB.

2.3 Acquisition hardware

The acquisition board XMC Module X5-400M from Innovative Integration is used to convert the analog interference signal into a digital one. The board has two channels of 14-bit A/D (analogue to digital conversion) capable to operate at rates up to 400 MSPS (mega samples per second) [34]. This board allows the use of external trigger and clock signals which, in the current setup, are fed with the signal provided by the laser source.

The board includes, for signal processing, data buffering and system IO, a high performance computing core built around a Virtex-5 Field Programmable Gate Array supported by a 512 MB DDR2 DRAM and a 4 MB QDR-II SRAM. For communication with the computer, an 8-lane PCI Express interface provides over 1 GB/s transfer rates [34].

The data packaging can be done by either frame acquisition or continuous acquisition [34]. In the frame acquisition, used in the experimental setup, each frame contains a number of data points multiple of 256, to a maximum of 2048 data points. Usually, each frame formed by 768 32-bit words, each divided into two 16-bit words containing one data point each. Thus, a single frame contains 1536 data points. The first 1376 data points describe the desired A-scan (per source's limitation) and the remaining 160 data points are zero-padded values.

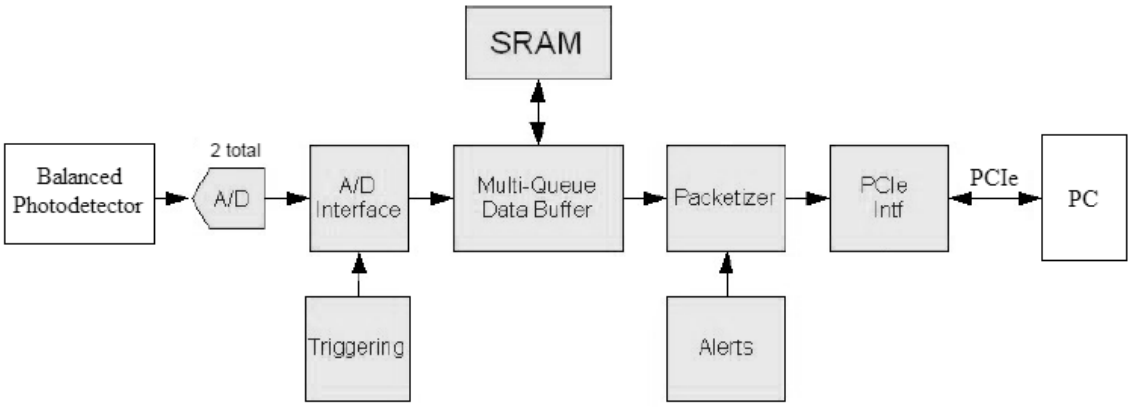

Figure 29. X5-400M Framework Logic Data Flow. Adapted from [34].

The diagram in Figure 29 describes the data acquisition process pipeline. Data flows from the analog to digital conversion devices into the FPGA's A/D interface component, with the control of the source's trigger signal. Data is directed into the data buffer in order to be queued in the SRAM. From that point on, the "packetizer" pulls the data from the queue, creates data packets of 32-bit words and sends those to the PC memory making them accessible to running programs [34].

2.4 Acquisition and processing software

After the data packets acquired by the X5-400M board arrive at the host PC, a series of processes and data transfers in and between these two components take place in order to obtain the Fourier transformed data of the acquired interference spectra. It is important to note that in the OCT's current processing setup, the Fast Fourier Transform algorithm is done by a function provided by Innovative Integration's development tool, meaning that this processing step is handled by the acquisition board X5-400M.

While both galvanometer mirrors move by a ramp wave, the number of A-scans that form the requested B-scan are acquired. Upon finishing its acquisition, all these A-scans that form the B-scan are sent simultaneously to the PC memory and it is then initiated the processing of the data packets, as described in Figure 31. One A-scan (data packet) is usually formed by 768 32-bit words, which in turn are divided into 16 most and 16 least significant bits, each containing information of one data point from the interference spectrum (Figure 30). The data point's information needs to be reorganized since the acquisition is done using only one of the board's two available A/D channels, meaning that instead of having the 16 most significant bits reserved to channel 1 and the 16 least to channel 2, the same number of bits is used to pass the single channel's information as represented in Figure 30. Thus, each data packet contains information of 1536 data points of the interference spectrum. But as mentioned before, the source's wavelength sweep only allows the acquisition of 1376 samples in each A-scan, meaning that only the first 1376 data points of the data packet contain relevant information. So, after this reorganization, the last 160 data points are forced to zero (zero padding). Then, and since to display the A-scan's FFT signal an inverse Fourier transform of each data point is needed, the addition of an imaginary part (with value equal to zero) must be done, so that each data point contains both real and imaginary parts. In the end of this three step process each A-scan has 3072 samples.

32-bit word (0)		32-bit word (1)		…	32-bit word (767)	
Data point 1	Data point 0	Data point 3	Data point 2	…	Data point 1535	Data point 1534

Figure 30. Data packet (A-scan) format, with 768 32-bit words, each divided into two 16-bit words.

After this data pre-processing, the B-scan (set of N A-scans) is sent to the acquisition board's memory in order to perform the Fourier transform using the board's Transform() method. At last, the FFT of each A-scan is then sent to the host PC's memory for further display. Note that each resulting A-scan's FFT signal only has 768 points, due to the rejection of the imaginary part (half of the original 3072 samples) and the rejection of the mirrored points (half of the remaining 1536 samples), since every FFT signal is symmetric.

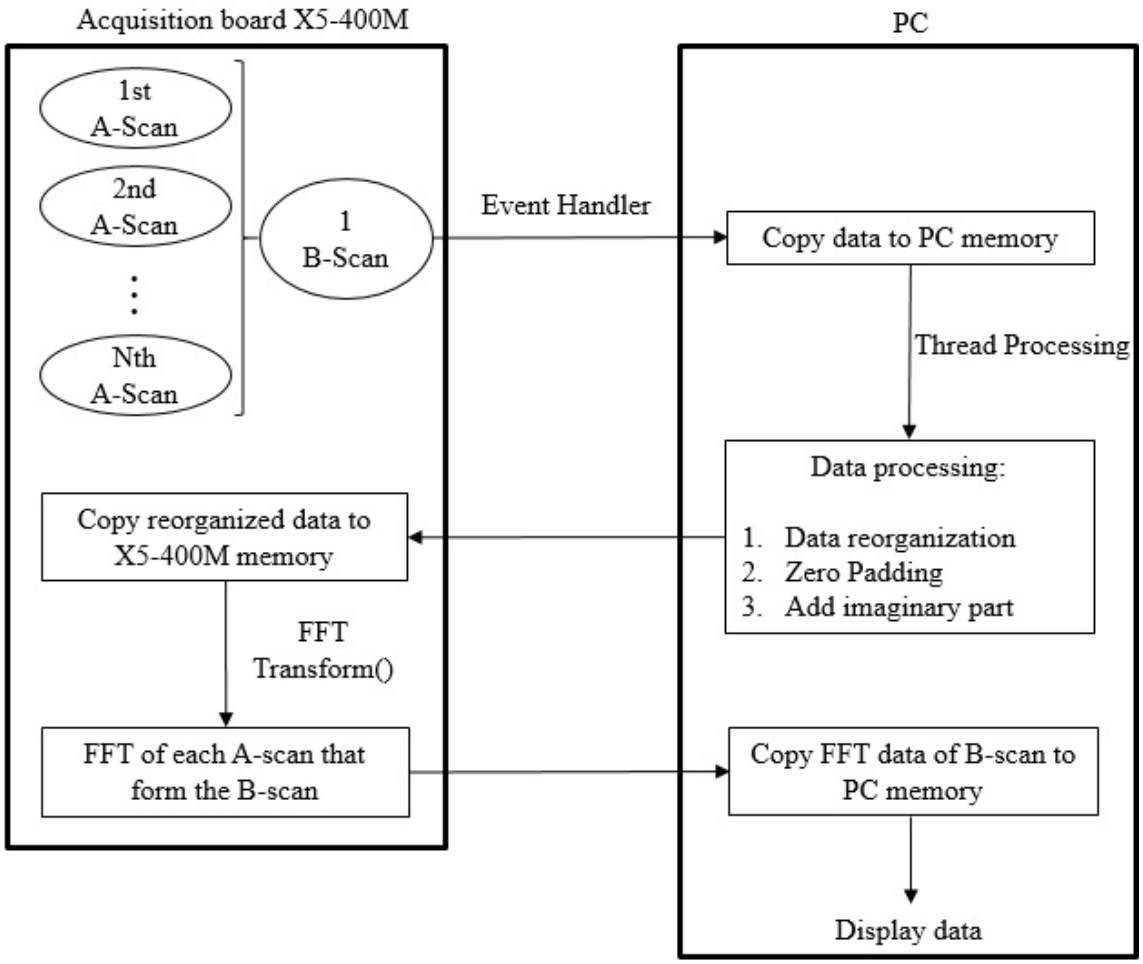

Figure 31. Flow chart of B-scan data since its acquisition until the FFT is obtained.

Note that all these processes are required for obtaining (and further displaying) the Fourier transform of the A-scans from a given B-scan. For only displaying an interference spectrum, only data reorganization and zero padding are needed, and then the resulting data is shown as a graph in the user interface.

2.5 Galvanometer system

The use of a galvanometer system GVS002 from Thorlabs allows scanning the sample by directing the laser beam across the region of interest.

The system is made of two silver coated mirrors– an X-mirror and a Y-mirror – with around 97% reflectance for wavelengths between 970 nm and 1100 nm, each independently controlled by a precision motor through an electronic servo driver. An optical position detector provides information about each galvanometer position. The

motor's acceleration is directly proportional to the current applied to the motor coil, yielding a rotation of the motor shaft and, consequently, the rotation of the mirror [35].

Because of the maximum range of input voltage of the servo driver is ±10 V and of the three possible scaling factors, 0.5 V, 0.8 V and 1 V per degree, the respective scanning angles are of ±20°, ±12.5° and ±10° with an angular resolution of 0.0008° [35].

The signals driving the galvanometers mirrors are generated by the NI-DAQ board according to user's specifications via the acquisition software and allow the specification of the scanning angle and number of A-scans.

2.6 Objective lenses

Two different scanning objective lenses from Thorlabs are used. The LSM02-BB model is placed in the reference arm to focus the beam in the reference mirror. On the other hand, the LSM03-BB model is positioned just before the sample to focus the beam in the sample at study.

Since both these models are telecentric objectives, they present interesting characteristics for OCT imaging. First, as the laser beam is scanned across the sample, a constant field of view is achieved. This results in smaller image distortion and consequently better image quality. Moreover, magnification does not change with depth, minimizing the post-processing corrections needed for displaying images with correct geometry. Second, a higher coupling of the light back-scattered from the sample into the detection system is also achieved. Finally, because the spot size in the image plane across the entire field-of-view is approximately constant, so is the image resolution [36].

Table 2 presents the specifications for the objectives in use.

The working distance (see Figure 32) is the distance between the tip of the scanning lens and its front focal plane. The objective lens field-of-view is the size of the area on the sample that can be imagined within the targeted resolution [36].

Table 2. LSM02-BB and LSM03-BB specifications. From [36].

	LSM02-BB	LSM03-BB
Magnification	10X	5X
Wavelength Range	1050 ± 50 nm	
Effective Focal Length	18 mm	36 mm
Lens Working Distance	7.5 mm	25.1 mm
Scanning Distance	16.1 mm	18.9 mm
Pupil Size	4 mm	
Field of View	4.7 x 4.7 mm	9.4 x 9.4 mm
Mean Spot Size	11 μm	21 μm

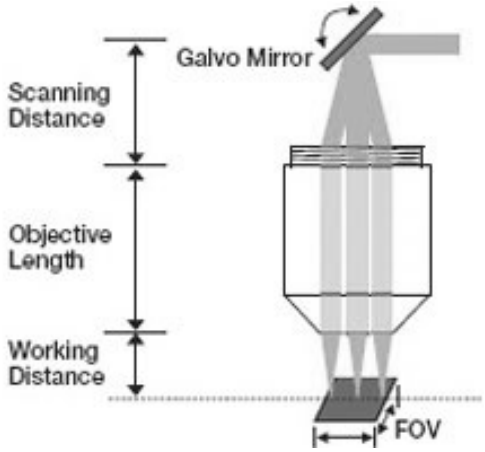

Figure 32. Representation of objective lens. Adapted from [36].

Chapter 3

Phase Stability in Phase-Sensitive OCT

The analysis of the phase of the OCT signal allows, among other applications, to determine the information on the blood flow within the sample. However, in order to retrieve reliable information on the phase, phase stability is paramount.

First, an approach to Phase-Sensitive OCT is given, before introducing the topic of phase stability along with its determination for the OCT system being developed. Lastly, the implementation of a fully numerical phase stabilization algorithm, for improving the phase stability of the system, is described.

3.1 Phase-sensitive OCT

The most common application of Fourier Domain Optical Coherence Tomography systems is to extract information on sample reflectivity. However, it is also possible to obtain additional information on the sample's properties through the phase analysis of gathered spectrograms. Phase-sensitive OCT, also known as phase-resolved OCT, measures both phase and amplitude of the OCT signal along the A-scan. The field of application and general interest have grown over the last decade in the field of Optical Coherence Tomography.

Since in Fourier Domain OCT the signal analysis is done by Fourier transforming the acquired spectrogram, the yielded result is a complex-valued depth profile with both amplitude (standard intensity profile) and phase (phase-contrast profile) information. The most used application for phase-resolved OCT is Doppler flow OCT, where, through analysis of the phase-shifts between successive A-scans, it is possible to identify blood flow in acquired images [37] [38]. These phase-shifts, originated by the Doppler effect on the laser beam, can be obtained by evaluation of phase differences [39] or phase variances [40] between consecutive spectrograms.

Stability of the phase is of highest importance in order to retrieve reliable phase information from the acquired data [41]. This implies that the sampled wavenumbers must remain equal during the entire acquisition process [37].

In swept source OCT, phase instability can be caused by jitter in synchronization between the source's wavelength sweep and the process of data acquisition [41] [42]. This jitter is a random time delay between the trigger signal and the actual beginning of the sampling by the acquisition board. This uncertainty in time leads to differences in the wavenumber space from one cycle to the next [43]. The smallest time delays do have a noticeable impact in the acquired spectrograms at current sweeping and sampling rates. Moreover, mechanical swept sources present poorer phase stability compared to sources without moving parts, like semiconductor based ones. This is mainly due the mechanical movement dependence on accumulation and depletion of momentum, which can result in hysteresis and unwanted drifts (e.g. thermal drift caused by friction) in the operating regime, but can also be influenced by mechanical instabilities like vibrations [44]. Phase instability in the OCT system reduces the accuracy of phase measurements and manifests itself as depth dependent phase differences [43].

3.2 Phase stability assessment

Phase stability of an OCT system can be estimated by the statistical analysis of phase differences between consecutive A-scans [38] [40] and is usually defined as the standard deviation of these differences [40] [44]. In order to assess the phase stability of the OCT system being developed, data analysis was performed based on the algorithm described in the paper "Akinetic all-semiconductor programmable swept-source at 1550 nm and 1310 nm with centimeters coherence length", by Bonesi *et al.* [44].

3.2.1 Algorithm

The implemented algorithm (in MATLAB), named "cross-correlation algorithm" in the paper, intends to estimate the OCT system phase stability. Two thousand consecutive spectrograms (Figure 33) of the same location (i.e., no galvanometer scanning) on a 1 mm thick cover glass were acquired and processed according to the steps presented in Figure 34. This assessment was done both with and without a Butterworth electronic low-pass filter (CLPFL-0100 from Crystek) with a frequency cutoff of 100 MHz, placed between the balanced detector and the acquisition board. This intended to analyze its effect in phase measurements since these suffer degradation in deeper regions of the sample, due to the higher frequencies of the interference fringe [45].

For each acquired spectrogram (S_i) a sequence of processing steps (Figure 34) were applied. First, Fourier Transform using the Fast Fourier Transform algorithm *fft()* was performed to the spectrogram in order to extract the phase information – *angle()* and *unwrap()* functions – at the A-scan peak position coincident with the front surface of the cover glass (Figure 35). This position corresponds to the maximum absolute value of the obtained A-scan ($F_{S_i} = \mathcal{F}\{S_i\}$). Then, for this position, phase differences between consecutive A-scans were obtained ($\varphi_{D,i} = \varphi_{i+1} - \varphi_i$) using the *diff()* function and its standard deviation $\sigma_{\varphi_{D,i}}$ computed with the *std()* function. The $\sigma_{\varphi_{D,i}}$ value represents the phase stability of the OCT system.

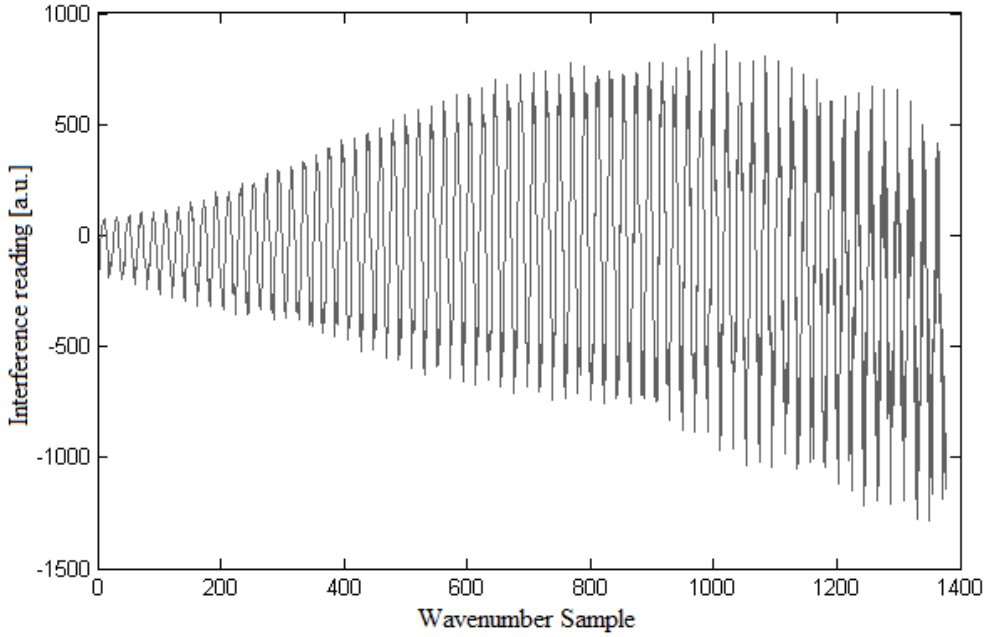

Figure 33. One of the 2000 total acquired spectrograms of a 1 mm thick cover glass.

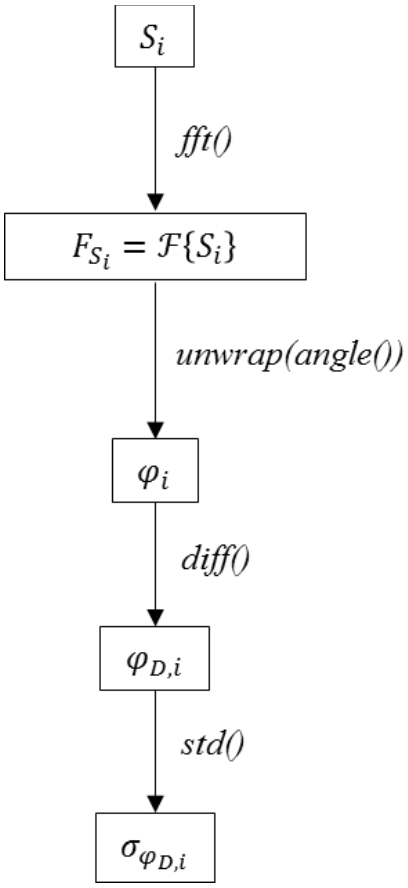

Figure 34. Schematic of the algorithm implemented in MATLAB, for evaluating the system's phase stability. S_i represents the i-th spectrum (raw data); $\mathcal{F}\{\ \}$ is the FFT function operator; φ_i is the unwrapped phase and σ_{φ_i} its standard deviation; $\varphi_{D,i}$ is the phase difference between consecutive spectra and $\sigma_{\varphi_{D,i}}$ its standard deviation. The MATLAB functions used in each step are presented next to the arrows.

A brief note regarding the intensity profile in Figure 35. The interfaces air/glass and glass/air are easily identified by the two peaks of the resulting A-scan. The first peak (from left to right) corresponds to the front surface of the cover glass (air/glass interface) while the second corresponds to the back surface of the cover glass (glass/air interface).

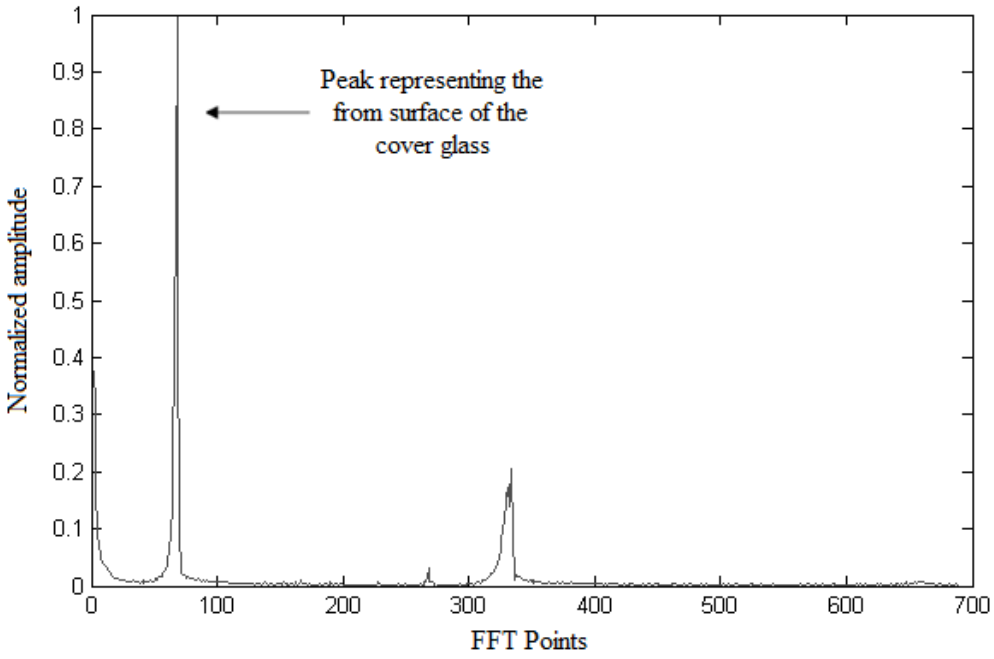

Figure 35. Normalized A-scan of 1 mm thick cover glass, processed by Fourier transform of a spectrogram, used in the phase stability algorithm.

The standard deviation of the phase, σ_{φ_i}, was also easily obtained by applying the *std()* function to the φ_i values. Ideally it should be the same since no changes in sample properties were introduced. However, this is not the case due to variations arising from swept-source instabilities, as discussed below.

3.2.2 Results and conclusions

The results obtained from the implementation of the previous algorithm are presented in Table 3. The computed values of power spectrum FFT phase stability represent the phase stability of our OCT system. As aforementioned, they are determined at the A-scan peak position corresponding to the front surface of the cover glass.

Table 3. Phase stability algorithm results evaluated at the front peak position, obtained from analysis of a 1mm thick cover glass. The low-pass filter used was Crystek CLPFL-0100, with a 100 MHz cutoff frequency. σ_{φ_i} is the standard deviation of phase and $\sigma_{\varphi_{D,i}}$ represents the standard deviation of phase difference.

Parameter	**Value**	
	Without low-pass filter	With low-pass filter
σ_{φ_i} (rad)	0.638	0.253
$\sigma_{\varphi_{D,i}}$ (rad)	0.069	0.058

We can compare the values obtained for our OCT system with those reported by Bonesi *et al.* [44]. However, it is important to note that the OCT setup described in that paper uses an akinetic all-semiconductor swept-source that is characterized by the absence of moving parts for performing the laser frequency sweep. Our system's source is based in a MEMS tunable filter. Therefore, the phase stability values measured will be poorer than those presented in the paper.

The values presented in the paper for the cross-correlation, standard deviation of phase σ_{φ_i} = 67.5 mrad and standard deviation of phase difference $\sigma_{\varphi_{D,i}}$ = 4.5 mrad, for a 100 kHz sweep rate, are much lower than the ones obtained for our setup, portraying a better phase stability of their system compared to ours. Also, the electronic low-pass filter attenuates the higher frequencies of the signal resulting in better phase stability without compromising the sensitivity roll-off of the system as shown in Chapter 5.

A reported phase stability value of 9 mrad [46], by R. Manapuram, using a mechanical swept source (rotating polygonal mirror) for *in vivo* phase-sensitive measurements like detection of microbubbles in mice tails or mechanical wave propagation in mice corneas, both *in vivo*, can be regarded as the target value for phase stability. Since the current state of the OCT system being developed in IBILI presents a phase stability of 58 mrad, a fully numerical phase stabilization method was implemented. In the next section, a description of this algorithm is made, along with the obtained improvement in the results.

3.3 Numerical phase stabilization

Here, a fully numerical phase stabilization algorithm for improving the phase stability of the swept-source OCT system is presented. The algorithm is based on the work published

by Y.-J. Hong *et al* in [47] and was tested in the data sets acquired for the phase stability measurement, to assess the improvement in the results.

The algorithm corrects the phase jitter caused by relative shifts between two sampled spectrograms $S_1(k)$ and $S_n(k)$, where k is the sampling index of the spectrum (linear in wavenumber) and n is the index of the n^{th} spectrogram of a B-scan or Volume.

The $S_1(k)$ spectrum is considered the reference spectrum (typically, the first of m within the ensemble). Assuming that $S_n(k)$ suffers from spectral shift, it can be viewed as:

$$S_n'(k) = S_n(k) \otimes \delta(k - \beta) \tag{36}$$

where β is the spectral shift in the sampling points and $\otimes$ is the convolution operator. Applying the shift theorem of the Fourier transform to $S_n'(k)$, yields the Fourier transformed signal:

$$F_n'(j) = F_n(j)\, e^{-i\frac{2\pi j\beta}{N}} \tag{37}$$

where $F_n'(j)$ and $F_n(j)$ are the discrete Fourier transform of $S_n'(k)$ and $S_n(k)$, respectively, j is the index of the discrete Fourier transform (that also represents the depth position in the A-scan) and N is the number of sampling points in a single spectrum. The term $e^{-i\frac{2\pi j\beta}{N}}$ is the erroneous phase slope that must be corrected. To do so, the value of β must be determined. Weighted-least square fitting determines the β value that minimizes E^2 given by:

$$E^2 \equiv \sum_j I(j)\left[-\frac{2\pi j\beta}{N} - \varphi(j)\right]^2 \tag{38}$$

where $\varphi(j)$ represents the differential phase between $F_n'(j)$ and $F_1(j)$, caused by spectral shift, obtained through the following operation:

$$\varphi(j) = \angle F_n'(j)F_1^*(j) = \angle I(j)\, e^{-i\frac{2\pi j\beta}{N}} \tag{39}$$

where $\angle$ represents the phase operator, $F_1^*(j)$ is the complex conjugate of the reference A-scan and $I(j)$ is the intensity of the perfectly correlated part of the OCT signal. $I(j)$ is set equal to zero if below the noise level.

The algorithm is applied to each acquired spectrogram $S_n'(k)$, apart from the reference spectrogram and according to the processing steps presented in Figure 36.

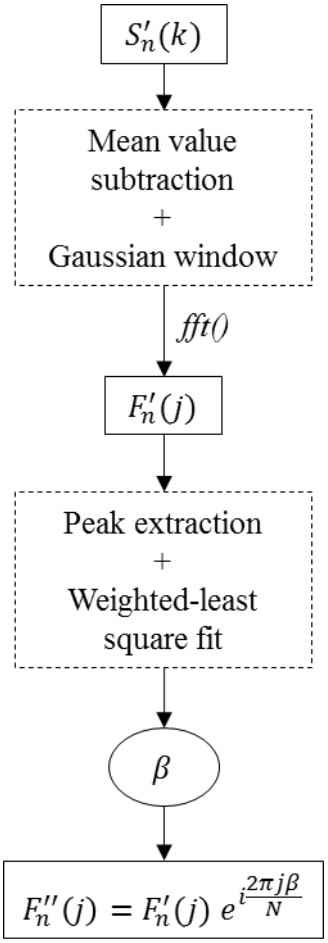

Figure 36. Schematic of the phase stabilization algorithm implemented in MATLAB. See text for description.

First, the average power of the signal is removed by subtracting the mean value of each spectrogram. Then, a Gaussian window is applied to each signal, with a standard deviation $\sigma = 0.2N$, before computing its Fourier transform using the Fast Fourier Transform algorithm of MATLAB, obtaining $F'_n(j)$. From the resulting Fourier transformed signal, a region of ± 30 FFT points around the first peak of the A-scan is selected, corresponding to the correlated part between the A-scan under correction ($F'_n(j)$, $n = 2, \dots, m$) and the reference A-scan ($F_1(j)$). For our analysis, this peak matches the first surface of the cover glass used in the phase stability assessment. Then, with the 60 points of each signal, the β value is determined for each pair $F_1(j)/F'_n(j)$, as described before. After determining β through Equation 38, the spectral shift is cancelled by multiplying the entire A-scan under correction by the complex conjugate of the phase slope ($e^{i\frac{2\pi j\beta}{N}}$), obtaining the corrected A-scan $F''_n(j)$:

$$F''_n(j) = F'_n(j)\, e^{i\frac{2\pi j\beta}{N}} \tag{40}$$

Table 4 presents the yielded results after applying the numerical phase stabilization algorithm to the data sets used in section 3.2.

Table 4. Improvement in the phase stability results evaluated at the front peak position of a 1mm thick cover glass. The low-pass filter used was Crystek CLPFL-0100, with a 100 MHz cutoff frequency. σ_{φ_i} is the standard deviation of phase and $\sigma_{\varphi_{D,i}}$ represents the standard deviation of phase difference.

Parameter	**Value**			
	Without low-pass filter		With low-pass filter	
	Before correction	After correction	Before correction	After correction
σ_{φ_i} (rad)	0.638	0.0136	0.253	0.0201
$\sigma_{\varphi_{D,i}}$ (rad)	0.069	0.0140	0.058	0.0119

These results show a great improvement in the phase stability of the OCT system, from 58 mrad to 11.9 mrad, which can be considered a good value for phase sensitive applications since it is fairly close to the desired 9 mrad reported by R. Manapuram [46]. Therefore, it can be concluded that this phase stabilization method yields the expected upgrade in the phase stability through a fully numerical compensation that can be easily implemented without any additional hardware.

Regarding the performance of this algorithm, the computing times involved are still substantial, taking 1.89 seconds to process a B-scan composed of 512 A-scans. Therefore, improvements are needed for the algorithm to become fast enough for the demanding acquisition speeds of state-of-the-art OCT systems.

Chapter 4

Optical Simulations

The current chapter presents the optical simulations developed using software Zemax OpticStudio 15 Standard Edition, concerning the imaging of the rat's eye in the sample arm of the OCT system.

First, a description of an optical model of the rat's eye is presented, along with its simulation in Zemax. Then, an optical setup for imaging the rat's retinal structures is tested, detailing its optical performance.

4.1 Rat's eye optical model

As mentioned in this thesis, the Optical Coherence Tomography system being developed at IBILI intends to image retinas of small animals, particularly rats. Therefore, a study of the optical components needed to obtain a good image of the rat's retinal structures was made using Zemax OpticStudio 15, a widespread and very powerful Computer-Aided Design (CAD) tool for design and analysis of optical systems. Before studying any optical solutions, an optical model representing the refractive properties of the eye must be implemented in Zemax. Following the initial works of A. Hughes in 1979 [48] and based on the most recent work conducted by D. Link *et. al.* in [49], an optical model of the rat's eye, formed only by simple lenses was developed, according to the parameters presented in the following Table 5.

Table 5. Rat's eye data for Zemax model – d represents the distance measured from the anterior corneal surface, r represents the curvature radius and n is the refractive index of each layer in-between surfaces. [48] [49]

Surface	$\boldsymbol{d}$ $(\boldsymbol{mm})$	$\boldsymbol{r}$ $(\boldsymbol{mm})$	$\boldsymbol{n}$
Anterior cornea	0	2.965	1.38
Posterior cornea	0.260	2.705	1.337
Pupil	---	---	1.337
Anterior lens	0.881	2.340	1.39
Anterior core	1.778	0.958	1.5
Posterior core	3.695	-0.958	1.39
Posterior lens	4.591	-2.340	1.337
Retinal surface	5.981	-2.965	1.351
Outer limiting membrane	6.111	-2.965	

For designing the rat's eye in Zemax, each single lens corresponding to each ocular structure must be defined by three parameters – thickness (d), curvature radius (r) and refractive index (n) of the medium between that surface and the next. The resulting layout of the optical system is presented in Figure 37. Note that the distances (in mm) presented in Table 1 are referred to the first optical component of the rat's eye, i.e. the anterior cornea, as detailed in Figure 37. Also, the pupil located between the posterior cornea and

the anterior lens may vary in size (aperture), similarly to the pupil in the human eye. For this simulations, a pupil diameter of 3 mm was used, based on the values described by P. Artal *et al.* in [50], for a fully dilated pupil, since these are the intended imaging conditions.

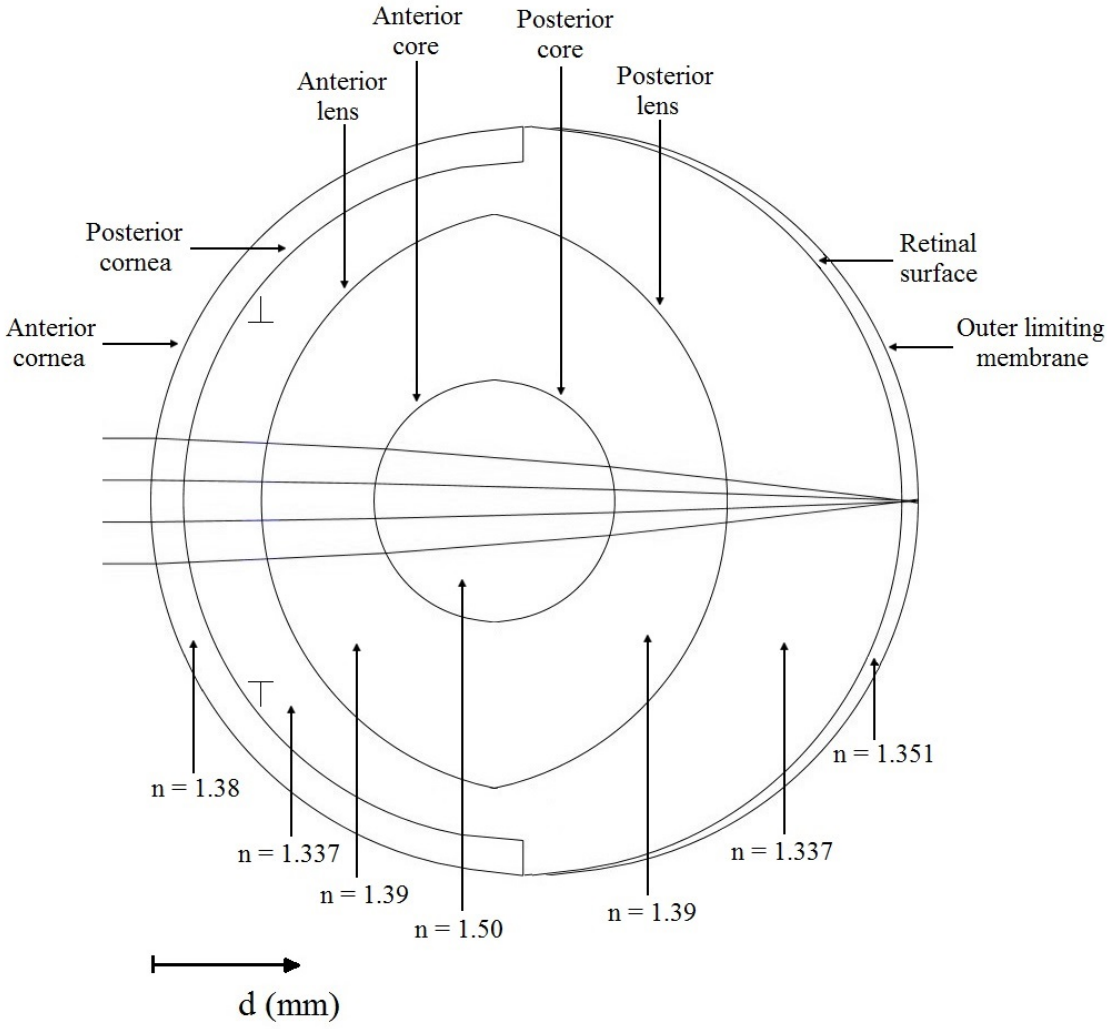

Figure 37. Rat's eye optical model implemented in Zemax, with reference to each optical surface and refractive index, apart from the pupil, that is not drawn in the schematic. Paraxial rays entering through the anterior corneal surface and focusing in the outer limiting membrane (inside the retina). Distances (d) presented in Table 5.

The biggest concern when imaging the rat's eye is the inherent presence of a high spherical aberration due to its anatomy, namely its high 300 diopter ($D = \frac{1}{f}$, where f is the focal length) value of refractive power [48] [49]. Spherical aberration, present in spherical lenses, occurs when incident paraxial rays at different distances from the optical axis fail to converge in the same focal point. This effect is accentuated for paraxial rays further from the optical axis, meaning that thinner laser beams will suffer less spherical

aberration. The ray trace in Figure 38 represents the spherical aberration in the eye, for a collimated beam with an aperture diameter of 2.5 mm, the limit situation in which all the marginal rays pass through the pupil of the eye. It is possible to see that the marginal rays focus (i.e., cross the optical axis) before reaching the retinal surface. In the next section, this effect is quantified when analyzing the proposed optical solution.

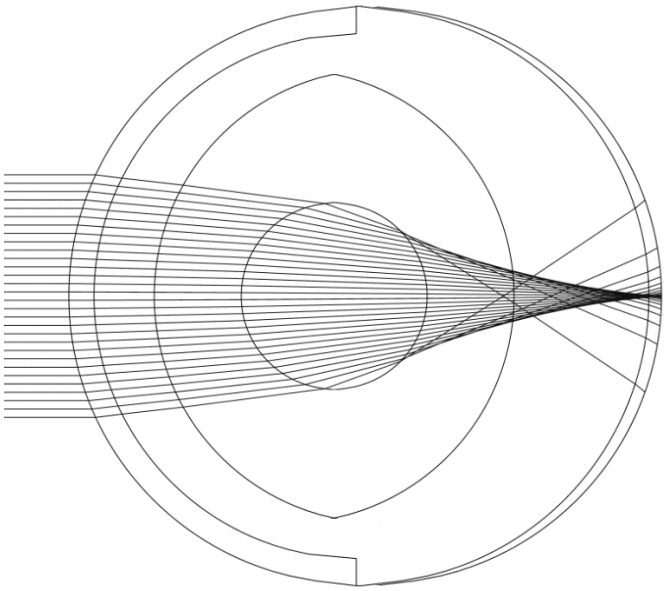

Figure 38. Rat's eye optical model represented in Zemax, for describing the spherical aberration when using a wide collimated beam of 2.5 mm aperture diameter.

4.2 Imaging probe simulation

Although many implementations for imaging retinal structures of the rat's eye in Optical Coherence Tomography are based on the use of an objective lens, other solutions are also implemented. It is possible, for instance, to obtain image using only a pair of lenses forming an imaging probe [51] or using a microscope objective [52] [53].

Here, a pair of lenses (imaging probe) containing one achromatic doublet and one aspheric lens is presented. Figure 39 schematically represents the layout of the simulation performed in Zemax.

The first lens of the pair, L_1, is a 25 mm diameter achromatic doublet (model AC254-060-C) from Thorlabs, with a focal distance of 60 mm [54]. The second lens, L_2, is an aspheric lens (model AL2520M) also from Thorlabs, with a focal distance of 20 mm [55].

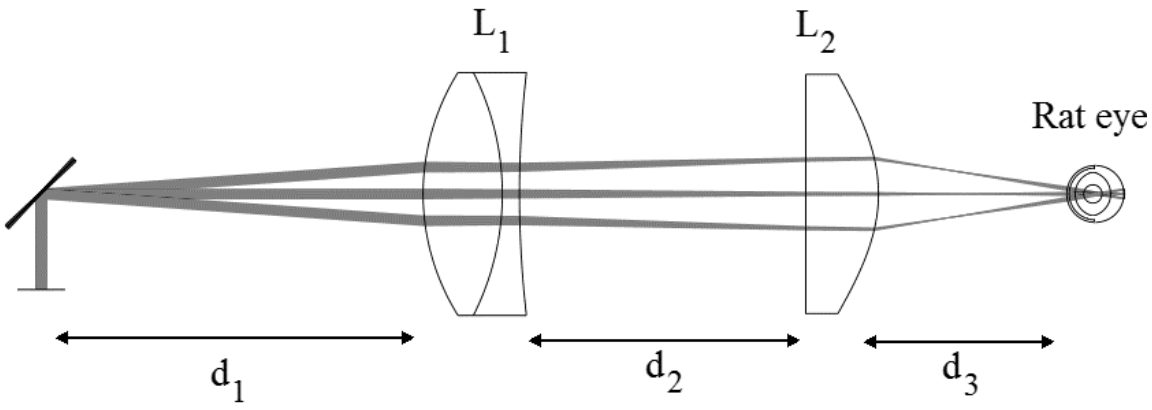

Figure 39. Optical simulation schematic of an achromatic doublet (L_1) and an aspheric lens (L_2) for imaging the rat's eye; d_1= 45 mm, d_2= 68 mm and d_3= 19.7 mm are the distances between the components. Note that the distances and representation of the components are not at scale.

In order to evaluate the focus of rays with a certain incident angle and the field-of-view in the retina, a simulation of a galvanometer system with a maximum scanning angle of ±2° was done. The distance between the pivot point of the galvanometer mirrors and the achromatic doublet is d_1= 45 mm. The distance between the two lenses is d_2= 68 mm, while between the aspheric lens and the rat's eye is d_3= 19.7 mm.

The beam initial aperture diameter was set to 1 mm, and measured approximately 0.4 mm at the entrance of the eye. With these aperture values, the lowest spherical aberration is obtained, and all laser beams for each scanning angle (-2°, 0° and +2°) are focused in the outer limiting membrane of the rat's retina. Therefore, in order to obtain the best imaging conditions, these aperture values as well as the distances presented in Figure 39 should be used. If needed, an iris (for instance, Thorlabs CP20S [56]) with an aperture diameter of 1 mm can be placed in the sample arm – after the collimator and before the galvanometer mirrors – to adjust the diameter of the laser beam.

From the analysis of the spot diagrams depicted in Figure 40, for each scanning angle of the galvanometer mirrors, it is possible to conclude that for a laser beam incident with a certain angle, the spherical aberration of the rat's eye yields a worse focus in the retinal structures than the laser beam incident at zero degrees. The focusing spot for this latter condition presents a radius of approximately 1 µm, which can be considered a very good value when compared with the dimensions of the desired imaging structures (around 10 µm). In fact, this value can be considered as diffraction limited and is a good estimate of the lateral resolution limit for this imaging system. For the case of a maximum galvanometer mirror angle (-2º and +2º), the diagram spot is not circular, exhibiting some

coma aberration due to an off-axis object point. Similarly to the case of a zero degree scanning angle, these can also be considered good values (radius of 2 µm and 3 µm in x and y directions) when compared with the dimensions of the intended imaging objects.

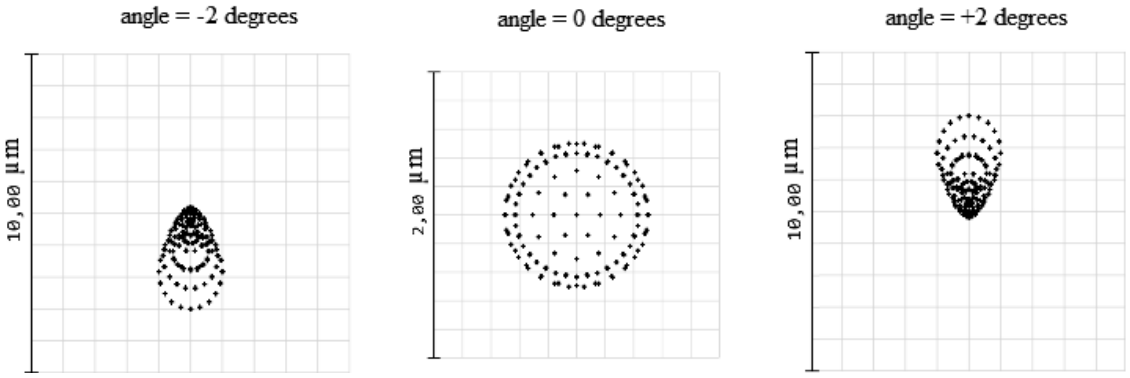

Figure 40. Spot diagram for each scanning angle (-2°, 0°, +2°) of the galvanometer mirrors, obtained in Zemax OpticStudio, for the simulated optical system.

This optical design allows the improvement of the spherical aberration for incident rays with a certain scanning angle due to the presence of the aspheric lens. The Seidel diagram presented in Figure 41 quantifies the spherical aberration for this optical design, detailing the contribution originated from each layer. Layers 16 through 24 represent the structures in the rat's eye (from anterior cornea to outer limiting membrane).

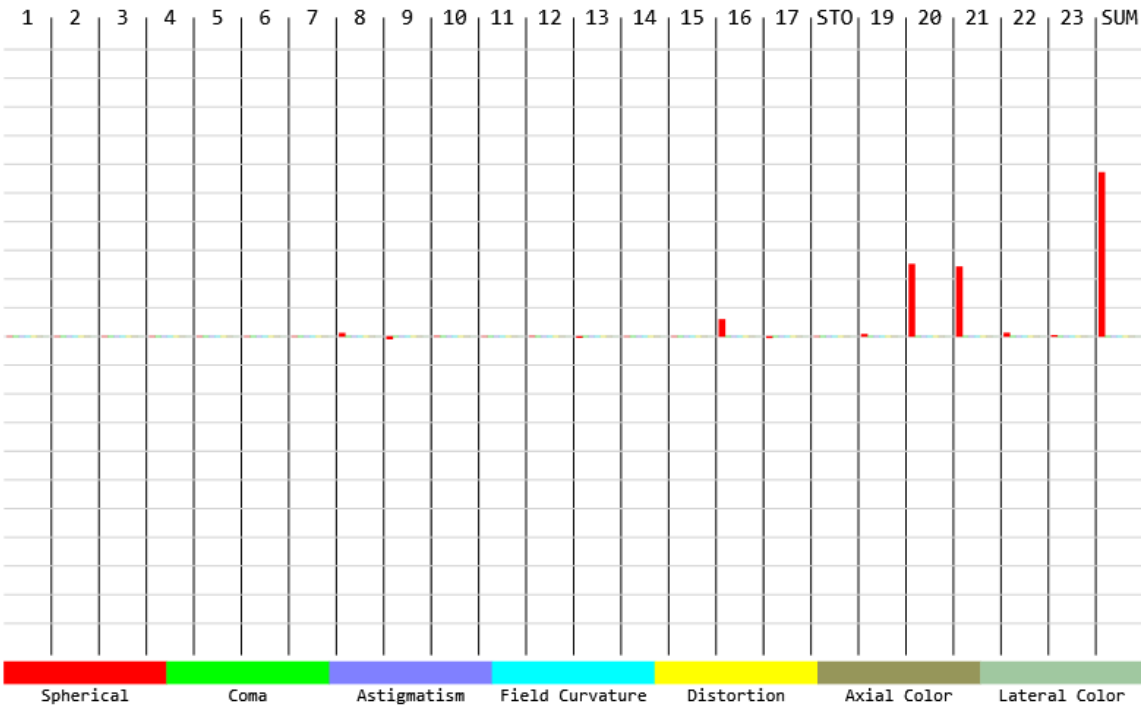

Figure 41. Seidel diagram of the achromatic doublet and aspheric lens simulation, obtained in Zemax OpticStudio for a beam aperture diameter of 0.5 mm at the entrance of the eye, indicating the contributions of each layer of the eye for the spherical aberration (red color). Maximum aberration scale is 0.1 µm and grid lines are spaced 0.01 µm.

In order to evaluate the decrease in spherical aberration while using this imaging setup when compared to direct imaging of the rat's eye without optical components (i.e. using the rat's eye as the sample objective), it is necessary to simulate similar laser incident conditions: an incident laser beam with an aperture diameter of 0.5 mm at the entrance of the eye. This can be done by placing an iris with the desired aperture diameter (aperture STOP, in Zemax) before the eye, to reduce the diameter from the initial value of 1 mm, as presented in Figure 42. The Seidel diagram obtained from this simulation is presented in Figure 43.

Figure 42. Zemax OpticStudio simulation of a laser beam with an initial aperture diameter of 1 mm, resized to 0.5 mm in diameter at the entrance of the rat's eye due to an aperture STOP.

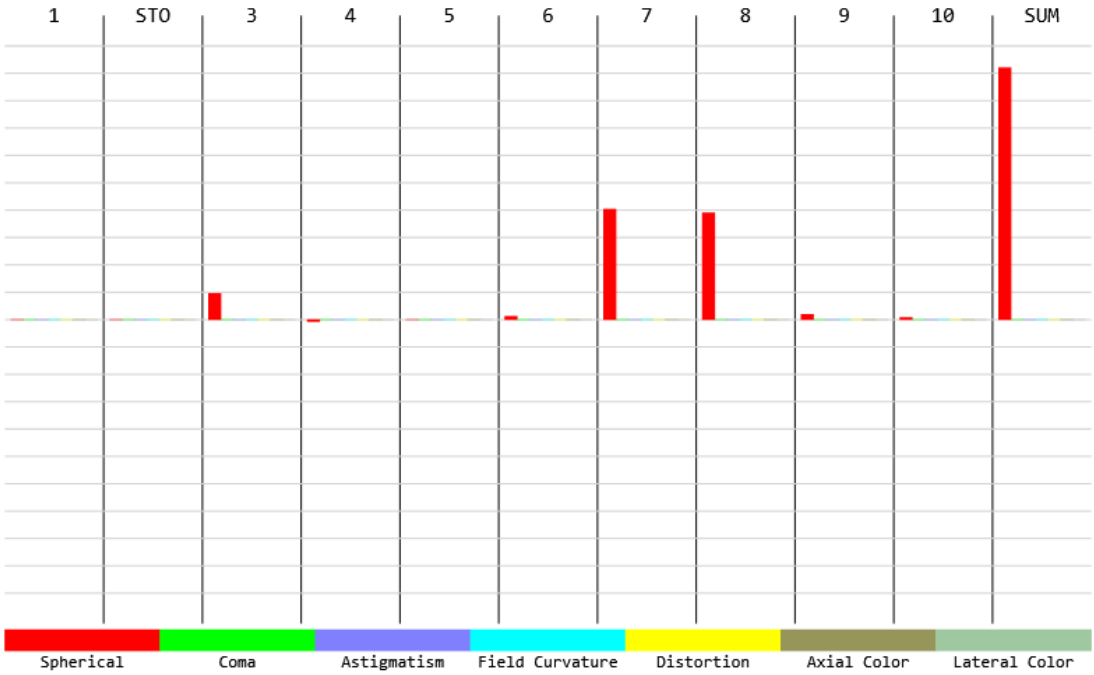

Figure 43. Seidel diagram of the rat's eye for a beam aperture diameter of 0.5 mm at the entrance of the eye, indicating the contributions of each layer of the eye for the spherical aberration (red color). Maximum aberration scale is 5 µm and grid lines are spaced 0.5 µm.

From the Seidel diagram of Figure 43 it is possible to conclude that the spherical aberration (red color) is the main type of aberration present when imaging the rat's eye. For this simulated case, the total spherical aberration due to all the layers in the eye is approximately 4.6 μm. This value is mostly due to both the anterior and posterior cores of the eye's lens (surfaces number 7 and 8 in the diagram), which have a high curvature radius and a small half-diameter.

The decrease in spherical aberration can be concluded from the comparison of this result with the total value obtained from the Seidel diagram of Figure 41, which is 0.06 μm. So, a decrease factor of approximately 77 times in the total spherical aberration is achieved while using the achromatic doublets for imaging the rat's eye. With these imaging conditions, a spherical aberration value of 0.06 μm can be considered a very good value when compared to the smallest spot size of 1 µm diameter, corresponding to 6% of its dimensions.

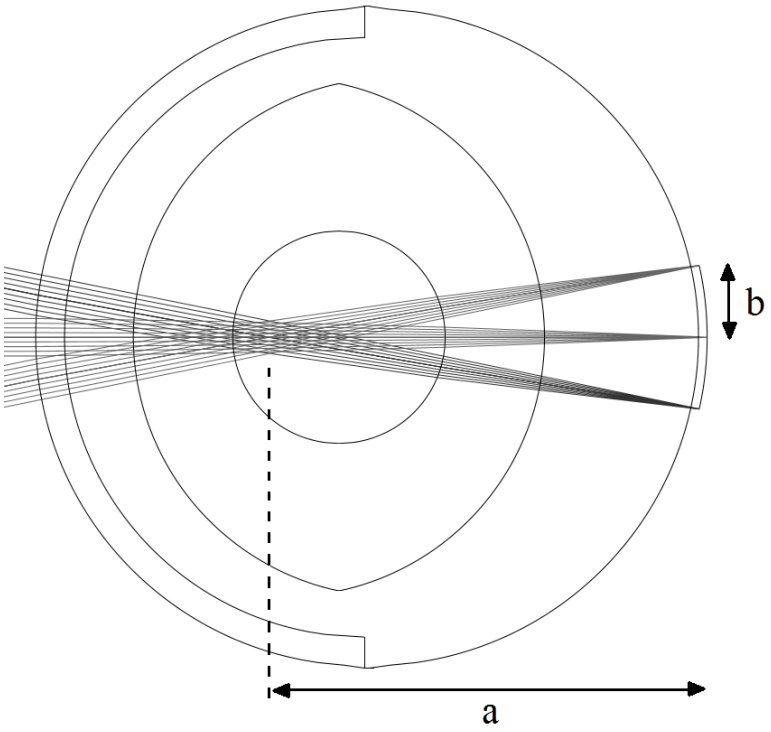

Figure 44. Schematic of the rat's eye, with scanning rays originated from a 2º scan of the galvanometer mirrors, for determining the field-of-view in the retina.

A brief note regarding the resulting field-of-view in the rat's retina while using this optical solution. Through Zemax calculations and schematic representation, it is possible to obtain values for a and b (see Figure 44), where b represents the scanning distance corresponding to the maximum input scanning angle (in our case, two degrees). With

these two values ($a = 4\ mm,\ b = 0.65\ mm$), it is possible to conclude that a 2º galvanometer scan yields a field-of-view value, in degrees, of $2\theta = 2 \times \tan^{-1}\left(\frac{0.65}{4}\right) = 18.5°$. In micrometers, and assuming an isotropic scan in both x and y directions, a squared field-of-view with a 1.30 mm side (double of the obtained b value) can be achieved. Since the intended imaging area in the retina is the optic disc, it is important to compare this FOV value with its dimensions. Based on the description by D. C. Lozano and M. D. Twa in [57], presenting an optic disc diameter of approximately 400 µm, and the 384 µm diameter described by Austin Hughes and Heinz Wässle in [58], it can be concluded that the obtained squared FOV with 1.30 mm of side is enough to cover the region of interest.

Chapter 5

Performance Results

This final chapter presents the experimental results concerning the performance of the Swept Source Optical Coherence Tomography system used throughout this thesis.

The parameters measured and presented here are the system's axial resolution in the air, the sensitivity, the dynamic range, the laser beam diameter, the lateral field-of-view and an estimate (in the air) of the lateral resolution. The experimental methods for obtaining the first three parameters were discussed in the first chapter of this thesis. The procedures for obtaining the remaining parameters (lateral resolution, laser beam diameter and the lateral field-of-view) will be described here.

5.1 Axial resolution

As discussed in chapter 1, it is possible to state the maximum achievable value for the axial resolution, in the air, based on the assumption of a laser beam with a Gaussian shaped power spectrum. The axial resolution can therefore be calculated using Equation 21 from section 1.5.1:

$$\Delta z = \frac{2\ln 2}{\pi}\frac{{\lambda_0}^2}{\Delta\lambda} = \frac{2\ln 2}{\pi} \times \frac{(1060 \times 10^{-9})^2}{110 \times 10^{-9}} = 4.51\ \mu m \tag{41}$$

In a real OCT system, the power spectrum of the source is not Gaussian. An alternative would be to measure the output spectrum of the light source using an optical spectrum analyzer and determine the Full-Width at Half Maximum (FWHM) of the Fourier transformed spectrum [11] or compute it directly from the power spectrum of the source provided by the manufacturer (Figure 23). After digitation of the spectrum and data interpolation, a Lorentzian curve is fitted to the data, as shown in Figure 45. Please note that the side lobes appearing in the Fourier transform of the spectrum are due to the usage of its entire wavelength interval (965 to 1115 nm). Should the 110 nm interval of interest be used, between the 985 and the 1095 nm, the Fourier transform of the spectrum becomes closer to the Lorentzian fit. The maximum achievable resolution value, obtained from the FWHM, is almost exactly the same, though 4.61 μm. Parameters from the fit are presented in Table 6.

Table 6. Lorentzian fit parameters for the Fourier transform of the output source's spectrum, obtained using OriginPro software – w is the Full-Width at Half Maximum, x_c is the peak's position, y_0 is the offset, A is the area under the curve and H is the peak's amplitude.

Parameter	$w\ (\mu m)$	$x_c\ (\mu m)$	$y_0\ (a.u.)$	A	H
Value	4.61	183.4	0.012	7.12	0.98

This fit has an adjusted R-square value of $R^2 = 0.983$. The obtained axial resolution value of $\Delta z = 4.61\ \mu m$ must be considered a more accurate expected value for the OCT system when considering just the optical properties of the light source. However, this value is very close to the one obtained using the Gaussian approximation, which may suggest that deviations from this shape of the power spectrum do not yield considerable changes in the axial resolution since this value is determined at the FWHM of the Fourier transformed spectrum. Please note that this value does not account for the effect of the

spectral response of other OCT components (namely fiber optics and couplers) and of the spectral response of the photodetectors.

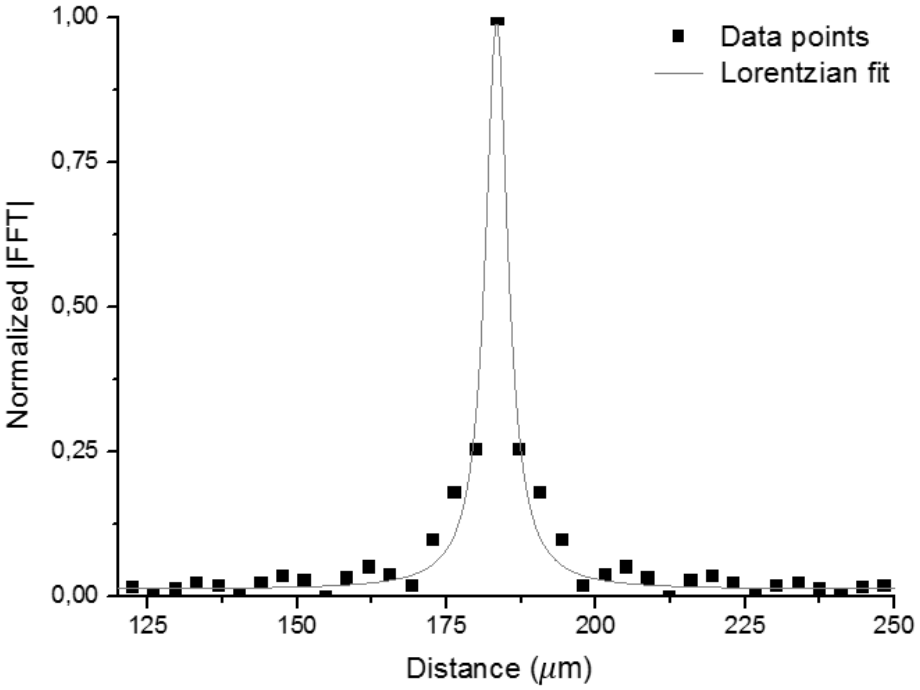

Figure 45. Fourier transform of the output source's spectrum, and respective Lorentzian fit using software OriginPro.

The axial resolution of the entire OCT system, in the air, accounting for all dispersion that may occur in the system components, can be measured using a gold mirror as the sample and determining the FWHM of the acquired PSF, as mentioned in section 1.5.1. It is important to note that, throughout this chapter, the A-scan of a gold mirror (single reflector) will be called "PSF signal", as mentioned in Chapter 1.

Using the data processing software OriginPro, the resulting fit parameters are presented in Table 7. A 5.8 mm thick glass was placed in the reference arm, to minimize dispersion effects.

Table 7. Lorentzian fit parameters, obtained using OriginPro software, for a gold mirror as sample (legend equal to the previous table).

Parameter	$\boldsymbol{w\ (\mu m)}$	$\boldsymbol{x_c\ (\mu m)}$	$\boldsymbol{y_0\ (a.u.)}$	$\boldsymbol{A}$	**H**
Value	8.14	407.57	0.86	1845.32	144.25

This fit has an adjusted R-square value of $R^2 = 0.983$. The axial resolution value of 8.14 μm is, as expected, higher than the theoretical limit, due to the effects of dispersion along

the system's components. However, it is still within the acceptable range for the field of application (up to 10 μm [12]).

5.2 Sensitivity

As explained in Chapter 1, a neutral density filter of known optical density ($OD = 2$) is placed before a gold mirror to measure the sensitivity of the OCT system. Then, a PSF signal is acquired for determining the average value of the noise level, representing the sensitivity in dB (Figure 46).

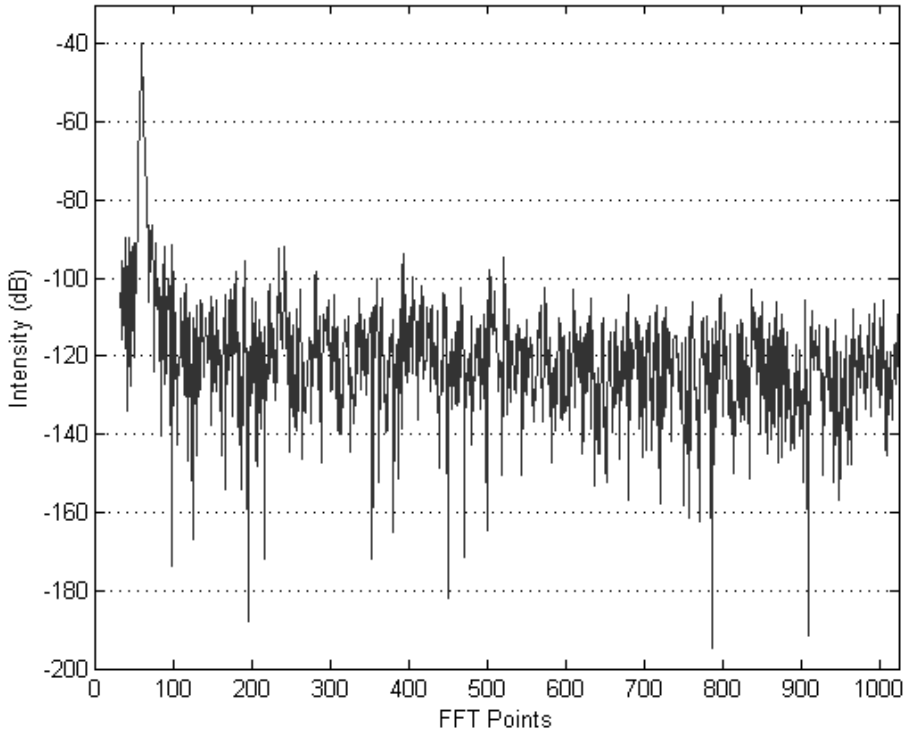

Figure 46. Acquired Point Spread Function of a gold mirror.

The obtained sensitivity value of the OCT system was $S_{dB} = 123.8\, dB$, which corresponds to a minimum reflectivity value of $R_{s,min} = 4.17 \times 10^{-13}$. This sensitivity value represents the maximum attenuation that light reflected from the sample can suffer and still be distinguished from the noise level. Since this value is higher than the minimum standard value of 95 dB [12] accepted for biomedical imaging, it can be considered a good value.

5.3 Dynamic range

The experimental method for determining the dynamic range of an OCT system is similar to the procedure for obtaining the sensitivity. There are, however, two differences: the density filter is not used and only one Point Spread Function is acquired.

The dynamic range was measured for two distinct scenarios – with and without the 100 MHz electronic low-pass filter positioned between the analog output balanced photodetector and the acquisition board.

Figure 48 depicts the acquired data, in logarithmic scale, for the case with the low-pass filter installed. Table 8 contains the maximum PSF value, corresponding to its peak, the standard deviation of the noise level and the resulting dynamic range for both cases studied.

Table 8. Dynamic range (D) measurements, with and without the 100 MHz low-pass filter CLPFL-0100 from Crystek Microwave. PSF_{max} is the peak of the PSF, and σ_{noise} is the standard deviation of the noise floor.

	$\boldsymbol{PSF_{max}}$ $\boldsymbol{(a.u.)}$	$\boldsymbol{\sigma_{noise}}$ $\boldsymbol{(a.u.)}$	$\boldsymbol{D}$ $\boldsymbol{(dB)}$
Without low-pass filter	244.24	0.64	51.69
With low-pass filter	268.31	0.4585	55.35

The use of the low-pass filter improves the results, since it cuts off unwanted high frequencies of the interference signal, allowing for a better signal-to-noise ratio and consequently a higher dynamic range. In both cases, the dynamic range is higher than the minimum required for biomedical imaging, which is 40 to 50 dB [12].

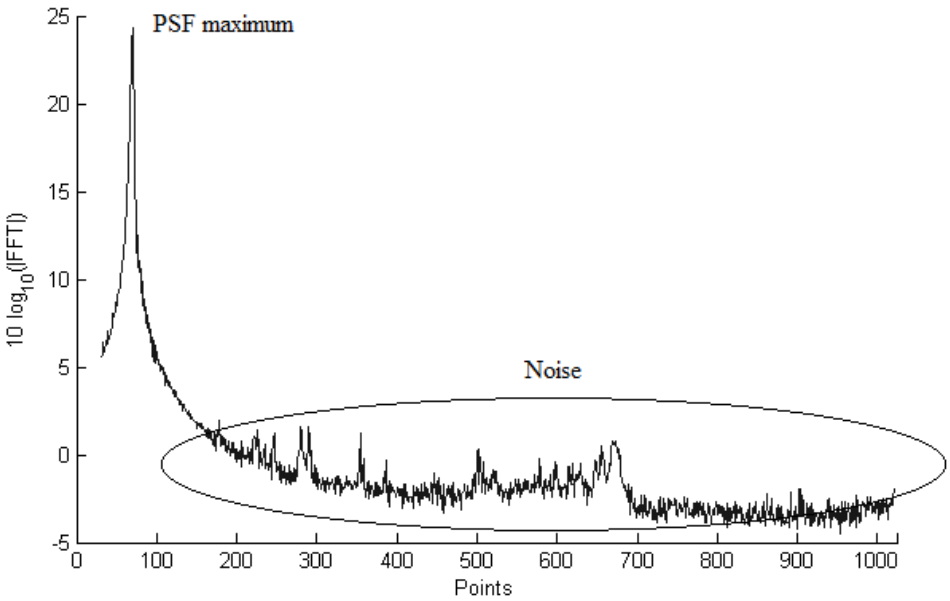

Figure 47. PSF of a gold mirror, for dynamic range determination, using a 100 MHz low-pass filter.

5.4 Sensitivity roll-off

The sensitivity roll-off was determined in a 4 mm depth range. The 100 MHz Butterworth electronic low-pass filter, used during phase measurements in Chapter 3, was present in the OCT setup, since its bandwidth impacts on the imaging depth.

As discussed in chapter 1, consecutive PSF signals were acquired for various depth positions of the sample (gold coated mirror). The light path to the sample can be made to change, using a micrometer drive, with up to 10 µm precision. For this test, a PSF of a gold mirror used as sample was acquired for each 50 μm increment in depth. The obtained PSF's are plotted in Figure 49, where the drop in signal maximum over the distance is notorious.

Fitting a line to the maximum amplitude peaks allows to compute the sensitivity roll-off value (dB/mm). However, it is clear the two distinct regions that would turn a single linear fit a poor approximation (blue fit y in Figure 50). Therefore, two separate linear fits allow for a better description of the data, one for the interval 0-2800 μm (green fit y_1 in Figure 50) and one for the interval 2800-4000 μm (black fit y_2 in Figure 50). Within the depth range of 0 to 2800 μm, the negative slope is 0.92 dB/mm, which represents a very good sensitivity roll-off when compared to the standard values (10 dB/mm [12]). After the 2800 μm, the sensitivity roll-off is of 7.26 dB/mm, still in the normal standard for OCT systems.

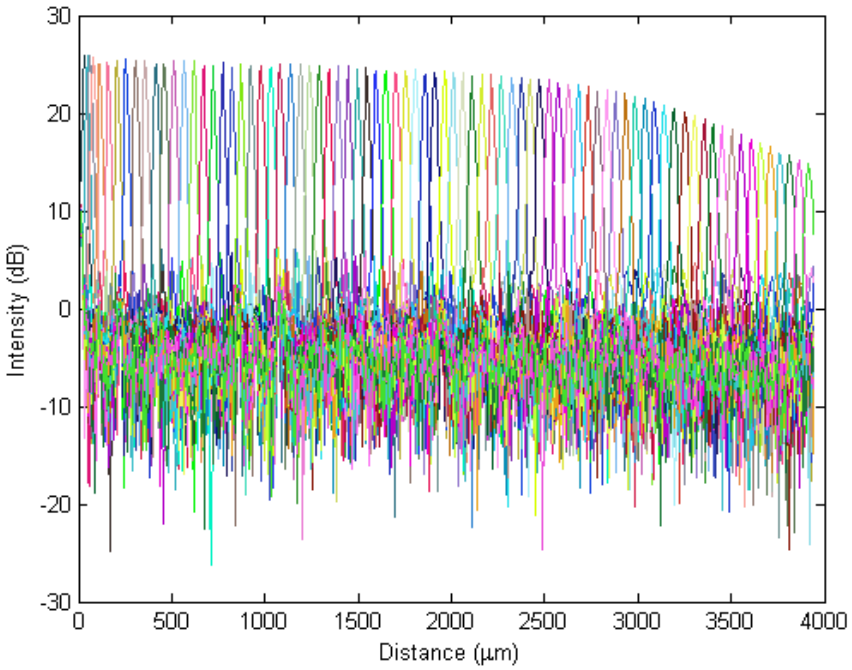

Figure 48. PSF's of a gold mirror, for several depth positions, to determine the sensitivity roll-off of the OCT system.

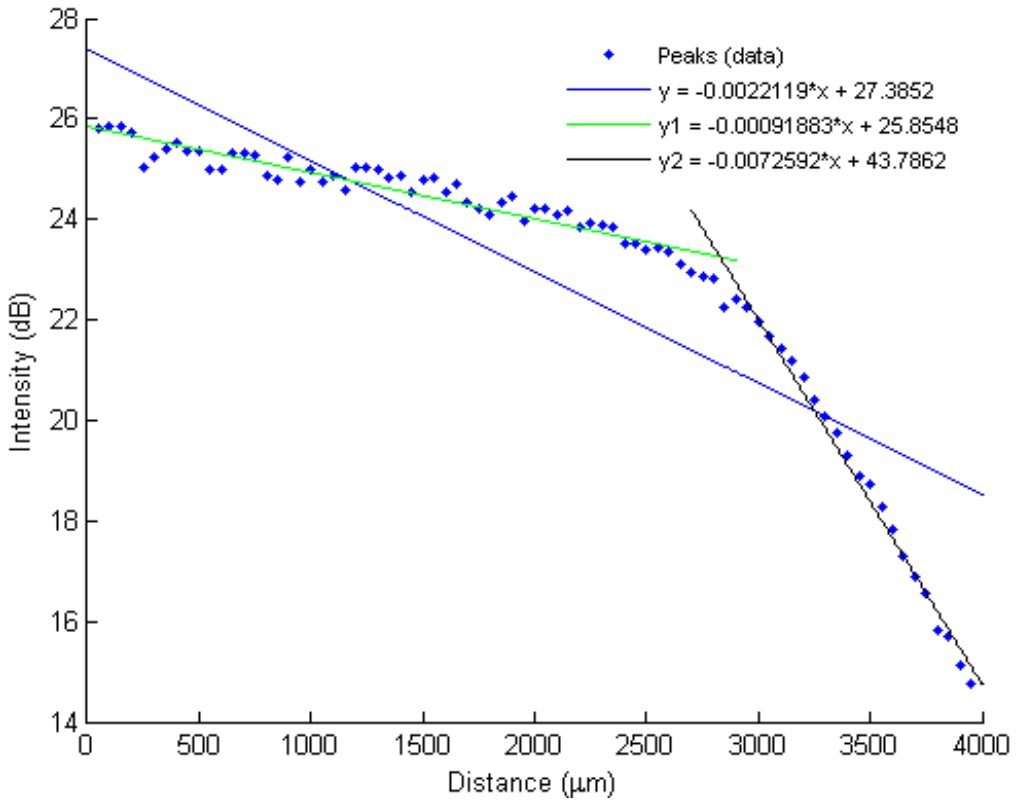

Figure 49. PSF peaks with linear fits (y, y_1, y_2), for determination of the sensitivity roll-off of the OCT system.

5.5 Laser beam profile

Another measured parameters were the shape and dimensions of the system's laser beam. This was done using a beam profiler. It consists of a CCD camera capable of measuring the energy distribution of the laser beam and consequently allow to determine the width in both the x and y directions. In this work, the detection device was a high resolution Spiricon SP620U Beam Profiling Camera from Ophir Photonics.

The beam diameter can be defined in different ways: by the D4σ; the $1/e^2$; and the Full Width at Half Maximum values. In this work, the adopted metric was the D4σ one, which defines the width of a beam in a given direction as being equal to 4 times the standard deviation of the energy distribution in that direction. The software used in this experiment provides measurements in both x and y directions, D4σX and D4σY respectively.

The beam diameter was measured in two distinct points of the sample arm – after the galvanometer mirrors (before the scanning objective lens) and in the focal point of the objective lens. It is only interesting to measure this profile in the sample arm, since it is there that the scan of the sample is made and, therefore, where it is important to assess it.

the laser beam has the right characteristics to irradiate the desired scanning area of the sample. Figures 51 and 52 show the beam profile in both studied cases.

Table 9. SP620U beam profiler specifications [59].

Parameter	Value
Spectral response	190 – 1100 nm
Active area	7.1 mm × 5.4 mm
Pixel spacing	4.4 μm × 4.4 μm
Number of effective pixels	1600 × 1200
Accuracy of beam width	± 2%
Saturation intensity (1)	2.2 μW/cm^2
Lowest measurable signal (1)	2.5 nW/cm^2

(1) Camera set to full resolution at maximum frame rate and exposure times, running CW at 632.8nm wavelength. Camera set to minimum useful gain for saturation test and maximum useful gain for lowest signal test.

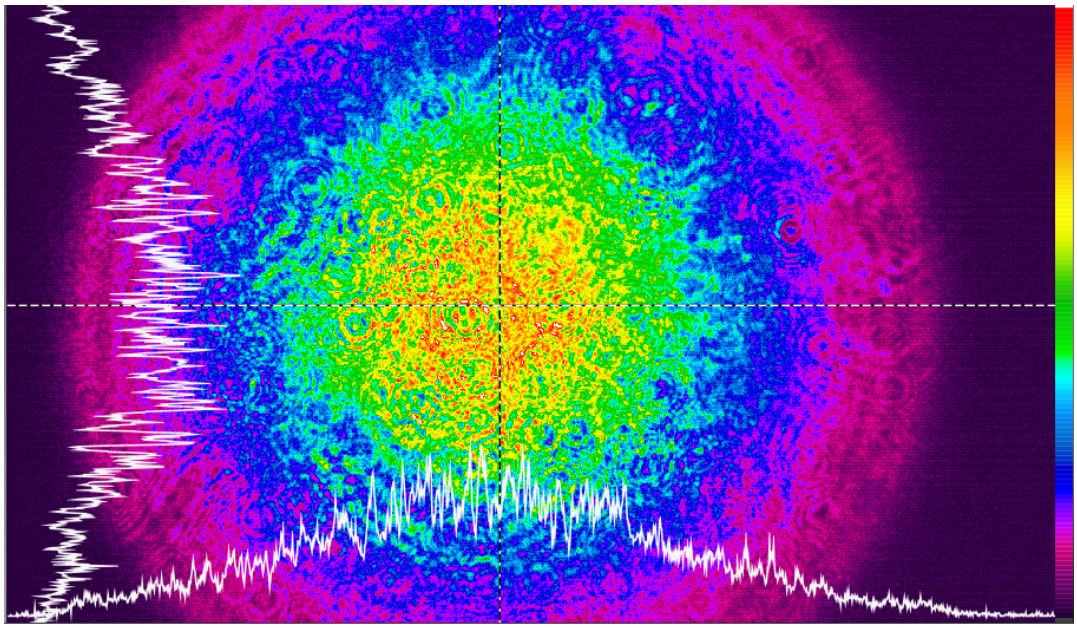

Figure 50. Laser beam profile measured after the galvanometer mirrors.

As expected, the unfocused beam in Figure 51 has a bigger diameter compared to the one measured at the focal point of the objective lens, shown in Figure 52.

Table 10. Results of the beam profile measurements.

	D4σX (mm)	D4σY (mm)
After the galvanometer mirrors	4.858	4.537
Focal point of objective lens	0.679	0.692

In each situation, both x and y diameters measured similar values which indicates that the beam profile can be considered to be spherical, since the measurements were conducted perpendicularly to the beam's propagation direction.

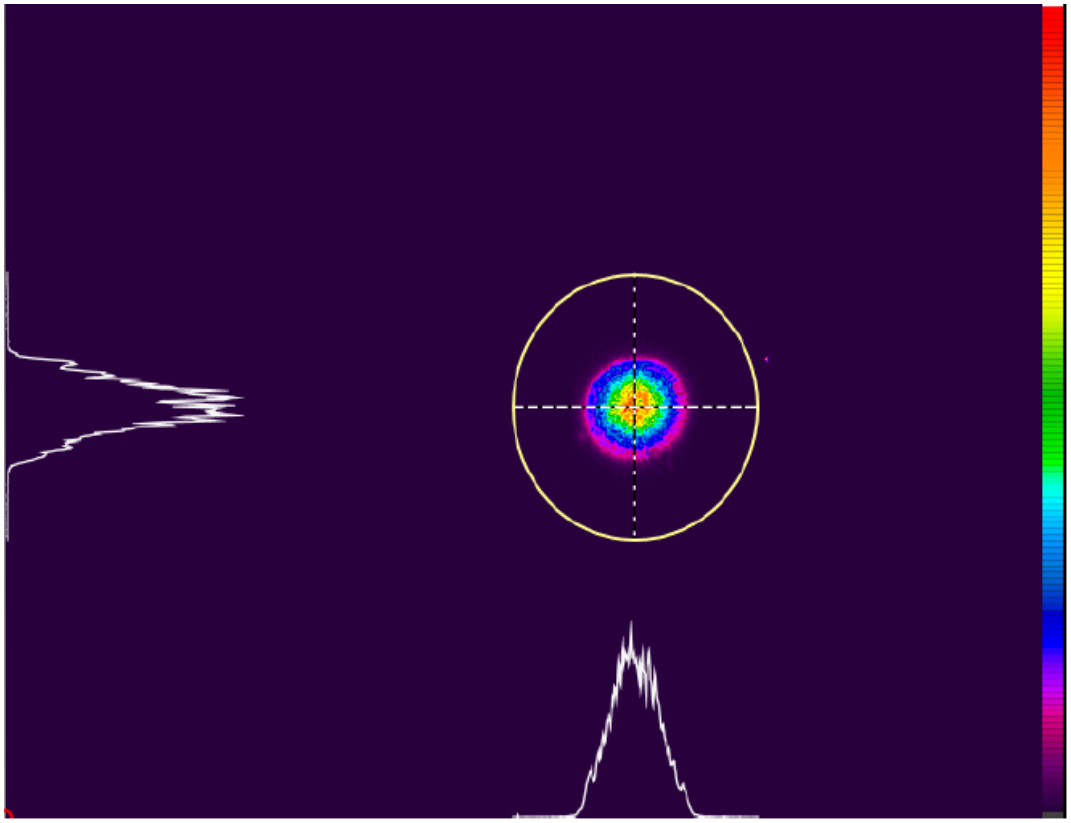

Figure 51. Laser beam profile measured in the focal point of the scanning objective LSM03-BB.

5.6 Field-of-view

Using the same Spiricon SP620U Beam Profiling Camera mentioned in the previous section, a measurement of the lateral field-of-view (in the air) at the focal point of the scanning objective LSM03-BB was performed. This was accomplished by setting up a larger exposure time of the CCD camera, leading to a spreading of the spatial distribution corresponding to the laser scanning movement, as presented in Figure 53, in opposition to the single circular profile observed in the previous section for the case of a single spot focus. Similar to the previous section, the D4σX value of this distribution therefore corresponds to the lateral scanning field-of-view.

As mentioned in chapter 2 when describing of the galvanometer system, the scanning amplitude is controlled by voltage, with a higher voltage (within the range ±10 V peak-to-peak) yielding a wider range of motion of the galvanometer mirrors. So, the

measurement of the dependence of scanning amplitude, at the LSM03-BB focal point, with the peak-to-peak voltage of the ramp wave function provided to the galvanometers was performed.

The registered voltage and respective scanning distance values are presented in the graph of Figure 54, showing a linear behavior. The resulting linear fit has an adjusted R-square value of $R^2 = 0.999$ and is translated by the relation:

$$scanning\ distance\ (mm) = 2.165 \times voltage(V) + 1.664 \quad (42)$$

Note that since the CCD only has 7.1 millimeters horizontally, the maximum applied voltage (2.7 V) is limited by this maximum measurable scanning distance. However, through the previous equation it is possible to extrapolate data for higher values of applied voltage.

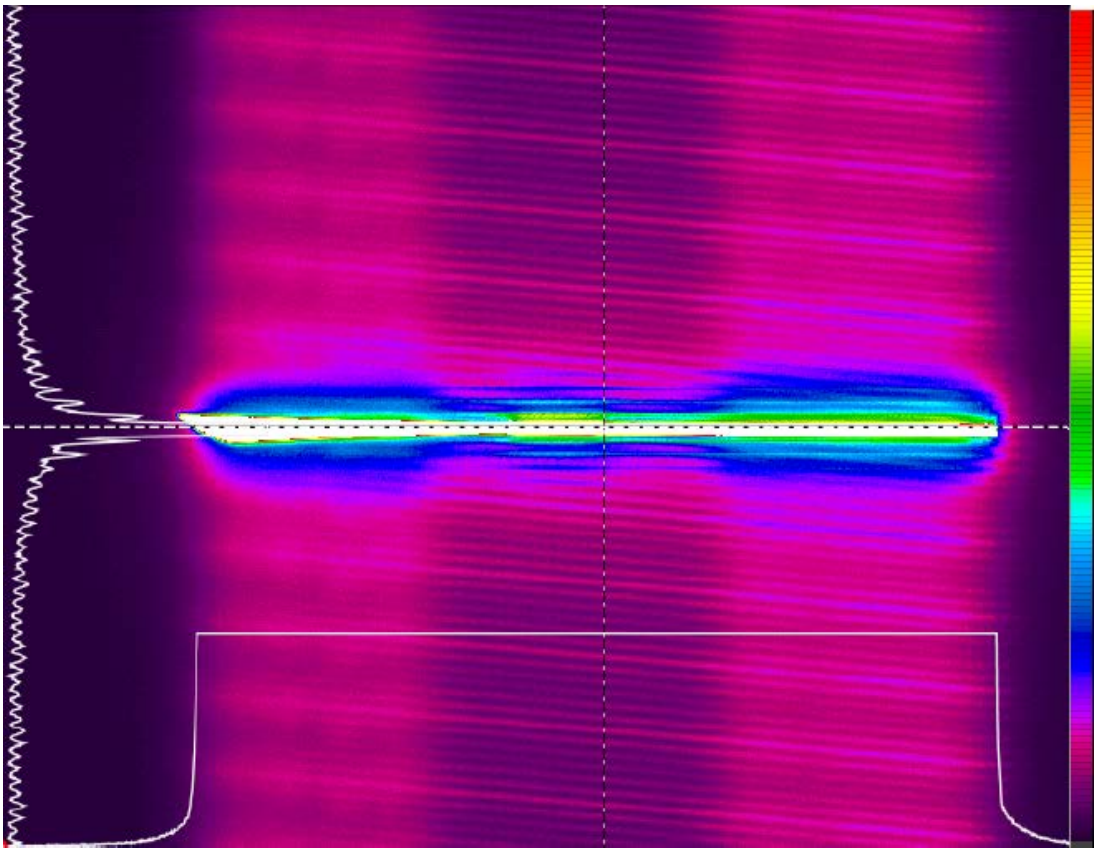

Figure 52. Scanning profile measured in the focal point of the scanning objective LSM03-BB.

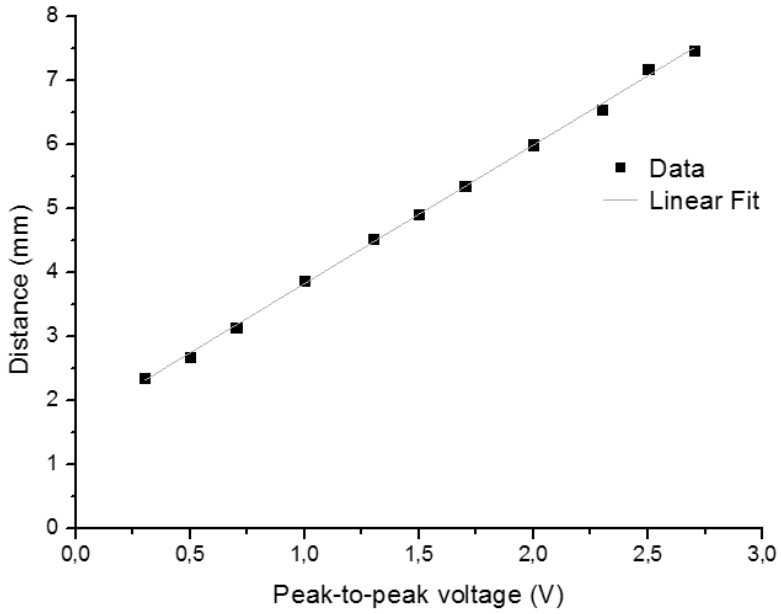

Figure 53. Scanning distance data as a function of peak-to-peak voltage applied to the galvanometer mirrors, with respective linear fit performed using OriginPro software.

The previous relation (Equation 42) is valid for the current optical setup of the sample arm, which includes an objective lens LSM03-BB from Thorlabs for scanning the sample.

5.7 Estimation of lateral resolution

It is possible to estimate the lateral resolution (in air) of an OCT system by imaging a variable line grating target. Since this target is a thick cover glass with several line mirrors of different widths and spacing, in M categories of N line pairs per millimeter (lp/mm), if the system is able to distinguish those consecutive mirrors in a M category, then its lateral resolution is, at least, equal to $\frac{1\,mm}{N\,lines}$. The target used in the measurements was the R1L3S6P Variable Line Grating Target (Figure 55), from Thorlabs, with line densities ranging from 1.25 to 250 line pairs per millimeter (Table 11).

Table 11. Resolution of line grating for the R1L3S6P target. From [60].

Resolution of Line Grating (lp/mm)								
1.25	2.08	2.86	3.85	5	10	16.67	50	200
1.67	2.5	3.33	4.17	6.67	12.5	26	100	250

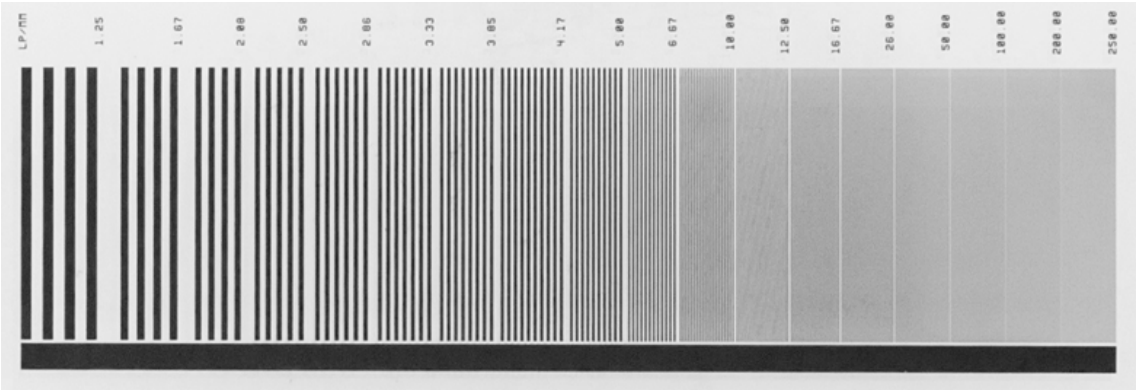

Figure 54. R1L3S6P Variable Line Grating Target, from Thorlabs. From [60].

Figure 56 presents the acquired B-scan while imaging both 100 lp/mm and 200 lp/mm densities, with a scanning amplitude high enough to image both areas. It is possible to conclude that the lines in the range of 100 lp/mm (right side of image) can still be distinguished in the image while the ones in the 200 lp/mm range (left side of image) cannot. Therefore, it is possible to conclude that the lateral resolution of the OCT system with the current optics is:

$$\Delta x = \frac{1\ mm}{100\ lp} = 10\ \mu m \tag{43}$$

Since this measurement was obtained using the LSM03-BB scanning objective in the sample arm, it is possible to determine a theoretical value for the lateral resolution based on the objective's numerical aperture, NA, as previously detailed in chapter 1. From the specifications of the scanning objective [36], using the value 0.22 mm of depth of view for 1050 nm, it is possible to determine the objective's NA (Equation 24 from chapter 1):

$$b = 2\frac{n\,\lambda}{NA_{obj}^2} \Leftrightarrow NA_{obj} = \sqrt{\frac{2 \times 1 \times 1050 \times 10^{-9}}{0.22 \times 10^{-3}}} = 0.0977 \tag{44}$$

which corresponds to a theoretical value of lateral resolution for a wavelength of 1040 nm of (Equation 23 from chapter 1):

$$\Delta x = 1.22\frac{\lambda_0}{2NA_{obj}} = 1.22\frac{1040 \times 10^{-9}}{2 \times 0.0977} = 6.5\ \mu m \tag{45}$$

Although the line grating used in this experiment only allowed to conclude that lateral resolution value is at least 10 μm, this can be considered a good value when comparing to the theoretical one and considering that most ophthalmological OCT systems present a lateral resolution ranging between 10 and 15 μm [61].

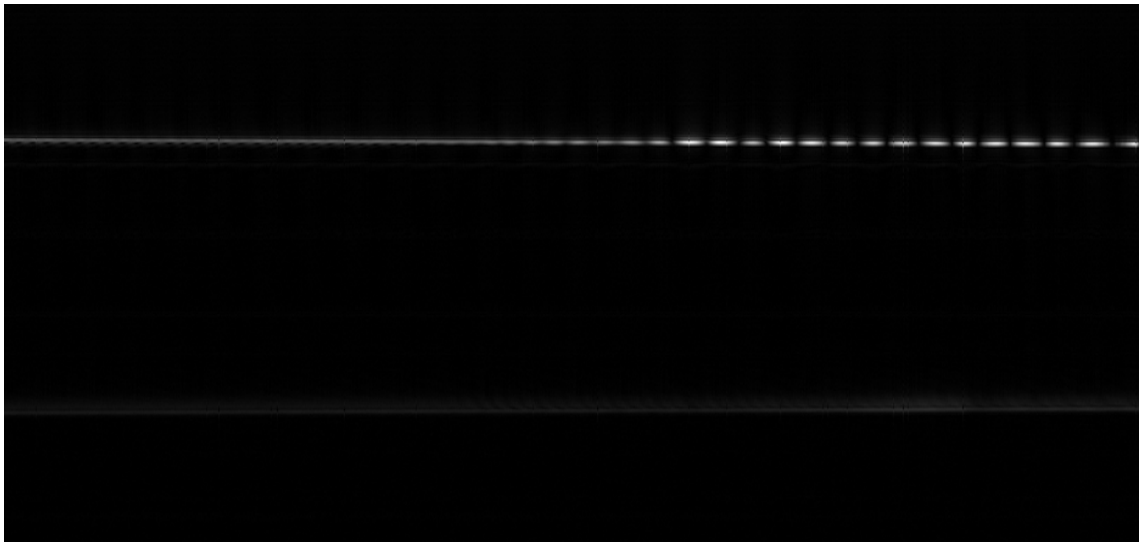

Figure 55. B-scan of the variable line grating target. The upper right side corresponds to the 100 lp/mm region of the target, while the upper left side corresponds to the 200 lp/mm. The bottom line corresponds to the back-side of the thick cover glass (not relevant to this analysis).

The intensity profile along the upper white line of the B-scan in Figure 55 (obtained using the *ImageJ* software), corresponding to the different mirror surfaces of the variable line grating target, supports the conclusion regarding the lateral resolution value. It is clear that in the right part of the graph (matching the 100 lp/mm region of the target) the variations in pixel intensity are well defined, as opposed to the left part (200 lp/mm).

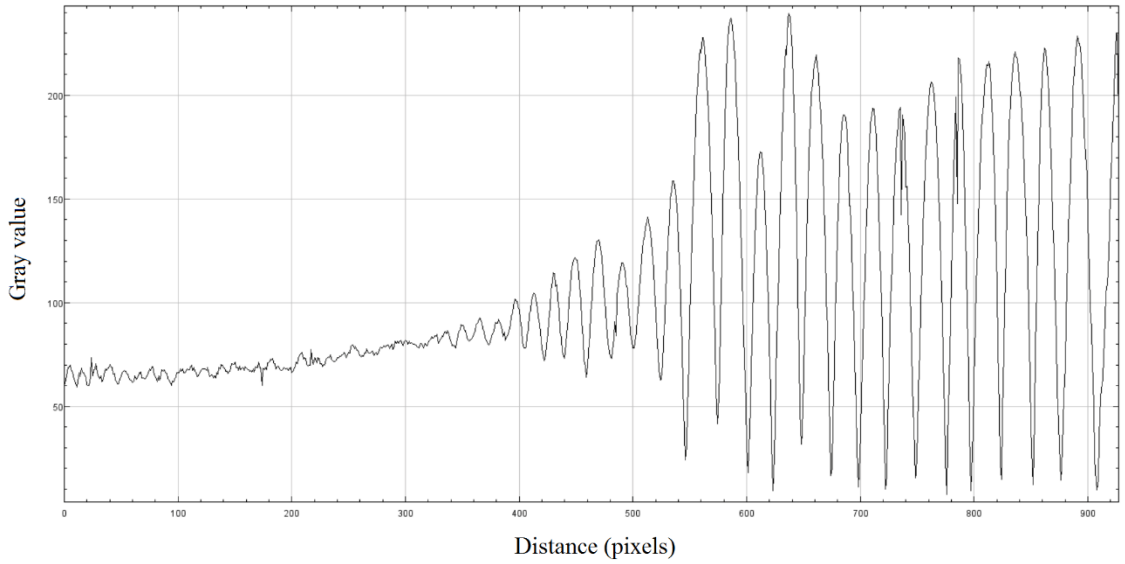

Figure 56. Analysis, using ImageJ software, of the white line in Figure 55 corresponding to the variable line grating target used for estimation of the system's lateral resolution.

Conclusions and future work

In this work, the SS-OCT under development was analyzed in detail and its performance characterized with respect to its components and setup. Furthermore, the optics of the system towards imaging the eye of rats and mice was simulated based on current system characteristics. Finally, the study on the stabilization of the phase of the interference signal was analyzed and a correction algorithm implemented.

The phase stabilization algorithm presented in section 3.3 allowed for a phase stability of 11.9 mrad. This value is close to the desired 9 mrad, even though there are significant differences on the laser sources. The level of stabilization achieved allows to conclude on the possibility to carry reliable phase measurements using the current setup.

In its present implementation, the phase stabilization is tailored for post-processing. Although the computing times involved are considerable, considering the trends and speed of acquisition of state-of-the-art OCT systems, it serves its current purposes. There is still room for improvement and the algorithm may be embedded in the acquisition module in the future, should it prove of general interest and should it become fast enough.

The validation of the optical design was carried through simulations using the Zemax OpticStudio suite. From the simulations it is possible to conclude on the adequacy of the optical setup containing an achromatic doublet and aspheric lens.

Additional optical simulations were performed including the scanning system (galvanometer mirrors) to establish the expected field-of-view in the rat's eye fundus. The results point to the possibility to cover a square area with side length of 1.30 mm on the ocular fundus. This area, which corresponds to an angular field of view of 18.5º, allows to image the entire optic disc of the rat (diameter around 400 µm), a landmark in the rat's ocular fundus, and is within the desired range.

The evaluation of the system lateral resolution (estimated to be at least 10 µm) allows to conclude on the average performance of the system. Although this value stands in the desired range for the intended applications, current trends are to increase it to the highest possible extent. Adaptive optics is a potential solution to consider in subsequent versions, even though it will greatly increase the complexity of the system.

Regarding the performance parameters, all experimentally obtained results are within the standards for retinal imaging. The possibility for further improvements are manifold and include, among others, the use of a dispersion-compensating prism pair in the reference arm, for fine, continuous, adjustment of dispersion correction. These solutions will come at the cost of increased complexity and thus making the alignment of the optics a much more difficult process.

Looking back, this project was an amazing opportunity for my academic formation. During this course I got a grasp on the optical coherence tomography technique, an increasing important imaging modality in the biomedical field. Along the process I had the need and opportunity to get acquaintance on Zemax OpticStudio, a reference tool in optical design. This allowed me to put in practice the knowledge of optics acquired during my academic courses. Finally, I had the chance to develop my programming skills, a fundamental tool for the current engineering professional.

References

[1] J. A. Izatt, M. A. Choma and A. Dhalla (2015), "Theory of Optical Coherence Tomography", in *Optical Coherence Tomography - Technology and Applications* (2nd Edition), Springer.

[2] M. Duguay and T. Mattick (1971), "Ultrahigh speed photography of picosecond light pulses and echoes", Appl. Opt., vol. 10, no. 9, pp. 2162–2170.

[3] J. G. Fujimoto, S. De Silvestri, E. P. Ippen, C. A. Puliafito, R. Margolis, and A. Oseroff (1986), "Femtosecond optical ranging in biological systems", Opt. Letters, vol. 11, no. 3, p. 150.

[4] F. Fercher, K. Mengedoht, and W. Werner (1988), "Eye-length measurement by interferometry with partially coherent light", Opt. Letters, vol. 13, no. 3, pp. 186–188.

[5] X. Clivaz, F. Marquis-Weible, R. P. Salathé, R. P. Novàk, and H. H. Gilgen (1992), "High-resolution reflectometry in biological tissues", Opt. Letters, vol. 17, no. 1, pp. 4–6.

[6] D. Huang *et al.* (1991) "Optical Coherence Tomography", Science (New York, N.Y.) 254.5035, pp. 1178–1181.

[7] P. Tomlins and R. Wang (2005), "Theory, developments and applications of optical coherence tomography", J. Phys. D. Appl. Phys., vol. 38, no. 15, pp. 2519–2535.

[8] M. Brezinski (2006), "Optical Coherence Tomography - Principles and Applications" (1st Edition), Academic Press - Elsevier.

[9] I. J. Bigio, S. Fantini (2016), "Quantitative Biomedical Optics - Theory, Methods and Applications" (1st Edition), Cambridge University Press.

[10] W. Drexler, J. G. Fugimoto (2015), "Introduction to Optical Coherence Tomography", in *Optical Coherence Tomography - Technology and Applications* (2nd Edition), Springer.

[11] J. Kolb, T. Klein, M. Eibl, T. Pfeiffer, W. Wieser, R. Huber (2016), "Megahertz FDML laser with up to 143nm sweep range for ultrahigh resolution OCT at 1050nm", Proc. SPIE, vol. 9697.

[12] W. Wieser, B. R. Biedermann, T. Klein, C. M. Eigenwillig, and R. Huber (2010), "Multi-megahertz OCT: High quality 3D imaging at 20 million A-scans and 4.5 GVoxels per second", Opt. Express, vol. 18, no. 14, pp. 14685–14704.

[13] M. D. Bayleyegn, H. Makhlouf, C. Crotti, K. Plamann, and A. Dubois (2012), "Ultrahigh resolution spectral-domain optical coherence tomography at 1.3µm using a broadband super luminescent diode light source", Opt. Commun., vol. 285, no. 24, pp. 5564–5569.

[14] S.-W. Lee, H.-W. Song, M.-Y. Jung, and S.-H. Kim (2011), "Wide tuning range wavelength-swept laser with a single SOA at 1020 nm for ultrahigh resolution Fourier-domain optical coherence tomography", Opt. Express, vol. 19, no. 22, pp. 21227-21237.

[15] M. R. Hee (2002), "Optical Coherence Tomography: Theory" in *Handbook of Optical Coherence Tomography* (1st Edition), CRC Press.

[16] M. A. Rollins, J. A. Izatt (1999), "Optimal interferometer designs for optical coherence tomography", Opt. Letters, vol. 24, no. 21, pp. 1484-1486.

[17] J. E. Nevins, G. Wollstein and J. Schuman (2015), "OCT Imaging in Glaucoma", in *Optical Coherence Tomography - Technology and Applications* (2nd Edition), Springer.

[18] P. A. Keane, P. J. Patel, S. Liakopoulos, F. M. Heussen, S. R. Sadda and A. Tufail (2012), "Evaluation of age-related macular degeneration with optical coherence tomography", Survey of Ophthalmology, vol. 57, no. 5, pp. 389–414.

[19] E. M. Frohman, J. G. Fujimoto, T. C. Frohman, P. A. Calabresi, G. Cutter and L. J. Balcer (2008), "Optical Coherence Tomography: A Window Into the Mechanisms of Multiple Sclerosis", Nat Clin Pract Neurol., vol. 4, no. 12, pp. 664-675.

[20] W. Drexler and J. G. Fujimoto (2015), "Retinal Optical Coherence Tomography Imaging", in *Optical Coherence Tomography - Technology and Applications* (2nd Edition), Springer.

[21] M. Terashima, H. Kaneda, T. Suzuki (2012), "The Role of Optical Coherence Tomography in Coronary Intervention", The Korean Journal of Internal Medicine, vol. 27, no. 1, pp. 1-12.

[22] T. Yonetsu, M. Villiger, B. Bouma and I.-K. Jang (2015), "Cardiovascular Optical Coherence Tomography", in *Optical Coherence Tomography - Technology and Applications* (2nd Edition), Springer.

[23] F. Alfonso, M. Paulo, N. Gonzalo, J. Dutary, P. Jimenez-Quevedo *et al.* (2012), "Diagnosis of spontaneous coronary artery dissection by optical coherence tomography", J. Am. Coll. Cardiol., vol. 59, no. 12, pp. 1073–1079.

[24] J. Hou, H. Lv, H. Jia, S. Zhang, L. Xing *et al.* (2012), "OCT assessment of allograft vasculopathy in heart transplant recipients", JACC Cardiovasc. Imaging, vol. 5, no. 6, pp. 662–663.

[25] B. Baumann, B. Potsaid, M. F. Kraus *et al.* (2011), "Total retinal blood flow measurement with ultrahigh speed swept source/Fourier domain OCT", Biomedical Opt. Express, vol. 2, no. 6, pp. 1539-1552.

[26] M. Wojtkowski (2010), "High-speed optical coherence tomography: basics and applications", Applied Optics, vol. 49, no. 16, pp. D30-D61.

[27] R. Leitgeb, C. K. Hitzenberger, and A. F. Fercher (2003), "Performance of fourier domain vs. time domain optical coherence tomography", Optics Express, vol. 11, no. 8, pp. 889-894.

[28] B. Potsaid, V. Jayaraman, J. Jiang, A. Cable, P. Heim, I. Grulkowski, and J. G. Fujimoto (2012), "1065nm and 1310nm MEMS tunable VCSEL light source technology for OCT imaging", SPIE Newsroom, pp. 8–10.

[29] L.S. Lim, G. Cheung and S.Y. Lee (2014), "Comparison of spectral domain and swept-source optical coherence tomography in pathological myopia", Eye, vol. 28, no. 4, pp. 488-491.

[30] Axsun OCT Swept Source Engine Operator's Manual (2010), Rev. 09, Axsun Technologies Inc., Massachusetts, USA.

[31] Spectra Database hosted at the University of Arizona (2016), Spectra at UA [Online] Available at: http://www.spectra.arizona.edu, (Accessed 06 July 2016).

[32] Balanced Amplified Photodetectors - PDB47xC Operation Manual (2014), Thorlabs.

[33] W.-C. Kuo, C.-M. Lai, Y.-S. Huang, C.-Y. Chang, and Y.-M. Kuo (2013), "Balanced detection for spectral domain optical coherence tomography," Opt. Express, vol. 21, no. 16, pp. 19280-19291.

[34] X5-400M User's Manual (2011), Rev. 1.01, Innovative Integration, California, USA.

[35] GSV002 Scanning Galvo Systems - User Guide. Thorlabs.

[36] Scan Lenses for Laser Scanning Microscopy (2016), Thorlabs [Online] Available at: https://www.thorlabs.de/newgrouppage9.cfm?objectgroup_id=2910&pn=LSM02-BB, (Accessed 18 April 2016).

[37] Boy Braaf, Koenraad A. Vermeer, Victor Arni D.P. Sicam, Elsbeth van Zeeburg, Jan C. van Meurs, and Johannes F. de Boer (2011), "Phase-stabilized optical frequency domain imaging at 1-μm for the measurement of blood flow in the human choroid", Opt. Express, vol. 19, no. 21, pp. 20886-20903.

[38] Gangjun Liu and Zhongping Chen (2008), "Phase-resolved Doppler Optical Coherence Tomography", in *Selected Topics in Optical Coherence (2nd Edition)*, Intech.

[39] B. White, M. Pierce, N. Nassif, B. Cense, B. Park, G. Tearney, B. Bouma, T. Chen, and J. de Boer (2003), "In vivo dynamic human retinal blood flow imaging using ultra-high-speed spectral domain optical coherence tomography", Opt. Express, vol. 11, no. 25, pp. 3490–3497.

[40] Yonghua Zhao, Zhongping Chen, Christopher Saxer, Qimin Shen, Shaohua Xiang, Johannes F. de Boer, and J. Stuart Nelson (2000), "Doppler standard deviation imaging for clinical monitoring of in vivo human skin blood flow", Opt. Letters, vol. 25, no.18, pp. 1358-1360.

[41] WooJhon Choi, Benjamin Potsaid, Vijaysekhar Jayaraman, Bernhard Baumann, Ireneusz Grulkowski, Jonathan J. Liu, Chen D. Lu, Alex E. Cable, David Huang, Jay S. Duker, and James G. Fujimoto (2013), "Phase-sensitive swept-source optical coherence tomography imaging of the human retina with a vertical cavity surface-emitting laser light source", Opt. Letters, vol. 38, no.3, pp. 338-340.

[42] Young-Joo Hong, Shuichi Makita, Franck Jaillon, Myeong Jin Ju, Eun Jung Min, Byeong Ha Lee, Masahide Itoh, Masahiro Miura, and Yoshiaki Yasuno (2012), "High-

penetration swept source Doppler optical coherence angiography by fully numerical phase stabilization", Opt. Express, vol. 20, no.3, pp. 2740-2760.

[43] Gangjun Liu, Ou Tan, Simon S. Gao, Alex D. Pechauer, ByungKun Lee, Chen D. Lu, James G. Fujimoto, and David Huang (2015), "Postprocessing algorithms to minimize fixed-pattern artifact and reduce trigger jitter in swept source optical coherence tomography", Opt. Express, vol. 23, no.8, pp. 9824-9834.

[44] M. Bonesi, M. P. Minneman, J. Ensher, B. Zabihian, H. Sattmann, P. Boschert, E. Hoover, R. A. Leitgeb, M. Crawford, and W. Drexler (2014), "Akinetic all-semiconductor programmable swept-source at 1550 nm and 1310 nm with centimeters coherence length", Opt. Express, vol. 22, no.3, pp. 2632-2655.

[45] Y. Sasaki, M. Fujimoto, S. Yagi, S. Yamagishi, S. Toyoda, J. Kobayashi (2014), "Ultrahigh-phase-stable swept source based on KTN electro-optic deflector towards Doppler OCT and polarization-sensitive OCT", Proc. SPIE, vol. 8934.

[46] R. K. Manapuram (2012), "Development of phase stabilized swept source optical coherence tomography for biomedical imaging and sensing", *Ph. D. dissertation*, University of Houston, Texas (USA).

[47] Y.-J. Hong, S. Makita, F. Jaillon, M. J. Ju, E. J. Min, B. H. Lee, M. Itoh, M. Miura, and Y. Yasuno (2012), "High-penetration swept source Doppler optical coherence angiography by fully numerical phase stabilization," Opt. Express, vol. 20, no. 3, pp. 2740-2760.

[48] A. Hughes (1979), "A schematic eye for the rat," Vision Res., vol. 19, no. 5, pp. 569–588.

[49] D. Link, C. Strohmaier, B. U. Seifert, T. Riemer, H. A. Reitsamer, J. Haueisen and W. Vilser (2011), "Novel non-contact retina camera for the rat and its application to dynamic retinal vessel analysis," Biomed. Opt. Express, vol. 2, no. 11, pp. 3094-3108.

[50] P. Artal, P. H. de Tejada, C. M. Tedó and D. G. Green (1998), "Retinal image quality in the rodent eye", Vis. Neurosci., vol 15, no. 4, pp. 597-605.

[51] S. Hariri (2013), "Ultrahigh Resolution Optical Coherence Tomography for Non-invasive Imaging of Outer Retina Degeneration in Rat Retina", Doctoral thesis, University of Waterloo, Ontario (Canada).

[52] K. Grieve, M. Paques, A. Dubois, J. Sahel, C. Boccara, J.-F. Gargasson (2004), "Ocular Tissue Imaging Using Ultrahigh-Resolution, Full-Field Optical Coherence Tomography", Invest. Ophthalmol. Vis. Sci., vol. 45, no. 11, pp. 4126-4131.

[53] W. Drexler, M. Liu, A. Kumar, T. Kamali, A. Unterhuber, R. Leitgeb (2014), "Optical coherence tomography today: speed, contrast, and multimodality", J. Biomed. Opt., vol. 19, no. 7, p. 071412.

[54] Unmounted Achromatic Doublets, AR Coated (2016), Thorlabs [Online] Available at: https://www.thorlabs.de/newgrouppage9.cfm?objectgroup_id=899&pn=AC254-060-C, (Accessed 1 August 2016).

[55] Mounted High-Precision Aspheres (2016), Thorlabs [Online] Available at: https://www.thorlabs.com/newgrouppage9.cfm?objectgroup_id=8402&pn=AL2520M, (Accessed 1 August 2016).

[56] Cage System Iris Diaphragms (2016), Thorlabs [Online] Available at: https://www.thorlabs.de/newgrouppage9.cfm?objectgroup_id=8376&pn=CP20S, (Accessed 1 August 2016).

[57] D. C. Lozano and M. D. Twa (2013), "Development of a Rat Schematic Eye From In Vivo Biometry and the Correction of Lateral Magnification in SD-OCT Imaging", Invest. Ophthalmol. Vis. Sci., vol. 54, no. 9, pp. 6446–6455.

[58] A. Hughes, H. Wässle (1979), "An estimate of image quality in the rat eye", Invest. Ophthalmol. Vis. Sci, vol. 18, no. 8, pp. 878-881.

[59] SPU620U Beam Profiling Camera Datasheet (2016), Ophir Photonics [Online] Available at: http://www.ophiropt.com/laser--measurement/beam-profilers/products/Beam-Profiling/Camera-Profiling-with-BeamGage/SP620U, (Accessed 03 May 2016).

[60] R1L3S6P Variable Line Grating Target (2016), Thorlabs [Online] Available at: https://www.thorlabs.com/newgrouppage9.cfm?objectgroup_id=4338&pn=R1L3S6P, (Accessed 12 May 2016).

[61] H.-W. Wang, J. A. Izatt and M. D. Kulkarni (2002), "Optical Coherence Microscopy" in Handbook of Optical Coherence Tomography (1st Edition), CRC Press.